Compound III-V semiconductor avalanche photodiodes for X-ray spectroscopy

Rajiv Bernard Gomes

A thesis submitted for the degree of Doctor of Philosophy

Department of Electronic and Electrical Engineering

The University of Sheffield

June 2012

Contents

Acknowledgements

Abstract

A theoretical investigation into the avalanche statistics limited energy resolution of avalanche photodiodes (APDs) was carried out using a random path length (RPL) model. The probability density function (PDF) of the avalanche gain which directly affects the energy resolution was computed taking into account the effects of the incident photon energy, the pair creation energy of the interacting material, the electron and hole ionisation coefficients and the mean avalanche gain. The results show that the use of conventional excess noise factors obtained from light measurements to calculate the spread in energy resolution due to avalanche statistics is incorrect as the gain PDF generated by X-ray absorption is considerably different from that obtained from light detection. The effect of dead space on the PDF was also investigated. Significant dead space leads to a more deterministic multiplication process leading to a narrow gain PDF and hence an improvement in the spectral resolution. Simulations were performed to study the experimental pulse height spectra obtained from a $GaAs/Al_{0.8}Ga_{0.2}As$ separate absorption and multiplication (SAM) APD. The simulated spectra are found to be in good agreement with experimental results when the noise from APD and read out electronics along with the statistics of photon energy loss were accounted for. The spectral performance of the SAM APD at room temperature is also presented.

In addition to the SAM APD, narrow bandgap InAs has also been investigated. InAs has the potential to achieve spectral resolution beyond that of elemental Si and Ge, closer to that obtained by superconductors. Its larger atomic number and crystal density also ensure that its linear stopping power is higher than elemental semiconductors. In addition, InAs APDs exhibit the highly desirable single carrier ionisation characteristic that leads to low avalanche excess noise. Electrical and X-ray characterisation of InAs n^+ip^+ APDs was carried out at liquid nitrogen temperature. The 5.9 keV X-ray energy peak from a ^{55}Fe radioisotope source was detected at zero bias with a full width

half maximum (FWHM) of 2.8 keV. At increasing gain the 5.9 keV peak shifts away from the electronic noise floor improving the signal to noise performance of the detector. This is also complemented by a rapid improvement in the energy resolution with an FWHM of 950 eV obtained at a gain of 5.3. Modelling of the X-ray pulse height spectra was carried out using the RPL technique. The intrinsic resolution limited by avalanche statistic was found to be independent of avalanche gain.

List of publications

Journal Publications

1. **R. B. Gomes**, C. H. Tan, P. J. Ker, J. P. R. David, and J. S. Ng, "InAs avalanche photodiodes for X-ray detection," *Journal of Instrumentation,* vol. 6, p. P12005, 2011.

2. **R. B. Gomes**, C. H. Tan, J. E. Lees, J. P. R. David, and J. S. Ng, "Effects of Dead Space on Avalanche Gain Distribution of X-Ray Avalanche Photodiodes," *Electron Devices, IEEE Transactions on,* vol 59, pp 1063 - 1067, 2012.

3. **R. B. Gomes**, C. H. Tan, J. P. R. David, and J. S. Ng, "Soft X-ray spectroscopy using GaAs/Al$_{0.8}$Ga$_{0.2}$As separate absorption and multiplication (SAM) avalanche photodiodes, " *in prep*

4. C. H. Tan, **R. B. Gomes,** J. P. R. David, A. M. Barnett, D. J. Bassford, J. E. Lees, and N. Jo Shien, "Avalanche Gain and Energy Resolution of Semiconductor X-ray Detectors," *Electron Devices, IEEE Transactions on,* vol. 58, pp. 1696-1701, 2011.

5. J. E. Lees, A. M. Barnett, D. J. Bassford, J. S. Ng, C. H. Tan, N. Babazadeh, **R. B. Gomes**, P. Vines, J. P. R. David, R. D. McKeag, and D. Boe, "Development of high temperature AlGaAs soft X-ray photon counting detectors," *Journal of Instrumentation,* vol. 6, p. C12007, 2011.

6. A. M. Barnett, J. E. Lees, D. J. Bassford, J. S. Ng, C. H. Tan, N. Babazadeh, and **R. B. Gomes**, "The spectral resolution of high temperature GaAs photon counting soft X-ray photodiodes," *Nuclear Instruments and Methods in Physics Research Section A: Accelerators, Spectrometers, Detectors and Associated Equipment,* vol. 654, pp. 336-339.

7. A. M. Barnett, J. E. Lees, D. J. Bassford, J. S. Ng, C. H. Tan, and **R. B. Gomes**, "Temperature dependence of the avalanche multiplication process and the impact ionisation coefficients in Al0.8Ga0.2As," *Nuclear Instruments and Methods in Physics Research Section A: Accelerators, Spectrometers, Detectors and Associated Equipment,* vol. 629, pp. 154-156.

8. A. M. Barnett, J. E. Lees, D. J. Bassford, J. S. Ng, C. H. Tan, and **R. B. Gomes**, "Modelling results of avalanche multiplication in AlGaAs soft X-ray APDs," *Nuclear Instruments and Methods in Physics Research Section*

A: Accelerators, Spectrometers, Detectors and Associated Equipment, vol. 626â, pp. 25-30, 2011/1/21/.

Conference Publications

1. **R. B. Gomes**, C. H. Tan, J. E. Lees, J. P. R. David, and J. S. Ng, "Avalanche gain distribution of X-ray avalanche photodiodes," in *Nuclear Science Symposium and Medical Imaging Conference (NSS/MIC), 2011 IEEE*, 2011, pp. 2238-2241.

2. **R. B. Gomes**, P. J. Ker, C. H. Tan, J. P. R. David, and J. S. Ng, "InAs avalanche photodiodes for X-ray detection," in *Nuclear Science Symposium and Medical Imaging Conference (NSS/MIC), 2011 IEEE*, 2011, pp. 2071-2073.

3. **R. B. Gomes**, C. H. Tan, J. P. R. David, Y. L. Goh and J. S. Ng, "Characterisation and a new method for modelling of avalanche multiplication of X-ray avalanche photodiodes ", in *38th International Symposium on Compound Semiconductors*, Berlin 2011.

4. **R. B. Gomes**, C. H. Tan, J. P. R. David, Y. L. Goh and J. S. Ng, "Characterisations of GaAs/AlGaAs separate absorption and multiplication (SAM) avalanche photodiodes for soft X-ray detection", in *Semiconductor and Integrated OptoElectronics Conference*, Cardiff 2011.

5. J. S. Ng, P. Vines, **R. B. Gomes**, N. Babazadeh, J. E. Lees, J. P. R. David, and C. H. Tan, "GaAs p-i-n diodes for room temperature soft X-ray photon counting," in *Nuclear Science Symposium and Medical Imaging Conference (NSS/MIC), 2011 IEEE*, 2011, pp. 4809-4811.

6. P. J. Ker, A. R. J. Marshall, **R. B. Gomes**, J. P. R. David, J. S. Ng and C. H. Tan, " InAs Electron-avalanche photodiodes: from leaky diodes to extremely low noise avalanche photodiodes," in *IEEE Photonics 2011 Conference*, Virginia 2011.

7. J. E. Lees, A. M. Barnett, D. J. Bassford, J. S. Ng, C. H. Tan, J. P. R. David, N. Babazadeh, **R. B. Gomes**, P. Vines, R. D. McKeag, and D. Boe, "Development of AlGaAs avalanche diodes for soft X-ray photon counting," in *Nuclear Science Symposium and Medical Imaging Conference (NSS/MIC), 2011 IEEE*, 2011, pp. 4528-4531.

Glossary of terms

a	Electron ionisation coefficient
	$a*$ Enabled Electron ionisation coefficient
A	Atomic weight
A_0	Amplifier gain
ADC	Analog to digital converter
APD	Avalanche photodiode
β	Hole ionisation coefficient
	$\beta*$ Enabled hole ionisation coefficient
C	Capacitance
	C_D Detector capacitance
	C_f Feedback capacitance
	C_T Total capacitance
CCD	Charge coupled device
d	Dead space
	d_e Electron hard threshold dead space
	d_h Hole hard threshold dead space
e_n	Preamplifier voltage noise spectral density
ε	electron - hole pair creation energy
ξ	Electric field
E	Energy
	E_{bind} Binding energy
	E_c Escape energy
	E_g Direct energy bandgap
	E_R Energy resolution defined as the % ratio of FWHM to the photon energy.
	E_{the} Electron impact ionisation threshold energy
	E_{thh} Hole impact ionisation threshold energy
EHP	Electron - hole pair
ENC	Equivalent noise charge

F	Excess noise factor	
	F_e	Pure electron injection excess noise factor
	F_h	Pure hole injection excess noise factor
f	Fano factor	
FWHM	Full width at half maximum of energy peak	
	$FWHM_g$	Full width at half maximum of avalanche gain distribution
g	Avalanche gain per photon	
g_m	Transconductance	
η_{int}	Detection efficiency	
h	Plank's constant	
I	Current	
	I_{diff}	Diffusion current
	I_{db}	Bulk leakage current
	I_{ds}	Surface leakage current
	I_g	Gate leakage current
J_D	Dark current density	
k_b	Boltzmann's constant	
k	Ionisation coefficient ratio	
λ	Mean free path length	
	λ_e	Mean free path length of electron
	λ_h	Mean free path length of hole
LIA	Lock-in amplifier	
M	Mean avalanche multiplication factor	
MCA	Multichannel analyser	
N	Number of EHPs	
φ	Linear absorption coefficient	
ϕ	Linear attenuation coefficient	
PDF	Probability density function	
PMT	Photomultiplier tube	
PWN	Parallel white noise	
Q	Charge	
ϱ	Density	

R		Resistance
	R_g	Gate resistance
	R_P	effective parallel resistance
	R_s	series resistance
	R_b	bias resistance
RPL		Random path length
σ		Standard deviation
S		Noise spectral density
SAM		Separate absorption and multiplication
SMU		Source measure unit
SWN		Series white noise
T		Temperature
τ		Shaping time
μ		Mobility
	μ_e	Electron mobility
	μ_h	Hole mobility
ν		Photon frequency
V		Voltage
Ψ		Avalanche noise spectral density
	Ψ_e	Pure electron avalanche noise spectral density
	Ψ_h	Pure hole avalanche noise spectral density
w		Avalanche region width
Z		Atomic number

Chapter 1 Introduction

1.1 Overview and motivation

wavelength

	Long wave Radio	10^3
10^6	Short wave Radio	
		10^0
10^9	Microwaves	
	Millimetre waves	10^{-3}
Hz 10^{12}		m
	Infrared light	
	Visible light	10^{-6}
10^{15}	Ultravoilet light	
		10^{-9}
10^{18}	X-rays	
		10^{-12}
	Gamma rays	
10^{21}		

Frequency
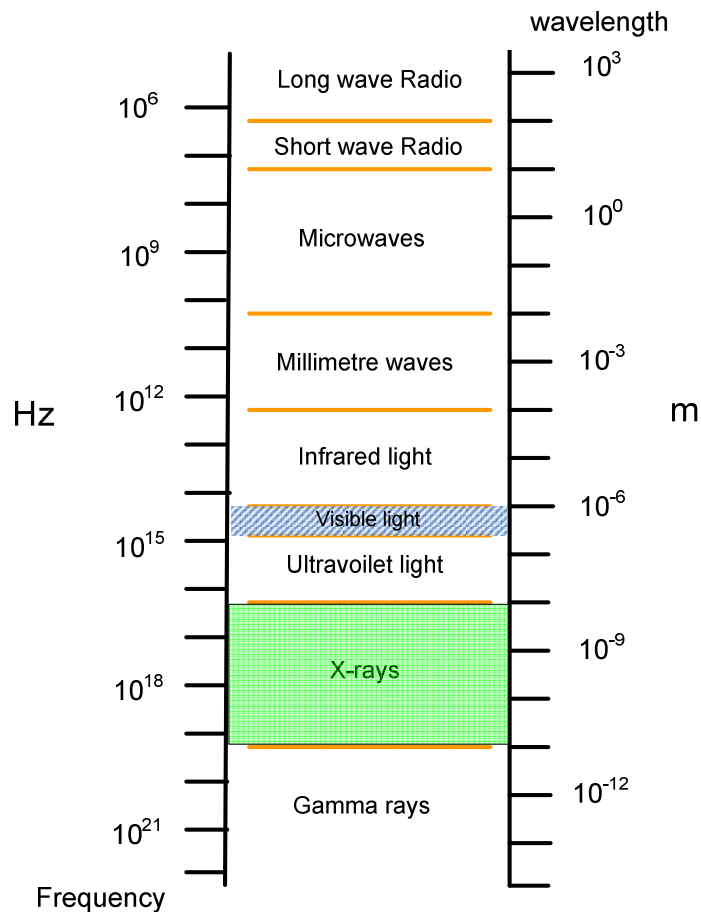
Figure 1.1 Schematic of the electromagnetic spectrum

In late 1985 Wilhelm Röntgen noticed that a barium platinocyanide screen was fluorescing as he generated cathode rays a few feet away using a cathode ray tube. The rays referred to as X-rays (X standing for an unknown quantity usually used in mathematics) were invisible to human eye and possessed high energy that enabled them to pass through matter. X-rays occupy the short wavelength portion of the electromagnetic spectrum from 10^{-8} to 10^{-11} m.

Immediately following his discovery X-rays were extensively used in medical imaging by using a photographic plate as a detector. In 1912 M. von Laue and P. Knipping used X-rays to obtain the diffraction pattern of crystals. Another important landmark was reported in 1953 when J. Watson and F. Crick used X-rays to solve the structure of the DNA. The X-ray tube has been conventionally used to generate X-rays by bombarding high energy electrons on a metal target. Mono energetic X-rays are also emitted from the decay of radioactive isotopes. X-rays are still omnipresent in medicine due to use in dental imaging and mammography. Apart from the medical applications X-rays are also important in astronomy, nuclear physics and crystallography.

The use of semiconductor detectors like p^+in^+ diodes, charge coupled devices (CCDs) and phototransistors has been popular in various industrial, biomedical and telecommunication applications. Semiconductors have the flexibility to be modified to fit a particular application that requires a specific spectral response, speed and geometry. Despite these advantages these devices need to operate in conjunction with low noise external amplifiers to amplify the detected signal. Photomultiplier tubes (PMTs) that are capable of operating at high gains have also been popular. PMTs are used in spectrometry, medical imaging systems, photometry and photon counting applications. However PMTs have many disadvantages; they are highly sensitive to stray magnetic fields (could affect their operation in positron emission tomography systems), high operating voltage (for high negative bias of the photocathode to accelerate the electrons away from it) and very low quantum efficiency as not every photon incident on the photocathode generates an electron. For the last 40 years the development of APDs as more flexible alternatives to PMTs has been undertaken. APDs operate at fields close to avalanche breakdown where carrier multiplication occurs hence producing internal gain. The development of high speed, low noise APDs with high quantum efficiency have been spurred by the recent advances in the telecommunication industry. This has led to the investigation of semiconductors like Si, Ge, GaAs. InP and InGaAs. APDs are available commercially for operation at a range of wavelength from visible to infrared light up to the wavelengths from telecommunications.

The development of semiconductor X-ray APDs has been largely limited to Si. The use of APDs for detection of ionising radiation was first shown by Locker and Huth [1]. One of the first uses of X-ray using APDs was carried out by Webb and McIntyre [2]. Most of the work was focused on analysing the avalanche noise performance of these APDs and their use as a replacement to the PMT [3, 4]. A Si APD coupled with a scintillator for detection of higher energy X-rays was carried out by Petrillio [5]. An investigation on the application of a Bismuth Germanate scintillator coupled to a Si APD for PET applications was also carried out[6, 7]. These initial results showed that APDs could be used for achieving good resolution without the requirement for expensive low noise electronics. The resolution was largely limited by the gain non uniformity across the devices.

Apart from coupling with scintillators Si APDs were also being used for direct detection of X-rays. Squillante et $al.$ showed the use of a Si APD for detection up to 26 keV with an energy resolution given by the ratio of the FWHM to the photon energy $E_R = 10\%$ obtained from a 5.9 keV X-ray peak [8]. APDs with very low noise threshold which enabled the detection of light elements were shown in [9], a peak at 1.49 keV was detected well above the noise floor originating from the backscatter of Aluminium. Energy thresholds as low as 50 eV have been demonstrated using a Si APD with a bevelled edge design [10]. Bevelled edge devices manufactured by Advanced Photonics Inc. were extensively studied by Moszynski et $al.$ [11-15]. Highlights of the results obtained include an energy resolution of $E_R = 4.8$ % using a scintillator crystal coupled to an APD for 662 keV gamma-rays. Since the devices also had a thick absorption region direct detection of X-ray was also possible and best resolution $E_R = 9.3$ % at 5.9 keV X-rays was obtained. Reach through APDs for direct detection [16] and reverse type APDs which have the avalanche region close to the surface of the detector and are hence most suitable for coupling with scintillators [17, 18] developed by Hamamatsu photonics have also been studied. The scintillator-APD performance was comparable to that obtained by the bevelled edge APDs. For direct X-ray detection an $E_R = 6.4$ % was achieved at 5.9 keV at -20 °C, which is the best resolution performance obtained using an

APD [19], still higher than the 130 eV that has been achieved with Si CCDs which were cooled to -90 °C [20].

In the early 1990's Kishimoto *et al.* pioneered the use of APDs for fast detection using synchrotron radiation with sub nanosecond timing resolution [21, 22]. This was then extended to devices with larger area and thicknesses for more practical application in nuclear scattering experiments by Baron *et al.* [23, 24]. A general overview of APDs for high count rate applications with good timing resolution can be found in [25, 26].

Although good energy and timing resolution have been obtained using Si APDs the detection of higher energy X-rays is limited by the maximum thickness of the detector. Compound semiconductor materials like GaAs, CdTe, CdZnTe, PbI_2 and HgI_2 have been investigated as alternatives to Si. These semiconductors offer higher detection efficiency due to their larger atomic numbers and crystal densities. They also offer the capability of room temperature operation with good resolution due to their larger band gap. An in depth review of progress in these materials is given by Sellin [27] and McGregor [28]. Owens *et al,* have also reviewed and highlighted the potential of a large number of compound semiconductors for radiation detection [29]. Narrow band compound semiconductors have also been investigated as they have the potential to achieve much better spectral resolution than Si with a higher quantum efficiency and peak to Compton ratio. There has been very little reported work on the use of compound semiconductors as X-ray APDs. Lauter *et al.* reported a GaAs/AlGaAs SAM APD with an energy resolution defined by the FWHM of the energy peak of 1.95 keV at 13.96 keV [30, 31]. GaAs was used as an absorber layer and an AlGaAs layer was used as the multiplication layer. An improvement in energy resolution to 0.9 keV was obtained at a gain of 4.1. GaP APDs operating in the Geiger mode have been demonstrated to detect X-rays, although their performance as energy resolving APDs were not studied [32]. $Al_{0.8}Ga_{0.2}As$ p^+in^+ diodes for soft X-ray spectroscopy has been the only other reported work on compound semiconductor X-ray APDs [33, 34]. The

APD was also operated above room temperature and showed an energy resolution (1.0–1.25 keV) over a temperature range of -30 to +90 °C.

APDs offer improvement in energy resolution and system signal to noise ratio due to internal gain when the system noise is dominated by amplifiers. Since avalanche multiplication is a stochastic process, randomness in the process will lead to an additional contribution to the intrinsic energy resolution of the APD. Despite many reports of X-ray APDs with good performance there has been a lack of gain optimisation studies in these APDs. The main motivation of this work is to understand the avalanche gain distribution effects on the energy resolution of X-ray APDs for a wide range of semiconductor materials. This will enable design of APDs optimised for low intrinsic noise with good energy resolving capabilities. Another section of this work focuses on the development of narrow band gap semiconductor APDs for X-ray detection. These APDs offer the potential for much lower spectral resolution and higher quantum efficiency than elemental semiconductors like Si and Ge.

1.2 Organisation of thesis

This thesis, presents a Monte Carlo method which has been developed to study the avalanche gain limited energy resolution in semiconductor X-ray APDs. The thesis reports the electrical and X-ray characterisation of an InAs n^+ip^+ diode for soft X-ray detection. The performance of the diode as an X-ray APD is also presented. The spectral performance of a $GaAs/Al_{0.8}Ga_{0.2}As$ SAM APD for room temperature photon counting applications is presented. The aforementioned Monte Carlo model was used to analyse the pulse height spectra obtained from the SAM APD. An overview of the thesis is provided below with a brief summary of the individual chapters.

Chapter 2 provides an outline of the interaction process of X-rays in semiconductors. A description of a read out system for pulse height analysis is also presented. A detailed breakdown of the various noise sources which lead to

fluctuations in the energy resolution both intrinsic to the APD and that arising from external electronics is described. An overview of the impact ionisation theory and avalanche multiplication along with the excess noise is presented.

Chapter 3 describes the experimental techniques used to characterise the X-ray APDs presented in the thesis. Electrical characterisation systems used to measure the current-voltage and capacitance voltage characteristics of the APD are described. Phase sensitive detections technique to measure the avalanche gain is detailed. A simple X-ray spectrometer that was set-up to obtain pulse height spectra from the APDs is also described.

Chapter 4 presents a Monte Carlo model to determine the PDF of the avalanche gain distribution in APD. The dependence of the energy resolution on the incident photon energy, its mean free path length through the absorbing material, the pair creation energy, impact ionisation coefficients and dead space of the APD along with the mean operating gain is rigorously analysed.

Chapter 5 describes the first report on the InAs n^+ip^+ diode both as a soft X-ray detector and its operation as an X-ray APD. The energy resolution and noise performance of the APD is experimentally and theoretically investigated.

Chapter 6 reports the experimental results on a GaAs/$Al_{0.8}Ga_{0.2}$As SAM APD for X-ray spectroscopy. The spectral performance of the detector was determined at room temperature. Simulations were performed to reproduce the experimentally obtained spectra at different gain values using the model described in chapter 4. An analysis of the electronic noise of the spectrometer was also performed.

Chapter 7 summaries all the work presented in the thesis along with suggestions for future work in compound III-V X-ray APDs.

1.3 References

[1]   R. J. Locker and G. C. Huth, "A NEW IONISING RADIATION DETECTION CONCEPT WHICH EMPLOYS SEMICONDUCTOR AVALANCHE AMPLIFICATION AND THE TUNNEL DIODE ELEMENT," *Applied Physics Letters,* vol. 9, pp. 227-230, 1966.

[2]   P. P. Webb and R. J. McIntyre, "Large Area Reach-Through Avalanche Diodes for X-Ray Spectroscopy," *Nuclear Science, IEEE Transactions on,* vol. 23, pp. 138-144, 1976.

[3]   R. J. McIntyre, "Multiplication noise in uniform avalanche diodes," *Electron Devices, IEEE Transactions on,* vol. 13, pp. 164-168, 1966.

[4]   R. J. McIntyre, "The distribution of gains in uniformly multiplying avalanche photodiodes: Theory," *Electron Devices, IEEE Transactions on,* vol. 19, pp. 703-713, 1972.

[5]   G. A. Petrillo, R. J. McIntyre, R. Lecomte, G. Lamoureux, and D. Schmitt, "Scintillation Detection with Large-Area Reach-Through Avalanche Photodiodes," *Nuclear Science, IEEE Transactions on,* vol. 31, pp. 417-423, 1984.

[6]   R. Lecomte, D. Schmitt, A. W. Lightstone, and R. J. McIntyre, "Performance Characteristics of BGO-Silicon Avalanche Photodiode Detectors for PET," *Nuclear Science, IEEE Transactions on,* vol. 32, pp. 482-486, 1985.

[7]   A. W. Lightstone, R. J. McIntyre, R. Lecomte, and D. Schmitt, "A Bismuth Germanate-Avalanche Photodiode Module Designed for Use in High Resolution Positron Emission Tomography," *Nuclear Science, IEEE Transactions on,* vol. 33, pp. 456-459, 1986.

[8]   M. R. Squillante, R. Farrell, J. C. Lund, F. Sinclair, G. Entine, and K. R. Keller, "Avalanche Diode Low Energy X-Ray and Nuclear Particle Detector," *Nuclear Science, IEEE Transactions on,* vol. 33, pp. 336-339, 1986.

[9]   R. Farrell, K. Vanderpuye, G. Entine, and M. R. Squillante, "High resolution, low energy avalanche photodiode X-ray detectors," *Nuclear Science, IEEE Transactions on,* vol. 38, pp. 144-147, 1991.

[10] E. M. Gullikson, E. Gramsch, and M. Szawlowski, "Large-area avalanche photodiodes for the detection of soft x rays," *Appl. Opt.,* vol. 34, pp. 4662-4668, 1995.

[11] M. Moszynski, M. Kapusta, J. Zalipska, M. Balcerzyk, D. Wolski, M. Szawlowski, and W. Klamra, "Low energy γ-rays scintillation detection with large area avalanche photodiodes," *Nuclear Science, IEEE Transactions on,* vol. 46, pp. 880-885, 1999.

[12] M. Moszynski, M. Kapusta, D. Wolski, M. Szawlowski, and W. Klamra, "Energy resolution of scintillation detectors readout with large area avalanche photodiodes and photomultipliers," *Nuclear Science, IEEE Transactions on,* vol. 45, pp. 472-477, 1998.

[13] M. Moszynski, M. Kapusta, M. Balcerzyk, M. Szawlowski, D. Wolski, I. Wegrzecka, and M. Wegrzecki, "Comparative study of avalanche photodiodes with different structures in scintillation detection," *Nuclear Science, IEEE Transactions on,* vol. 48, pp. 1205-1210, 2001.

[14] M. Moszynski, W. Czarnacki, M. Szawlowski, B. L. Zhou, M. Kapusta, D. Wolski, and P. Schotanus, "Performance of large-area avalanche photodiodes at liquid nitrogen temperature," *Nuclear Science, IEEE Transactions on,* vol. 49, pp. 971-976, 2002.

[15] M. Moszyński, M. Szawlowski, M. Kapusta, and M. Balcerzyk, "Avalanche photodiodes in scintillation detection," *Nuclear Instruments and Methods in Physics Research Section A: Accelerators, Spectrometers, Detectors and Associated Equipment,* vol. 497, pp. 226-233, 2003.

[16] J. Kataoka, T. Saito, Y. Kuramoto, T. Ikagawa, Y. Yatsu, J. Kotoku, M. Arimoto, N. Kawai, Y. Ishikawa, and N. Kawabata, "Recent progress of avalanche photodiodes in high-resolution X-rays and -rays detection," *Nuclear Instruments and Methods in Physics Research Section A: Accelerators, Spectrometers, Detectors and Associated Equipment,* vol. 541, pp. 398-404, 2005.

[17] T. Ikagawa, J. Kataoka, Y. Yatsu, T. Saito, Y. Kuramoto, N. Kawai, M. Kokubun, T. Kamae, Y. Ishikawa, and N. Kawabata, "Study of large area Hamamatsu avalanche photodiode in a -ray scintillation detector," *Nuclear Instruments and Methods in Physics Research Section A: Accelerators, Spectrometers, Detectors and Associated Equipment,* vol. 538, pp. 640-650, 2005.

[18] T. Ikagawa, J. Kataoka, Y. Yatsu, N. Kawai, K. Mori, T. Kamae, H. Tajima, T. Mizuno, Y. Fukazawa, Y. Ishikawa, N. Kawabata, and T. Inutsuka, "Performance of large-area avalanche photodiode for low-energy X-rays and Î³-rays scintillation detection," *Nuclear Instruments and Methods in Physics Research Section A: Accelerators, Spectrometers, Detectors and Associated Equipment,* vol. 515, pp. 671-679, 2003.

[19] Y. Yatsu, Y. Kuramoto, J. Kataoka, J. Kotoku, T. Saito, T. Ikagawa, R. Sato, N. Kawai, S. Kishimoto, K. Mori, T. Kamae, Y. Ishikawa, and N. Kawabata, "Study of avalanche photodiodes for soft X-ray detection below 20keV," *Nuclear Instruments and Methods in Physics Research Section A: Accelerators, Spectrometers, Detectors and Associated Equipment,* vol. 564, pp. 134-143, 2006.

[20] H. Nakajima, H. Yamaguchi, H. Matsumoto, T. G. Tsuru, K. Koyama, S. Kissel, B. LaMarr, and M. Bautz, "The ground calibration of X-ray CCD cameras (XIS) with front-illuminated chips onboard Astro-E2," *Nuclear Instruments and Methods in Physics Research Section A: Accelerators, Spectrometers, Detectors and Associated Equipment,* vol. 541, pp. 365-371, 2005.

[21] S. Kishimoto, "High time resolution x-ray measurements with an avalanche photodiode detector," *Review of Scientific Instruments,* vol. 63, pp. 824-827, 1992.

[22] S. Kishimoto, "Recent developments in the avalanche photodiode x-ray detector for timing and fast counting measurements," *Review of Scientific Instruments,* vol. 66, pp. 2314-2316, 1995.

[23] A. Q. R. Baron and S. L. Ruby, "Time resolved detection of X-rays using large area avalanche photodiodes," *Nuclear Instruments and Methods in Physics Research Section A: Accelerators, Spectrometers, Detectors and Associated Equipment,* vol. 343, pp. 517-526, 1994.

[24] A. Q. R. Baron, R. Rüffer, and J. Metge, "A fast, convenient, X-ray detector," *Nuclear Instruments and Methods in Physics Research Section A: Accelerators, Spectrometers, Detectors and Associated Equipment,* vol. 400, pp. 124-132, 1997.

[25] A. Q. R. Baron, "Detectors for nuclear resonant scattering experiments," *Hyperfine Interactions,* vol. 125, pp. 29-42, 2000.

[26] S. Kishimoto, "Avalanche Photodiodes as Fast X-ray Detectors," *Journal of Synchrotron Radiation,* vol. 5, pp. 275-279, 1998.

[27] P. J. Sellin, "Recent advances in compound semiconductor radiation detectors," *Nuclear Instruments and Methods in Physics Research Section A: Accelerators, Spectrometers, Detectors and Associated Equipment,* vol. 513, pp. 332-339, 2003.

[28] D. S. McGregor and H. Hermon, "Room-temperature compound semiconductor radiation detectors," *Nuclear Instruments and Methods in Physics Research Section A: Accelerators, Spectrometers, Detectors and Associated Equipment,* vol. 395, pp. 101-124, 1997.

[29] A. Owens and A. Peacock, "Compound semiconductor radiation detectors," *Nuclear Instruments and Methods in Physics Research Section A: Accelerators, Spectrometers, Detectors and Associated Equipment,* vol. 531, pp. 18-37, 2004.

[30] J. Lauter, D. Protic, A. Forster, and H. Luth, "AlGaAs/GaAs SAM-avalanche photodiode: An X-ray detector for low energy photons," *Nuclear Instruments and Methods in Physics Research Section A: Accelerators, Spectrometers, Detectors and Associated Equipment,* vol. 356, pp. 324-329, 1995.

[31] J. Lauter, A. Forster, H. Luth, K. D. Muller, and R. Reinartz, "AlGaAs/GaAs avalanche detector array -1 GBit/s X-ray receiver for timing measurements," in *Nuclear Science Symposium and Medical Imaging Conference Record, 1995., 1995 IEEE*, 1995, pp. 579-583 vol.1.

[32] J. Blažej, I. Procházka, K. Hamal," Solid state photon counters based on GaAs and GaP materials," in *Eurosensors XVI—Book of Abstracts*, vol.1-3, pp. 87-88, 2002.

[33] J. E. Lees, D. J. Bassford, J. S. Ng, C. H. Tan, and J. P. R. David, "AlGaAs diodes for X-ray spectroscopy," *Nuclear Instruments and Methods in Physics Research Section A: Accelerators, Spectrometers, Detectors and Associated Equipment,* vol. 594, pp. 202-205, 2008.

[34] J. E. Lees, A. M. Barnett, D. J. Bassford, J. S. Ng, C. H. Tan, N. Babazadeh, R. B. Gomes, P. Vines, J. P. R. David, R. D. McKeag, and D. Boe, "Development of high temperature AlGaAs soft X-ray photon counting detectors," *Journal of Instrumentation,* vol. 6, p. C12007.

Chapter 2 Background theory

2.1 Introduction

This chapter explains the underlying principle of radiation interaction in semiconductors. The principles of operation of a spectrometer used for pulse height spectra analysis of energy resolving detectors are also discussed. The basic principles of impact ionisation and avalanche noise are presented. An analysis of the noise sources both intrinsic to the APD and from accompanying electronics is presented. This has been used to characterise the performance of the APDs presented in this work.

2.2 Interaction of X-rays

The interaction of X-rays with a material can occur in three major ways: photoelectric effect, Compton scattering and pair production [1]. The possibility of pair production occurs only when the photon energy is larger than twice the rest mass energy of an electron (1.02 MeV). The probability of pair production is low until the gamma ray energy approaches several MeV. Since the X-ray photons used in this work range from 5 - 60 keV, this process can be neglected. The photoelectric and Compton interactions depend on the energy of the incident photon and will involve in either a partial or complete transfer of its energy resulting in an emission of a secondary X-ray photon or an electron.

Compton scattering takes place when an incident photon interacts with an electron in the absorber. The photon is scattered thorough an angle which results in partial transfer of energy to the electron, referred to as the 'recoil' or 'Compton' electron. The photoelectric effect occurs when the interaction with the atom involves the complete transfer of the incident photon energy. An energetic 'photoelectron' is ejected in this process. Figure 2.1 shows the energy

dependence (from 1 keV – 100 MeV) of the various interaction mechanisms for photons incident on GaAs [2]. The discontinuities in the curves correspond to the binding energy of electrons in different shells of the atom. For the energy range up to 30 keV the probability of Compton Effect is negligible. Most of the results reported in the work involve the interaction of soft X-rays and hence Photoelectric effect will be considered as the dominant process of interaction.
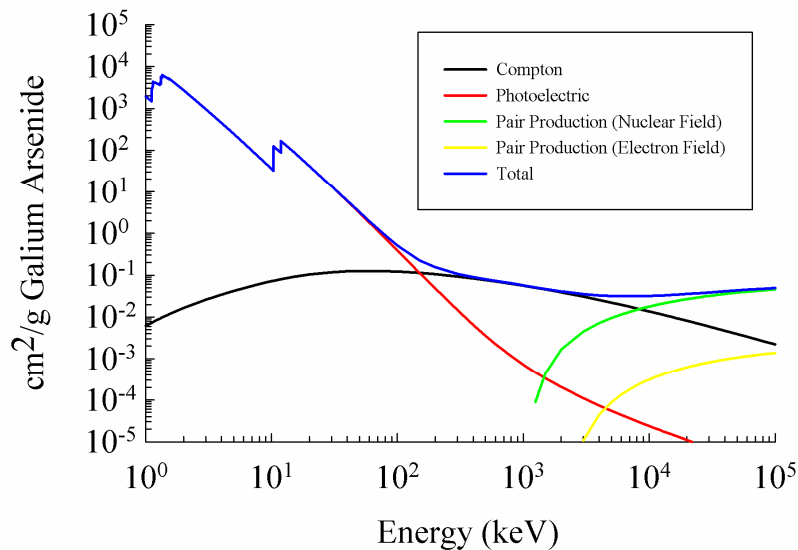
Figure 2.1 Energy dependence of the major interaction processes of X-rays with GaAs [2].

2.2.1 Photoelectric effect

Photoelectric effect is the dominant mechanism at X-ray energies (e.g. below 60 keV for Si). The interaction only occurs with an absorber atom and cannot take place with free electrons. The incident photon of energy $h\nu$ is completely absorbed and results in the ejection of a bound electron with energy given by

$$E_{e^-} = h\nu - E_{bind} , \qquad (2.1)$$
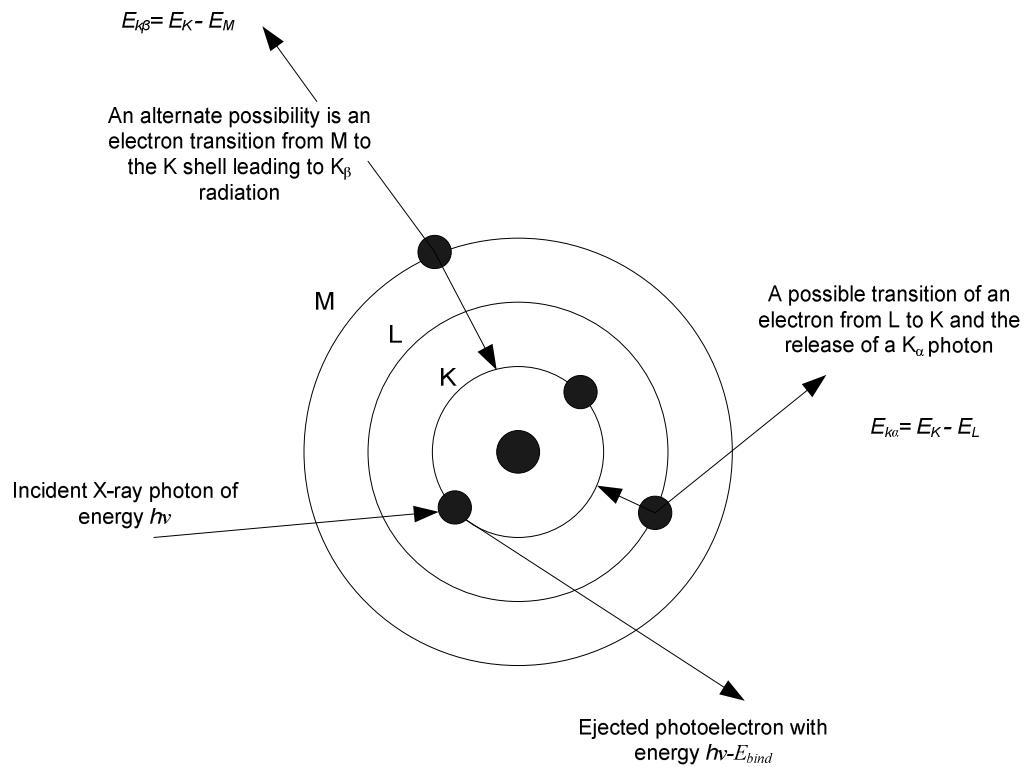
Figure 2.2 Schematic of the photoelectric effect illustrating the possible emission of characteristics X-rays. An alternative possibility is the emission of auger electrons (not shown in the schematic).

where E_{bind} is the binding energy of the electron in its original state. The photoelectric effect also results in the creation of an ionised atom with a vacancy in its bound shells. This vacancy is subsequently filled by rearrangement of the electrons. Energy is hence liberated either in the form of a characteristic X-ray or the emission of an Auger electron. A schematic of the process is shown in figure 2.2. The emission of Auger electrons is an alternative mechanism of releasing excess energy. The energy of the Auger electron, like the characteristic X-rays, depends on the electronic configuration of the ionised atom. Hence the energy of either the emitted X-ray or electron is fairly low and can range from a few 100 eV to a few keV.

The characteristic X-ray is usually reabsorbed close to the original interaction point by the photoelectric effect. If the X-rays are absorbed close to the surface, the characteristic X-ray may escape the detector without absorption

resulting in an 'escape peak' in the collected energy spectra. The ratio of the emission of secondary X-rays to the ejection of Auger electrons is dependent on the constituent atom and its fluorescence yield. The fluorescence yield is simply defined as the probability that a vacancy in a given shell will result in a radiative transition. The process is independent of incident energy. The probability of auger electrons escape is higher closer to the surface of the semiconductor.

The probability of photoelectric absorption per atom can be given by the following empirical relationship:

$$\delta \approx \frac{Z^n}{(h\nu)^{3.5}} \quad , \tag{2.2}$$

where the exponent n varies from 4 to 5, depending on $h\nu$ and Z is the atomic number. Hence the photoelectric effect increases with atomic number for a given energy. The atomic number is thus an important parameter when considering materials for X-ray detection.

The ejected photoelectron, along with the secondary electron created during the photoelectric process, will undergo multiple scattering resulting in the creation of a large number of electron-hole pairs (EHPs). These EHPs usually have kinetic energy lower than the threshold and thus are incapable of undergoing any further ionisation. They achieve equilibrium by losing their residual energy to lattice vibrations. If nothing escapes the detector the kinetic energy of the electrons created is equal to the energy of the incident X-ray. This photoelectric process is hence the most ideal process for energy resolving X-ray detectors.

2.2.2 Photon absorption

The photoelectric effect results in the complete absorption of the incident photon. The X-ray beam incident on the detector is attenuated in intensity and is given by

$$I(\zeta) = I_0 exp(-\phi\zeta) \quad , \tag{2.3}$$

where I_0 is the incident X-ray beam intensity, $I(\zeta)$ is the intensity at depth ζ and ϕ is the linear attenuation coefficient of the absorber and can be given as

$$\phi = \left(\frac{\vartheta}{\varrho}\right)\varrho \quad , \tag{2.4}$$

where ϑ/ϱ is the mass attenuation coefficient of the material (cm^2gm^{-1}) and ϱ is the density ($gmcm^{-3}$). The mass attenuation coefficient is fairly constant for different materials for a particular energy range and hence the linear attenuation coefficient is strongly dependent on the density. The probability $P(\zeta)$, that a photon is absorbed at position ζ is

$$P(\zeta) = 1 - exp(-\varphi\zeta), \tag{2.5}$$

where φ is the absorption coefficient of the material. The photoelectrons and the Auger electron undergo interaction with the electrons and nucleus of the atom. Elastic collisions can occur with the nucleus of the atoms which sometimes can result in the complete back scattering of the electrons. Interaction with loosely bound electrons in the valence or conduction band can lead to the emission of secondary electrons referred to as slow electrons. Electrons can also be generated with interaction with the more tightly bound electrons in the inner shell of the atom. This process can lead to ejection of characteristic X-rays or Auger electrons, and a fast electron, as electrons ejected from the inner shells of the atom can be of considerably high energy. In materials with free or loosely bound electrons inelastic interactions can occur with the incident electron leading to collective oscillations in the electron cloud called Plasmons.

The loss of energy of an electron through a material can be quantitatively given by the phenomenological expression first specified by Bethe [3, 4]. The 'stopping power' which gives the electron range and the spatial distribution of secondary emissions is given as

$$\frac{dE}{dx} = -785 \frac{\varrho Z}{AE} ln\left|\frac{1.166E}{G}\right|, \tag{2.6}$$

where E is the instantaneous energy of the electron (in eV), along the path length x (Å). Z is the atomic number, ϱ is the density (in gm/cm^{-3}), A is the atomic weight and G is the mean ionisation potential (in eV). The value of G can be experimentally obtained or in this case used from tabulated results obtained from analytical fitting of data by Berger and Seltzer [5] and given as,

$$G = 9.76Z + \frac{58.5}{Z^{0.18}}. \tag{2.7}$$

Figure 2.3 shows the calculated stopping power using equation (2.6) and (2.7) for GaAs as a function of increasing incident photon energy. For values of $E < G/1.166$, the equation will predict a negative stopping power which is physically impossible. Hence it is invalid for low electron energies. An empirical correction as suggested in [6, 7] can be used. The equation predicts the mean distance travelled by the electron without change of direction. In reality due to the various interaction mechanisms briefly described earlier the electron will undergo a change of direction and hence the effective disarticulation will be much shorter. To analyse this, figure 2.4 shows the realistic electron path length of 4 electron paths generated by 5.9 keV X-rays in GaAs through simulations. The X-rays are assumed to be incident normal to the surface of the sample. A Monte Carlo 'CASINO' code obtained from [8-10] has been used to simulate the interactions of electrons in GaAs. In the Monte Carlo simulation the path of an electron is followed in a step wise approach until it is completely absorbed or back scattered. The probability of electron scattering, the scattering angle, the distance between scattering events and the electron loss is computed using relevant physical models.
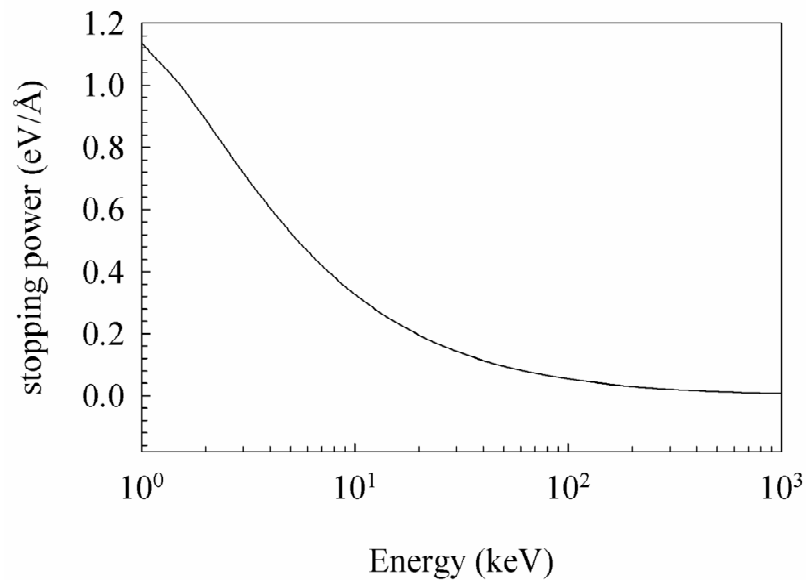
Figure 2.3 Stopping power of GaAs calculated using Bethe's equation.
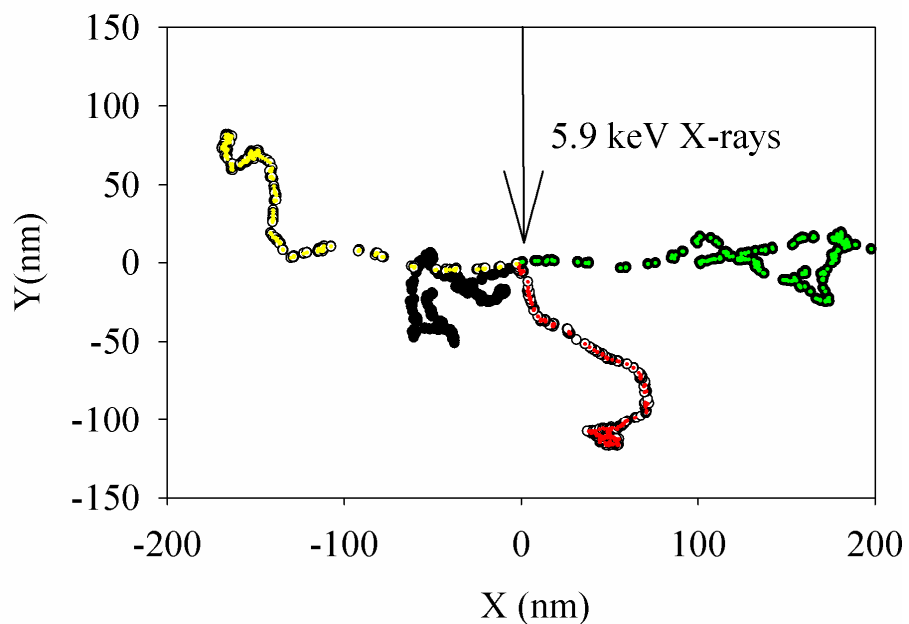
Figure 2.4 Four simulated electron path lengths created by the absorption of 5.9 keV X-rays in GaAs, The position of interaction is at the origin. The simulation accounts for the probability of elastic and inelastic scattering.

The interaction of radiation with semiconductors always leads to the creation of a large number of EHPs. The energy required to create an electron hole pair is called the pair creation energy, denoted by ε. A small value of ε

results in a large number of EHPs which makes the statistical fluctuation in the creation of charge carriers a smaller faction of the total EHPs creation, leading to an improvement in the energy resolution. The decrease in ε also helps to improve the signal to noise ratio of the detection system due to the increase in the amount of charge per pulse. Since detectors are of finite thickness, not all the generated photoelectrons, auger electrons and characteristic X-ray rays are absorbed in the detector. The escape of electrons or X-rays can lead to a considerable change in number of electrons deposited in a material for a given incident X-ray photon. For an X-ray with energy E, in a material with a pair creation energy ε, the number of EHPs created is given by $N = E/\varepsilon$, when no electrons escape the detector. For a characteristic X-ray of energy E_c that escapes the detector $N = (E - E_c)/\varepsilon$, this will result in an 'X-ray escape peak' in the pulse height spectra. The distortion in the pulse height spectra due to escape of secondary electrons depend on the kinetic energy of the escape electron.

2.3 Radiation detection systems

Radiation detection systems usually consist of a detector, a preamplifier a pulse shaping amplifier and a pulse digitising system. Certain experiments include the incorporation of alternative electronic components but the basics of the measurements remain the same. The detector converts the interaction photon energy into an electrical signal that is proportional to the energy of the incident photon. The electrical signal is coupled to a preamplifier and shaped using a pulse shaping network. The shaped signal is passed on to an analogue to digital converter for further signal processing or for pulse height analysis using a multichannel analyser (MCA). A schematic of a readout system is shown in Figure 2.5.

preamplifier   Pulse shaping

detector   ADC
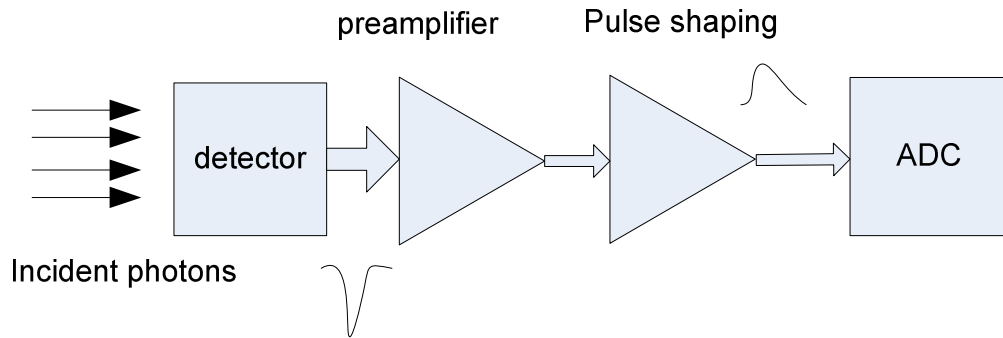
Incident photons

Figure 2.5 Block diagram of a pulse readout system for signal processing.

2.4 Detector

Radiation detection can be carried out either by direct or indirect detection. In direct detection the incident photons ionise the detector atom as in the case of solid state or gas detectors. In indirect detection the incident energy is converted to light, as in the case of scintillations. This is then converted to an electrical signal by coupling the light to a PMT or semiconductor detectors. The detectors used for radiation detection can be summarised as follows,

- **Proportional Counters** In proportional counters, ion pairs are created by the interaction of incident radiation with an inert gas like Helium or Argon. They are operated at high electric fields to amplify the charge represented by the ion pairs via the process of gas multiplication. The number of ion pairs produced is thus proportional to the incident energy (assuming negligible noise in the multiplication process).

- **Geiger-Mueller counters** also work on the gas multiplication principle similar to proportional counters but operated at much higher fields. The amplitude of the pulse obtained from a Geiger tube is independent of the incident energy and can only be operated as counters for radiation events, often without the need for external amplification due to the high gain.

- **Scintillator detectors** convert the energy of the incident high energy photons to visible light that can be measured. The total light

is proportional to the incident photon energy. Inorganic Alkali halide crystals (like Nai or CsI) are most widely used as they show good linearity and stopping power.

- **PMTs** are largely used in combination with scintillator crystals to convert the light signal into an electrical pulse. The PMT consists of a photosensitive layer called a photocathode, which converts the incident light to electrons with relatively low energy via the photoelectric effect. The second stage involves an electron multiplier section that increases the number of electrons before their collection.

- **Semiconductor detectors** (including APDs CCDs and photoconductors) offer the potential for a much lower statistical limit to the energy resolution due to the large number of EHPs created by an incident photon when compared to ionising gas chambers or scintillators. Solid state detectors offer higher quantum efficiency compared to the other detectors mentioned earlier together with a compact geometry and low power consumption. In addition APDs offer internal charge multiplication though the process of impact ionisation and hence are attractive choices for low energy gamma ray spectroscopy.

Irrespective of the type of detector used the basic attributes required for energy resolving detectors are discussed in the following sections. These define the characterisation required for various applications.

2.4.1 Energy Resolution

For detectors operating in a pulse mode, where every pulse produced provides information of the energy of the interacting quanta of radiation, a pulse height distribution can then give the energy of the interacting photon. Even for single energy X-rays, fluctuations in the pulse height spectra are produced due to the inherent response of the detector or accompanying electronics. For radiation spectroscopy where the energy distribution of the

incident radiation needs to be determined, the energy resolution is the fundamental measure of the quality of the detector.
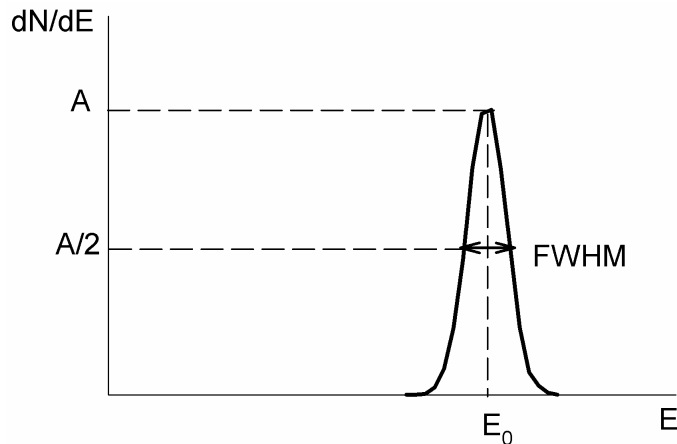
Figure 2.6 Gaussian response function of a detector with standard deviation σ to single energy X-rays. The FWHM is given as 2.36 σ. The energy resolution is thus defined as $E_R = \text{FWHM}/E_0$.

The energy resolution of a detector can be determined by measuring its response to single energy X-rays. The pulse height distribution for a hypothetical detector is shown in figure 2.6. The full width at half maximum (FWHM) is defined as the width of the function where the distribution level is half that of the peak. The energy resolution E_R is defined by the ratio of the FWHM to the centroid of the energy peak and hence a dimensionless quantity. E_R is hence given as a percentage of the detected peak energy. For detectors with good resolving capabilities the FWHM should be ideally as narrow as possible.

The response fluctuations could arise due to statistical fluctuations in the number of EHPs created in the detector. Noise from the read out electronics will also contribute to the broadening of the energy resolution. A detailed breakdown of all the significant noise sources with relevance to APDs is presented later in this chapter.

2.4.2 Detection efficiency

X-rays and gamma rays have to undergo significant interactions with the host atoms before their detection is possible. The probability of interaction reduces with increasing energy due to the increase in the mean free path length of the photon through the detector. For very low energy X-rays (<0.5 keV) a drop in the absorption probability can be obtained due to absorption of these photons in the dead layer (where EHPs created are not collected) at the surface of the detector. The number of counts produced hence can be much lower than the number of photons incident on the detector. The intrinsic efficiency of the detector can be given as,

$$\eta_{int} = \frac{number\ of\ pulses\ recorded}{number\ of\ photons\ incident\ on\ detector}. \tag{2.8}$$

The intrinsic resolution is thus independent of the geometry of the source and the distance of the source from the detector. Equation 2.8 gives the total efficiency of the detector. The number of incident photons can be determined by collimating the X-ray beam on a high efficiency reference detector (e.g. using a Si (Li) drift detector). Practically the efficiency can be calculated by integrating the area under the curve of the measured pulse height spectrum. In this method the calculated quantum efficiency will be limited by the low energy threshold of the system and as such is difficult to obtain. An alternate method is to determine the efficiency of the detected peak obtained by integrating the total area under the detected energy peak. This value is more easily obtained and in less susceptible to experimental variations and read out electronics. The intrinsic peak efficiency gives a measure of the number of events that result in complete deposition of their energy in the detector. The detection efficiency can be increased by using material with larger absorption coefficients either due to their higher atomic number or crystal density. If a material absorption edge lies in the energy region of interest a sharp increase in the absorption coefficient is seen after the edge, thus leading to a minimum in detection efficiency immediately below the absorption edge.

2.4.3 Low energy threshold

The minimum detectable energy of a detection system can be defined as the required minimum number of primary carriers, generated by the detector, to produce a count above the electronic noise floor. The electronic noise floor is dependent on the dark current of the detector and noise from the preamplifier. Detectors which offer charge multiplication can hence offer an improvement in the low energy threshold, provided their intrinsic noise is kept to a minimum. APDs operating at optimised reverse bias voltage levels can thus be useful when a low noise threshold is required. The charge multiplication reduces the effect of the amplifier voltage noise with increasing multiplication factors. Although the bulk dark current will also increase at higher gains and the stochastic nature of the avalanche process can increase the dark current contribution to the electronic noise at higher gain. Figure 2.7 shows the electronic noise peak obtained by connecting a test pulse to the preamplifier input. A GaAs/Al$_{0.8}$Ga$_{0.2}$As SAM APD is also connected at the input. As the reverse bias increases tailing in the electronic noise peak is observed suggesting a non systematic behaviour of the dark current at increasing gain.
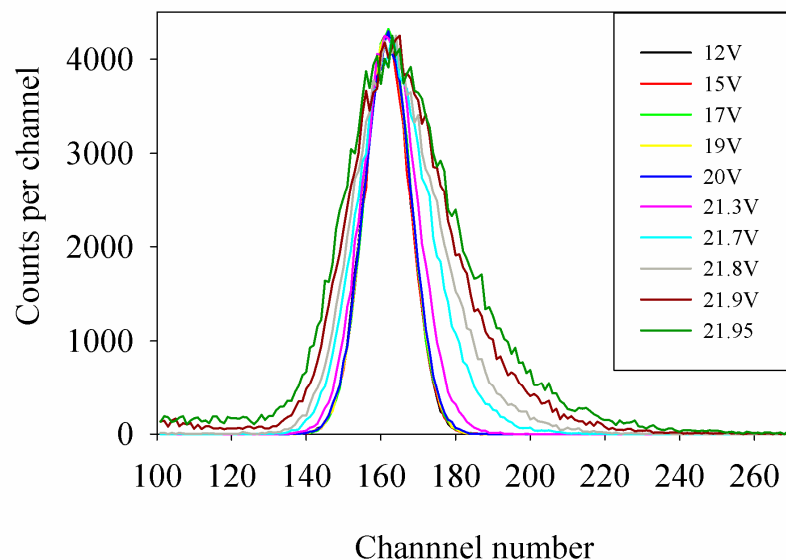
Figure 2.7 Noise peak from a pulser connected to the preamplifier input along with a GaAs/Al$_{0.8}$Ga$_{0.2}$As SAM APD connected at the input. The noise is seen to be non- Gaussian for higher gain values of the APD.

2.5 Preamplifier
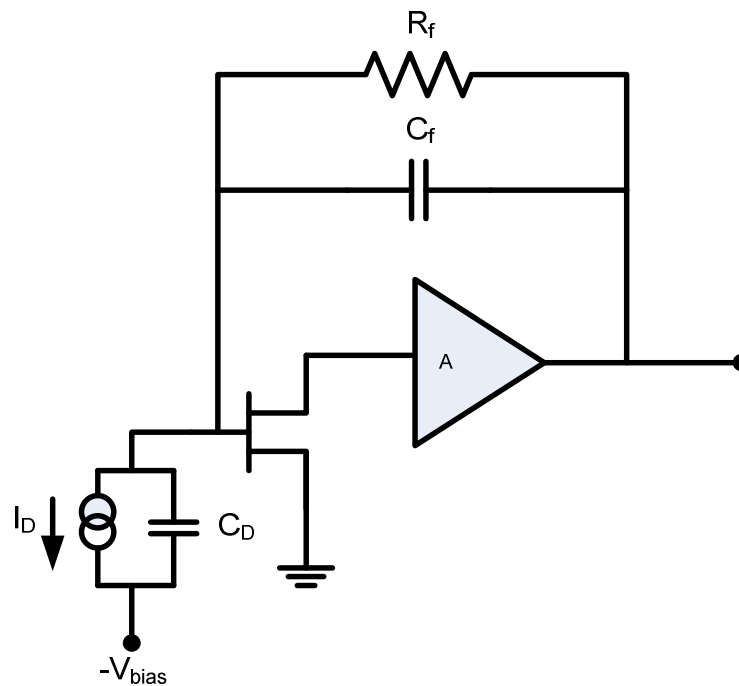
Figure 2.8 Schematic of a charge sensitive amplifier. Also shown is the equivalent circuit of a detector connected to the amplifier via an n-channel JFET at the input.

The preamplifier used in radiation detectors are known as 'charge sensitive'. The preamplifier integrates the charge from a current pulse flowing through the detector intimated by a photon absorption event. The charge integration takes place via a capacitor in the feedback loop of the amplifier; the voltage at the output is hence proportional to the charge at the input of the amplifier. Figure 2.8 shows the basic schematic of a charge sensitive amplifier. An equivalent circuit of a detector with junction capacitance, C_D, and dark current, I_D, is also shown. The feedback capacitor C_f is discharged by placing a resistor across it. Since the resistor introduces a thermal noise current source to the system its value is chosen to be as high as possible. The use of a large resistor will lead to a slow discharge of the capacitor; this can be particularly inhibiting for high count rate applications. Pulsed light or transistor reset techniques as described in [11] have previously been used as alternatives. A novel charge amplifier design that excludes the feedback resistor has been developed by Bertuccio *et al.*

that displayed noise characteristics below 20 electrons (r.m.s.) at room temperature [12].

When the input resistance is high, the time constant at the input of the amplifier is large and hence the signal pulse is determined by the integrated current and the decay time constant. Considering a charge sensitive amplifier with infinite input impedance and a gain A_0, the output voltage for an inverting amplifier configuration can be given as $v_o = -A_0 v_i$ [13]. Since the input impedance of the preamplifier is large, there is no signal flowing through the input. The difference in voltage across the feedback capacitor of the amplifier $v_f = (A_0+1)\ v_i$. The charge deposited on the feedback capacitor is hence given as $Q_f = C_f v_f = C_f\ (A_0+1)\ vi$. Since no signal flows through the input of the amplifier the charge at the input $Q_i = Q_f$ and hence the effective input capacitance of the amplifier can be given as

$$C_i = \frac{Q_i}{v_i} = C_f(A_0+1) \qquad (2.9)$$

The gain at the output per unit charge at the input of the amplifier can thus be expressed as

$$A_Q = \frac{dv_o}{dQ_i} = \frac{A_0\,v_i}{C_i v_i} = \left(\frac{A_0}{A_0+1}\right)\frac{1}{C_f} \qquad (2.10)$$

The gain of the amplifier (for $A_0 \gg 1$) is thus inversely proportional to the feedback capacitor which is well defined. Unlike voltage sensitive amplifiers the charge sensitive amplifiers output signal voltage is independent of the capacitance at the input of the detector. This configuration is thus preferred for use with detectors whose junction capacitances changes with increasing reverse bias voltage. The above analysis assumes an ideal charge sensitive preamplifier that can follow the detector pulse shape. Practical charge sensitive amplifiers might be much slower but this does not typically pose a problem as the signal is first integrated across the device and stray capacitances at the input. The time response of the amplifiers is dependent on the input resistance and the capacitance at the input. Since radiation detectors operate above the cut off

frequency of the amplifier the input impedance is resistive. The RC time constant of the preamplifier should always be larger than that of the shaping amplifier.

2.6 Shaping amplifier

The main objective of the shaping amplifier is to improve the signal to noise ratio of the detected pulses. This is achieved by reducing the bandwidth. An additional function of the shaping amplifier is to convert the short pulses from the detector into broader pulses that gradually peak at the maximum, which are then suitable as input to ADCs for pulse height analysis. The use of a larger pulse width can cause a pile up of pulses, which would make the system unsuitable for high count rate applications. Hence a compromise needs to be achieved based on the application. The reduction of pulse width for higher count rate applications would involve sacrificing low noise performance. The choice of shaping time is hence a direct compromise between good noise performance and high count rate. If the peak time of the shaper is less than the detector collection time, then loss in the pulse height occurs affecting the signal to noise ratio termed 'ballistic defect'. Apart from this the shaping amplifier also performs the rudimentary function of amplifying the signal from the preamplifier.
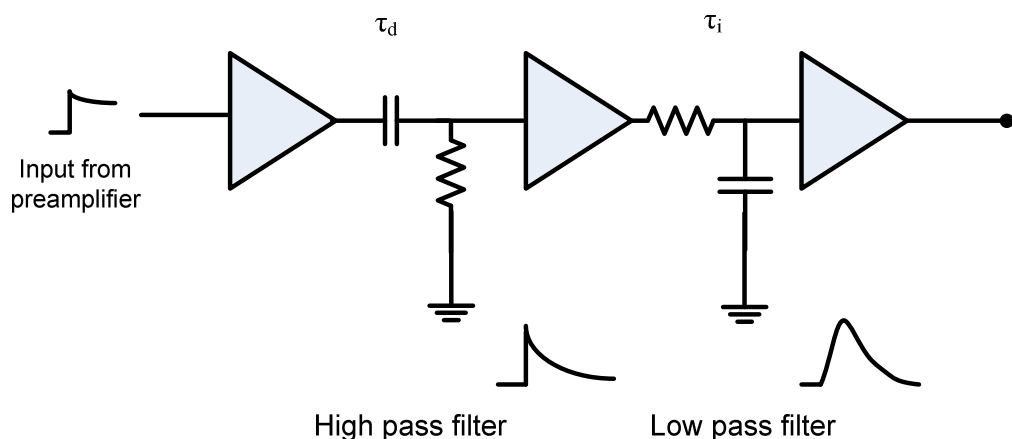

Figure 2.9 Schematic of a CR-RC pulse shaping amplifier with a differentiator as a high pass and an integrator as a low pass filter.

A simple pulse shaper is shown in figure 2.9 which has a differentiator and an integrator in cascade, also referred to as a CR-RC shaper. The low frequencies that contain a lot of noise are attenuated by the differentiator. The decay time of the pulse from the preamplifier is also shortened to avoid pulse pile up. This then passes through a low pass filter which limits the rise time to reduce the bandwidth. Practical shapers use much more sophisticated methods for shaping [14]. For semi Gaussian pulse shaping commonly employed in spectroscopy amplifiers, a differentiator stage followed by n integrator stages are used to make the pulse more symmetrical. Nonetheless the basic principles are similar to a CR-RC which introduces an upper and a lower frequency bound on the signal.

2.7 Intrinsic detector noise

The various factors that lead to the fluctuations in the pulse height spectra of a single energy X-ray photon intrinsic to the detector are discussed in the following sections.

2.7.1 Fano noise

The statistical fluctuations in the number of EHPs created during a photon interaction event places a limit on the lowest possible energy resolution achieved by a solid state detector.

The creation of each charge carrier is dependent on the history of the X-ray photon (some energy is lost via optical phonon scattering) leading to a distribution of carrier number from a given X-ray photon, as shown by Fano [15] in his paper on the fluctuations of ions created by the ionisation of gas by radiation. The fano factor f is introduced to describe the variance of a total number of charges N created during each photon interaction, such that $\overline{(N - \overline{N})^2} = f\overline{N}$. For the special case having Poissonian statistics where the variance is given by the average $\overline{N}$, $f = 1$. Hence the fano factor can be

interpreted as the ratio of the observed variance to that of a Poisson distribution. Since N for X-ray APDs is typically large, the final distribution approaches a normal distribution irrespective of the initial distribution, following the central limit theorem. The response function is given by a Gaussian with FWHM given as 2.36 times the standard deviation.

The fano limited resolution of the detector can hence be given in terms of energy as

$$E_F = 2.36\varepsilon\sqrt{fN} \tag{2.11}$$

The fano factors for semiconductor materials are much smaller than unity. Typical values obtained experimentally give the fano factor for Si = 0.12 [16], and GaAs = 0.12 [17]. In this thesis, the most accurately available experimentally obtained values of fano factor are used. In the case of unavailable experimental data, a conservative estimate of 0.14 is used. Figure 2.10 shows the fano limited energy for a range of semiconductors with increasing photon energy.
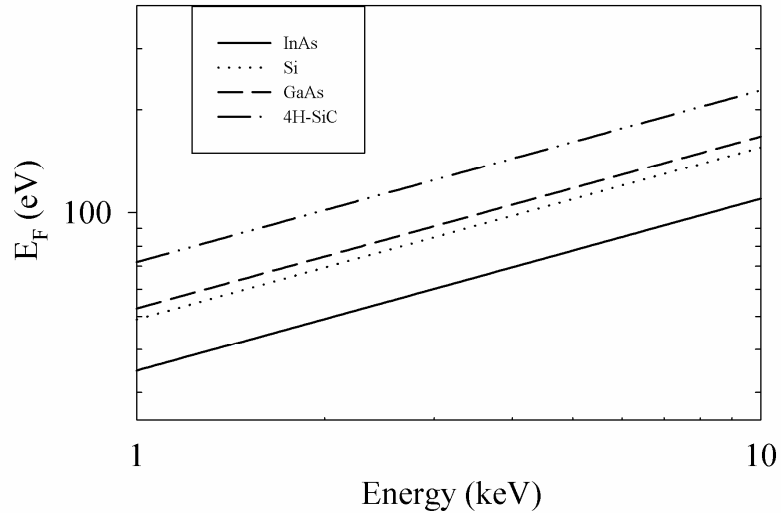

Figure 2.10 Comparison of the fano limited energy resolution with increasing incident photon energy for a range of semiconductors. f and ε for 4H-SiC obtained from [18, 19], $f = 0.14$ for InAs and ε calculated from equation 2.13 assuming $rh(\omega_R) = 0.5$ eV.

The value of ε is important to determine the number of charge carriers created and hence the statistical limit of the detector. Two different approaches have been used to calculate ε. The first approach postulated by Shockley [20] assumes that the incident energy is lost in the ionisation events that generate EHPs. In addition to this some of the energy is also lost due to phonon scatterings with the lattice before ionisation. Assuming an ionisation threshold equal to the band gap E_g, ε is given by the expression

$$\varepsilon = 2.2E_g + rh(\omega_R) , \tag{2.12}$$

where r is the number of optical (or Raman quanta $h(\omega_R)$) phonons emitted between impact ionisation events. Klein [21] showed that the average energy to create an EHP was equal to the sum of the residual kinetic energy of the carrier after ionisation $(9/5E_g)$, the bandgap and the phonon loss term to give

$$\varepsilon = 2.8E_g + rh(\omega_R) , \tag{2.13}$$

where $rh(\omega_R)$ was treated as the adjustable parameter. Klein also showed that the fano factor was dependent on the relative amount of phonon losses $(rh(\omega_R)/E_g)$. The bandgap dependence on the value of ε was shown to agree with equation 2.13 for phonon losses independent of E_g. Good agreement was found between experimental and calculated values for a range of semiconductors when $rh(\omega_R) \sim 0.5$ eV was used [21, 22]. Another approach to the calculation of ε is given in [23], referred to as the 'scattering rate assumption'. The free electron approximation is used to solve the probability of the number of EHPs created by an interacting photon. The calculated ε values are also shown to be in good agreement with experimentally obtained values.

2.7.2 Charge collection

The charges created, within the depletion region, by an X-ray detector drift under the influence of an applied voltage. The induced current per unit charge as given by Ramo's theorem [24] is collected by a charge sensitive preamplifier

at one of the electrodes of the detector. In an ideal detector the total measured charge by the preamplifier Q_M should be equal to the created charge $Q_o = Nq$ (where q is the electronic charge) such that the charge collection efficiency $\eta = Q_M / Q_o = 1$. In many semiconductors the amount of charge measured is less than the created due to the incomplete diffusion of carriers created in the non drift region of the detector or due to the loss of carriers via various trapping mechanisms

For carriers created in a region with a uniform electric field the charge collection efficiency can be calculated using the Hecht equation [25]. This is only useful at low electric fields. At higher field values the drift velocity of the carriers is less dependent on the electric field and will eventually reach a saturation velocity. APDs operate at sufficiently high fields such that the carriers reach their saturation velocity. Apart from the carriers created in the drift region, the carriers created in the field free region will diffuse through the semiconductor in an isotropic manner. Some of the charge will undergo recombination while the residual charge is injected into the depletion region of the detector. The extent of recombination is dependent on the carrier diffusion lengths. This partial collection will also lead to a broadening of the energy peak in energy resolving detectors. The diffusion of the charges from their initial point of creation will degrade the spatial distribution of detectors used from position sensitive applications.

2.7.3 Avalanche statistics

In APDs, another important factor contributing to the broadening of the energy resolution is due to the avalanche multiplication process. The stochastic nature of the process, while providing an improved signal to noise performance, can lead to considerable broadening and artefacts in the pulse height spectra under conditions discussed in chapter 4. An intensive analysis of the avalanche statistic contribution is presented in chapter 4. In the following sections the

basics of the impact ionisation process are discussed along with avalanche multiplication and noise theory.

2.8 Impact ionisation theory
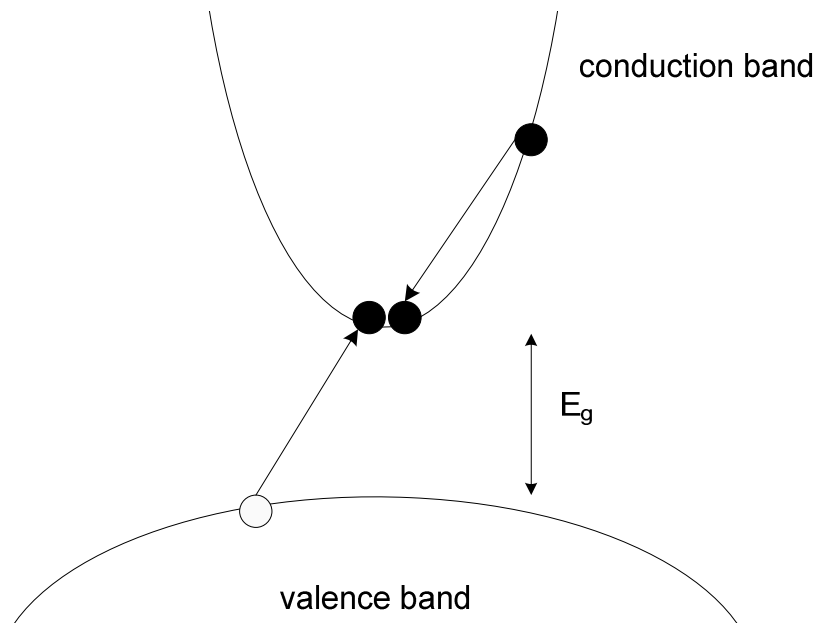
Figure 2.11 Schematic wavevector diagram illustrating an electron initiated impact ionisation event.

The process by which carriers (electrons or holes) in a reverse biased junction with high electric field lose their energy by interaction with atoms in the crystal lattice in creation of an EHP is called impact ionisation. Figure 2.11 depicts an electron initiated impact ionisation event (in the simple case of parabolic bands) whereby an electron in the conduction band that has gained energy from the electric field loses it via Coulombic interaction with an electron in the valence band thus promoting the electron to the conduction band. The newly created EHPs can further initiate impact ionisation if they accumulate sufficient energy from the electric field. A similar process occurs for hole initiated ionisation. Due to conservation of momentum and energy, a minimum threshold energy is required to create an EHP. As discussed previously the

carrier also undergoes non-ionising collisions where it can lose or gain energy from the lattice or can also undergo elastic scattering.

Carriers travel a distance, termed the dead space, to gain sufficient energy from the high field, before their energies exceed the threshold energy required to initiate impact ionisation events. After traversing the dead space a carrier has a finite ionisation probability. The distance travelled by a carrier between two successive ionisation events is called its ionisation path length. The reciprocal of the average ionisation path length gives the total number of ionisations per unit distance and is termed as its ionisation coefficient. The hole and electron ionisation coefficients given as α and β are material dependent whose values also vary with the electric field.

2.8.1 Avalanche multiplication

Impact ionisation process can occur in cascade producing a finite number of secondary carriers which leads to an increase in current. Figure 2.12 illustrates the avalanche multiplication process for an electron injected into an avalanche region of a p^+in^+ diode with a uniform electric field across its width, w. The electron injected at $z = 0$ travels a random ionisation path length before it impact ionises to create an EHP. The newly created secondary electron like the primary has an ionisation probability that is mutually exclusive of the primary electron. The secondary hole will also ionise after travelling a random ionisation path length. This process is repeated until all the electrons (holes) exit the avalanche region at $z = w$ (0). In the example shown in figure 2.12, a single electron injected results in a collection of five electrons; hence a multiplication factor of five is obtained.

The conventional expression for the mean multiplication factor M as given by Stillman and Wolfe [26] assume that the ionisation probability for the
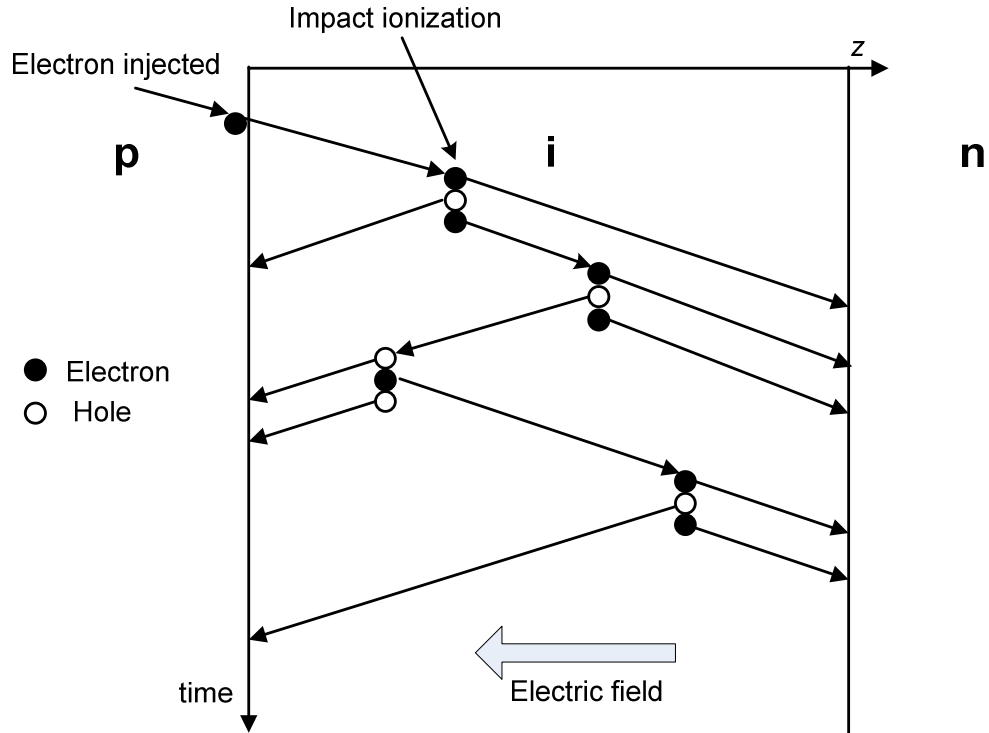
Figure 2.12 Schematic of an electron initiated ionisation process of a p^+in^+ diode with a uniform electric field across its width, w.

electron and hole depend only on the local electric field, an assumption that has been shown to be valid for diodes with thick avalanche regions. Hence the position dependent multiplication factor for a primary carrier created within w at x is given as,

$$M(x) = \frac{exp\left(-\int_0^x \left[\alpha(x') - \beta(x')\right] dx'\right)}{1 - \int_0^w \alpha(x') \, exp\left(-\int_0^x \left[\alpha(x') - \beta(x')\right] dx'\right) dx} \tag{2.14}$$

For pure electron or hole injection at $x = 0$ or w respectively, equation 2.14 reduce to

$$M_e = M(0) = \frac{1}{1 - \int_0^w \alpha(x') \, exp\left(-\int_0^x \left[\alpha(x') - \beta(x')\right] dx'\right) dx} \tag{2.15}$$

32

$$M_h = M(w) = \cfrac{1}{1 - \int\limits_0^w \beta(x') \, exp\left(- \int\limits_0^x [\alpha(x') - \beta(x')] \, dx'\right) dx} \qquad (2.16)$$

where M_e and M_h are the mean multiplication factors obtained under the pure electron and pure hole injection conditions respectively. For an avalanche region with a uniform electric field profile the ionisation coefficients are no longer dependent on the field and hence 2.14 simplifies to

$$M(x) = \frac{(\alpha - \beta) exp(- (\alpha - \beta)x)}{exp(- (\alpha - \beta)w) - \beta} \qquad (2.17)$$

M_e and M_h can hence be deduced for $x = 0$ and w respectively.

2.8.2 Avalanche excess noise

Impact ionisation is a stochastic process and hence the avalanche gain fluctuates about its mean value M. The fluctuations occur due to the randomness in the position of ionisation of carriers, as well as the number of secondary carriers created in each ionisation chain. This adds noise in addition to the shot noise associated with the diode. This is characterised by an excess noise factor F given by

$$F = 1 + \frac{\sigma_g^2}{<g>^2} \quad , \qquad (2.18)$$

where $\sigma_g^2 = <g^2> - <g>^2$, is the standard deviation of a multiplication event with mean gain $<g> = M$. Thus rearranging the above equation

$$F = \frac{<g^2>}{M^2} \quad . \qquad (2.19)$$

The mean square noise current for pure electron injection is thus given as

$$N = 2qI_{in}M_e^2F \quad , \qquad (2.20)$$

where I_{in} is the injected current. The noise spectral density for pure electron, Ψ_e and hole Ψ_h initiated impact ionisation process are given by McIntyre [27] using a local approximation as

$$\psi_e = 2qI_{in}M_e{}^3\left[1-(1-k)\frac{(M_e-1)^2}{M_e{}^2}\right] \tag{2.21}$$

$$\psi_h = 2qI_{in}M_h{}^3\left[1+\frac{(1-k)}{k}\frac{(M_h-1)^2}{M_h{}^2}\right] \quad , \tag{2.22}$$

where $k = \beta/\alpha$. The excess noise factors F_e and F_h as a function of gain can thus be given as

$$F_e = kM_e + (1-k)\left(2-\frac{1}{M_e}\right) \tag{2.23}$$

$$F_h = \frac{M_h}{k} + \left(1-\frac{1}{k}\right)\left(2-\frac{1}{M_h}\right) \tag{2.24}$$

From the above equations it can be seen that the excess noise factor is dependent on the type of carrier injection and the value of k. In order to achieve a low excess noise factor, the values of the ionisation coefficients should be disparate and the ionisation process has to be initiated by the strongly ionising carrier. As the electric field increases the ionisation coefficients converge and hence a large excess noise is predicted. However many III – V semiconductors have shown lower excess noise, despite the ionisation coefficients convergence, when the avalanche region thickness is reduced. This is because the dead space occupies a significant portion of the avalanche region width, leading to reduction of the variance of the ionisation path length PDF. Hence the local model overestimates the excess noise in thin avalanche regions. Non local models are used to determine gain and excess noise factors by accounting for the dead space effect, as discussed further in chapter 4.

2.9 Electronic Noise

This section deals with the noise added to the measurement of the induced charge by ionising radiation in the detector. This is differentiated from the intrinsic noise of the detector arising from statistics of energy loss, charge multiplication and collection. Referred to as the 'electronic noise' it can arise from the electronic circuit components and the detector. For the noise analysis a charge sensitive amplifier with a JFET at the input is employed. A quasi Gaussian pulse shaping network is used for improving the signal to noise ratio of the preamplifier pulse. For diodes which operate at unity gain or for APDs operating at low gain values, the preamplifier is the most important source of noise. Noise introduced between the APD and the input FET will also contribute to the energy resolution of the detector.
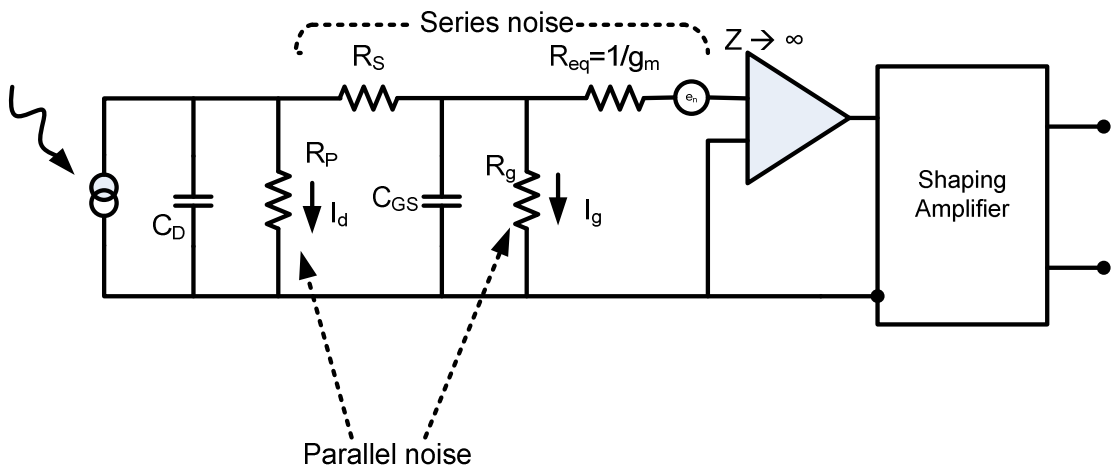
Figure 2.13 Equivalent circuit of the diode connected to a preamplifier with a JFET at the input for noise analysis. The signal from the preamplifier is given to a pulse shaping circuit.

A schematic of the equivalent circuit diagram for noise analysis is shown in figure 2.13 [28]. The noise is classified as series or parallel noise, according to its origin with respect to the signal. The total leakage current of the diode I_d is represented as a current noise generator in parallel with the detector capacitance C_D. R_P represents the effective shunt resistance across the detector

which includes the detector biasing resistor. The bias resistor R_b is connected to the detector along with a shunt capacitor that blocks any interference from the SMU. Since the shunt capacitor appears to have low impedance for high frequency signals the far end of R_b can be assumed to be connected to ground. R_b has noise behaviour similar to that of the shot noise from the detector leakage current. To limit the noise, R_b should have a large value. Since R_b is in parallel with the detector its resistance should be large such that the detector does not discharge through it. Ideally $R_b C_D >> \tau_p$, the peaking time of the shaping amplifier. If $R_b C_D$ is smaller than τ_p then most of the signal will be lost through discharge through R_b. A very large bias resistor is used to block the flow of the charge signal. For detector with high leakage current, the bias resistor value has to be reduced to minimise the voltage drop across it. The series resistance of the diode R_S acts a voltage noise source and thus contributes to the series noise in the system. The series noise largely stems from the voltage noise of the input JFET.

The noise is expressed in terms of its equivalent noise charge (ENC). This is defined as the value of a delta like charge signal that must be applied at the input to produce a signal to noise ratio of unity. ENC can be expressed in Coulombs, number of electrons or expressed in terms of energy (eV). For noise analysis the charge sensitive amplifier is considered to be coupled to a shaping amplifier with a single differentiating stage and n integration stages in cascade. With a shaping time constant τ the noise equivalent charge, Q_n, is given by [29, 30],

$$Q_n = \frac{\sqrt{b_n}}{a_n} \sqrt{\left[S_0 \tau + \frac{S_1}{4\pi n b_n} + \frac{S_2}{(2n-1)\tau} + \ldots \right]} \ , \tag{2.25}$$

where $a_n = n^n e^{-n/n!}$ is the maximum value of $\tau I(t)$, where $I(t)$ is the impulse response of the amplifier. $S(\omega) = (S_0 + S_1\omega + S_2\omega^2 + \ldots)$ is the noise current spectral density at the input and b_n is given by

$$b_n = \frac{(2n)!}{(2^{n+1} n!)^2} \, .$$ (2.26)

The charge generated at the input is far from a delta like function and is of finite shape and duration, dependent on the impulse response function of the detector. The term a_n is thus replaced by a_n', which accounts for the transit time of holes, τ_h, across the depletion region of the device and is given by,

$$a_n' = \frac{1}{a_n} + \frac{\tau_h}{\tau} \, .$$ (2.27)

Neglecting the frequency dependent noise contribution, (which is generally much smaller than the other sources of noise in the system [31]) the main contribution to $S(\omega)$ are from S_0 and S_2 which are respectively the parallel and series noise contribution from the detector-preamplifier system. It can be seen from equation 2.25, that the parallel contribution is proportional to the shaping time constant and the series noise contribution is inversely proportional to the shaping time. The contribution of sources of noise to S_0 and S_2 for a preamplifier with an APD connected to it via an input JFET is analysed in the following section. An expression for the total ENC is eventually derived.

The main contribution to S_0 is from the shot noise originating from the leakage current of the APD. McIntyre has analysed the noise spectral density of APDs [27]. The spectral density of the leakage current contribution is qualitatively given as [32]

$$s_d = 2q(I_{ds} + M^2 F I_{db}) \, ,$$ (2.28)

where I_{ds} is the unmultiplied component of the dark current termed as 'surface leakage' current. I_{db} is the portion that does get multiplied called the 'bulk leakage' current of the APD. F and M are the avalanche excess noise and multiplication factor of the APD respectively. F for electron injection is given by equation 2.23.

The value of F and M derived from the signal created by the incident radiation will not be equal to that from thermally ejected EHPs. This is due to the difference in the spatial generation of the carriers by the two processes. These factors can be assumed to be equal, if the majority of noise and signal are generated before the avalanche region of the APD [33]. Other sources of parallel noise are from shot noise due to the gate leakage current, I_g, of the JFET with spectral density $2qI_g$. This can be a few orders lower than the detector leakage current and in some systems its contribution will be negligible. The contribution from the effective resistance in parallel with the detector can be given as $4k_bT/R_p$. The total spectral density of the parallel noise is thus given by

$$S_0 = 2q(I_{ds} + M^2FI_{db} + I_g) + \frac{4k_bT}{R_p} .$$
(2.29)

These expressions are derived assuming a single value of F and M. The effects of this assumption are further analysed in chapter 4. Nevertheless they provide useful indication of the sources on noise in the spectrometer. As stated before, the contribution to S_2 is mainly from the thermal noise affecting the drain current of the preamplifier whose noise spectral density can be given as

$$e_n = \gamma \frac{4k_bT}{g_m} \quad ,$$
(2.30)

where γ is a constant whose value lies between 0.5 and 0.7, depending on the gate length and bias conditions of the JFET [34], and g_m is the transconductance. The noise associated with the series resistance of the APD is in series with the other noise sources so its contribution is simply given as $4k_bTR_S$. Apart from the white noise there is also a frequency dependent $1/f_f$ noise. This appears as a fluctuation in charge at the gate channel interface. The $1/f_f$ noise in JFETs is small and is neglected in this analysis. For an APD-preamplifier system with total input capacitance C_T which includes the APD capacitance C_D, the JFET capacitance C_{GS}, the feedback capacitor C_f and any stray capacitances, C_i at the input, the series white noise spectral density is given as [11],

$$S_2 = 4k_bTR_SC_D{}^2 + e_n{}^2C_T{}^2 \quad . \tag{2.31}$$

ENC_n, which is given as the total number of electrons required to achieve a signal to noise ratio of unity with an APD operating at gain M, is given as

$$ENC_n = \frac{\sqrt{b_n}}{qa_n}\sqrt{\left[\left(\frac{2q(I_{ds}+I_g)}{M^2}+FI_{db}+\frac{4k_bT}{R_pM^2}\right)\tau + \frac{4k_bTR_SC_D{}^2+e_n{}^2C_T{}^2}{(2n-1)M^2\tau}\right]} \quad . \tag{2.32}$$

The broadening of the X-ray peak due to the electronic noise contribution can be hence given as

$$E_N = 2.36\varepsilon ENC_n \quad . \tag{2.33}$$
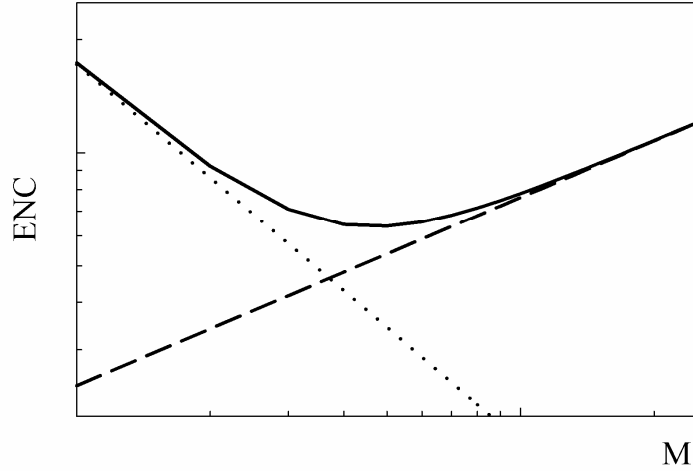
Figure 2.14 ENC dependence on the M, The series noise contribution (dotted) decreases with increasing gain while the parallel (dashed) contribution increases. The total contribution is also shown (solid).

Figure 2.14 shows the dependence of the noise components on the avalanche gain of the APD. For small gain values, the series noise is the dominating factor, hence a low noise amplifier is ideal for this purpose. As the gain increases, the dependence on the amplifier noise reduces while the parallel noise contribution increases. The parallel noise increases due to the increasing dark

current at higher gains. Thus an ideal operating point exists where the series and white noise are comparable.

2.10 References

[1]   G. F. Knoll, *Radiation detection and measurement*: John Wiley & Sons, Inc, 2002.

[2]   J. H. Hubbell and S. M. Seltzer, "Tables of x-ray mass attenuation coefficients and mass energy-absorption coefficients 1 keV to 20 meV for elements z = 1 to 92 and 48 additional substances of dosimetric interest. ," vol. http://www.nist.gov/pml/data/xraycoef/index.cfm, 1995.

[3]   H. Bethe, "Zur Theorie des Durchgangs schneller Korpuskularstrahlen durch Materie," *Annalen der Physik,* vol. 397, pp. 325-400, 1930.

[4]   H. Bethe and J. Ashkin, "Passage of radiations through matter," *Experimental Nuclear Physics (ESegrè, Ed). ,* vol. 1, 1953.

[5]   S. M. Seltzer and M. J. Berger, "Evaluation of the collision stopping power of elements and compounds for electrons and positrons," *The International Journal of Applied Radiation and Isotopes,* vol. 33, pp. 1189-1218, 1982.

[6]   D. C. Joy and S. Luo, "An empirical stopping power relationship for low-energy electrons," *Scanning,* vol. 11, pp. 176-180, 1989.

[7]   T. S. Rao-Sahib and D. B. Wittry, "X-ray continuum from thick elemental targets for 10–50-keV electrons " *Journal of Applied Physics,* vol. 45, pp. 5060-5068, 1974.

[8]   D. Drouin, P. Hovington, and R. Gauvin, "CASINO: A new monte carlo code in C language for electron beam interactions—part II: Tabulated values of the mott cross section," *Scanning,* vol. 19, pp. 20-28, 1997.

[9]   P. Hovington, D. Drouin, and R. Gauvin, "CASINO: A new monte carlo code in C language for electron beam interaction —part I: Description of the program," *Scanning,* vol. 19, pp. 1-14, 1997.

[10]   P. Hovington, D. Drouin, R. Gauvin, D. C. Joy, and N. Evans, "CASINO: A new monte Carlo code in C language for electron beam interactions—part III: Stopping power at low energies," *Scanning,* vol. 19, pp. 29-35, 1997.

[11]   F. S. Goulding and D. A. Landis, "Signal Processing for Semiconductor Detectors," *Nuclear Science, IEEE Transactions on,* vol. 29, pp. 1125-1141, 1982.

[12]   G. Bertuccio, P. Rehak, and D. Xi, "A novel charge sensitive preamplifier without the feedback resistor," *Nuclear Instruments and Methods in Physics Research Section A: Accelerators, Spectrometers, Detectors and Associated Equipment,* vol. 326, pp. 71-76, 1993.

[13]   H. Spieler, "Front-End Electronics and Signal Processing," *AIP Conference Proceedings,* vol. 674, pp. 76-100, 2003.

[14]   F.S, Goulding "Pulse-shaping in low-noise nuclear amplifiers: A physical approach to noise analysis," *Nuclear Instruments and Methods,* vol. 100, pp. 493-504, 1972.

[15] U. Fano, "Ionisation Yield of Radiations. II. The Fluctuations of the Number of Ions," *Physical Review,* vol. 72, pp. 26-29, 1947.

[16] F. Perotti and C. Fiorini, "Observed energy dependence of Fano factor in silicon at hard X-ray energies," *Nuclear Instruments and Methods in Physics Research Section A: Accelerators, Spectrometers, Detectors and Associated Equipment,* vol. 423, pp. 356-363, 1999.

[17] G. Bertuccio, A. Pullia, J. Lauter, A. Forster, and H. Luth, "Pixel X-ray detectors in epitaxial gallium arsenide with high-energy resolution capabilities (Fano factor experimental determination)," *Nuclear Science, IEEE Transactions on,* vol. 44, pp. 1-5, 1997.

[18] G. Bertuccio and R. Casiraghi, "Study of silicon carbide for X-ray detection and spectroscopy," *Nuclear Science, IEEE Transactions on,* vol. 50, pp. 175-185, 2003.

[19] G. Bertuccio, S. Caccia, R. Casiraghi, and C. Lanzieri, "Possibility of Subelectron Noise With Room-Temperature Silicon Carbide Pixel Detectors," *Nuclear Science, IEEE Transactions on,* vol. 53, pp. 2421-2427, 2006.

[20] S. William, "Problems related to p-n junctions in silicon," *Solid-State Electronics,* vol. 2, pp. 35-67, 1961.

[21] C. A. Klein, "Bandgap Dependence and Related Features of Radiation Ionisation Energies in Semiconductors," *Journal of Applied Physics,* vol. 39, pp. 2029-2038, 1968.

[22] R. C. Alig and S. Bloom, "Electron-Hole-Pair Creation Energies in Semiconductors," *Physical Review Letters,* vol. 35, pp. 1522-1525, 1975.

[23] R. C. Alig, S. Bloom, and C. W. Struck, "Scattering by ionisation and phonon emission in semiconductors," *Physical Review B,* vol. 22, pp. 5565-5582, 1980.

[24] S. Ramo, "Currents Induced by Electron Motion," *Proceedings of the IRE,* vol. 27, pp. 584-585, 1939.

[25] K. Hecht, "Zum Mechanismus des lichtelektrischen Primärstromes in isolierenden Kristallen," *Zeitschrift für Physik A Hadrons and Nuclei,* vol. 77, pp. 235-245, 1932.

[26] G. E. Stillman and C. M. Wolfe, *Avalanche photodiodes* vol. 12: Academic Press, Inc., 1977.

[27] R. J. McIntyre, "Multiplication noise in uniform avalanche diodes," Electron Devices, IEEE Transactions on, vol. 13, pp. 164-168, 1966.

[28] V. Radeka, "LOW-NOISE TECHNIQUES IN DETECTORS," Annual Review of Nuclear and Particle Science, vol. 38, pp. 217-277, 1988.

[29] J. L. Blankenship, "Design of Low-Noise Vacuum-Tube Pulse Amplifiers for Semiconductor Radiation-Detector Spectroscopy," Nuclear Science, IEEE Transactions on, vol. 11, pp. 373-381, 1964.

[30] G. A. Petrillo, R. J. McIntyre, R. Lecomte, G. Lamoureux, and D. Schmitt, "Scintillation Detection with Large-Area Reach-Through Avalanche Photodiodes," Nuclear Science, IEEE Transactions on, vol. 31, pp. 417-423, 1984.

[31] E. Gramsch, K. G. Lynn, M. Weber, B. DeChillo, and J. R. McWilliams, "Silicon PIN photodetectors in high resolution nuclear spectroscopy," Nuclear Instruments and Methods in Physics Research Section A:

Accelerators, Spectrometers, Detectors and Associated Equipment, vol. 311, pp. 529-538, 1992.

[32] P. P. Webb and R. J. McIntyre, "Large Area Reach-Through Avalanche Diodes for X-Ray Spectroscopy," Nuclear Science, IEEE Transactions on, vol. 23, pp. 138-144, 1976.

[33] P. J.P., "Avalanche photodiodes for particle detection," Nuclear Instruments and Methods in Physics Research Section A: Accelerators, Spectrometers, Detectors and Associated Equipment, vol. 387, pp. 186-193, 1997.

[34] F. M. Klaassen, "Characterisation of low 1/f noise in MOS transistors," Electron Devices, IEEE Transactions on, vol. 18, pp. 887-891, 1971.

Chapter 3 Experimental methods for characterisation of X-ray APDs

3.1 Introduction

The X-ray APDs presented in the work were evaluated for their dark current-voltage (I-V) characteristics. Capacitance–voltage(C-V) characteristics were determined to estimate the doping profile and depletion width. Photomultiplication measurements were performed to measure the avalanche gain with increasing reverse bias. A simple spectrometer to determine the performance of the APD as an X-ray detector has been set-up and described in this chapter along with other electrical characterisation techniques. The dark current and capacitance contribute to the parallel and series white noise respectively as detailed in chapter 2.

3.2 Electrical characterisation

3.2.1 I-V measurements

Dark current measurements are the fundamental way of accessing the shot noise performance of an APD. The shot noise contributes to the parallel white noise of the spectrometer and is detrimental to both the energy resolution and signal to noise ratio of the system. Additionally dark I-V measurements are used to determine the leakage current mechanism and breakdown voltage, V_{bd}, of the detector among other elementary characteristics.

The I-V measurements were carried out using an HP 4140B picoammeter. Measurements were carried out on several devices in the dark in order to avoid the photogeneration of carriers. The dark current density, J_D, was obtained from

reverse biased I-V measurements. Bulk leakage current mechanism dominates when the measured J_D across different sized devices is in good agreement. The bulk currents are proportional to the device area and can be due to the diffusion current I_{diff}, generation-recombination current, I_{gr}, and tunnelling current, I_{tunn}. At higher electric fields I_{tunn} increases at a much faster rate than I_{diff} and I_{gr}. It is particularly significant in narrow band gap materials due to band to band tunnelling, which reduces the useful operating gain region of the detector for X-ray spectroscopy.

The diodes presented in the thesis were produced by etching epitaxially grown planar structures into mesa devices. The abrupt discontinuities in the crystal structures arising from the exposed mesa side walls give rise to surface states. Moreover the formation of native oxides on the sidewalls can create a conduction path along the interface. This gives rise to surface leakage currents on the perimeter of the mesa. When the surface leakage current dominates, J_D is no longer related simply to the area but also involves a term related to device parameter.

The ideal forward current diode equation can be given as

$$I_f(V) = I_D exp\left(\frac{qV}{nk_bT} - 1\right),$$
(3.1)

where k_b is the Boltzmann's constant, T is the temperature and n is the ideality factor with ranges from a value between 1 and 2 depending on the diffusion and recombination currents [1]. A deviation from the ideal exponential increase in current is seen in diodes with series resistance. The series resistance can arise from the bulk of the semiconductor or formed between the deposited metal contact and the semiconductor. Contact resistance can be minimised by choosing an appropriate metal to form ohmic contacts and by thermal annealing after deposition. A large series resistance can control the voltage drop across the depletion region of the diode and hence limit its maximum achievable avalanche

gain. For X-ray detectors the series resistance contributes to the series white noise and needs to be evaluated.

X-ray characterisation of the diodes was carried out by packaging the diodes on TO-5 headers bonded using gold wires. A Keithley 236 or 2400 source measurement unit (SMU) was used to measure the leakage current and bias the packaged diodes. This allowed assessment of the degradation caused by the packaging process. For low temperature measurements the packaged diode were placed in a modified metal Dewar with a liquid nitrogen jacket for cooling the detector to 77 K.

3.2.2 C-V measurements

Doping profile and the depletion region width, w, of the diodes were determined by performing C-V measurements using a HP 4275 LCR meter. A sinusoidal ac signal of 50 mV at a frequency of 1 MHz superimposed over the bias voltage was used to drive the diode. Capacitance of the diode was determined from the measured impedance by the LCR meter by using one of the parallel or series equivalent circuit configurations. The series measurement circuit was employed for devices with high capacitances and the parallel measurement circuit was used for lower capacitances. Since the diodes presented in the work have capacitance up to a few tens of pico farads the parallel circuit configuration is chosen. C-V measurements were performed on devices with different sizes to check if the capacitance scaled with area.

For a one sided abrupt junction the depletion region width, W_D, for a reverse biased junction with voltage, V, is given as

$$W_D = \sqrt{\frac{2\varepsilon_s}{qN_o}\left(V_{bi} + V - \frac{2k_bT}{q}\right)} \ , \tag{3.2}$$

where V_{bi} is the built in potential, ε_s is the permittivity of the semiconductor and N_0 is the doping concentration of the depletion region. The term $2kT$ is used as a correction factor for the majority carrier diffusion tail at the edge of
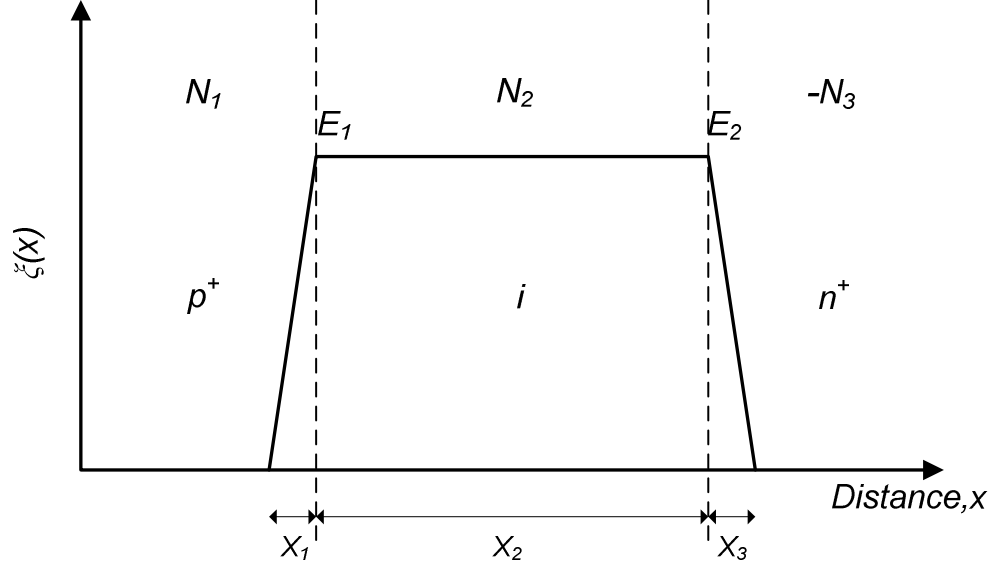

Figure 3.1 Electric field profile of an abrupt 3 region diode.

the depletion region. The capacitance of the junction with area, A_j, and depletion width W_d is hence given as

$$C = \frac{\varepsilon_s A_j}{W_d} \quad .$$ (3.3)

The doping profiles of the diodes presented in the thesis were estimated by solving Poisson's equation. Three regions for the p^+in^+ diodes and five abrupt regions for the SAM APDs were assumed. The electric field gradient in each region is hence given as

$$\frac{d\xi}{dx} = \frac{qN_0}{\varepsilon_s} \quad ,$$ (3.4)

where ξ is the electric field across the region and ε_s is the permittivity of the material. For a diode with a p^+in^+ structure as shown in figure 3.1 the doping profiles can be estimated. N_1, N_2, $-N_3$ are the doping concentrations of the p^+, i and n^+ regions respectively (where the negative sign indicated n type doping).

For an ideal p^+in^+ structure the capacitance is inversely proportional to the intrinsic region width, w_i, when fully depleted. The depletion width is generally longer than w due to the depletion in the cladding layers. The depletion region widths X_1, X_2 and X_3 were then obtained by calculating $\xi(x)$ (see Appendix A). The calculated capacitance was fitted to the experimental data by adjusting the values of the doping densities N_1, N_2 and $-N_3$ along with the intrinsic region thickness. A similar approach was used to determine the doping profile for a SAM APD structure.

3.3 Photomultiplication measurements

Photocurrent measurements were performed on a reverse biased diode using the set up shown in figure 3.2. Light from the laser was focused on the top of the diodes using a microscope objective. The focusing of the laser ensures that the light does not fall on the edge of the mesa structures giving rise to mixed injection of carriers. A white light source was aligned along with a beam splitter to aid the focusing of the device captured via a camera and displayed on a monitor. The photoresponse of the diode was measured as function of bias provided by a Keithley 236 or 237 SMU. Measurements were performed at different incident power to ensure primary photocurrents were independent of incident power and negate any heating effects on the value of multiplication obtained.

The primary photocurrent increases with bias due to the increasing collection efficiency. Since the depletion region increases with bias it reduces the distance travelled by the minority carries towards the edge of the depletion region and hence the increase in primary photocurrent [2]
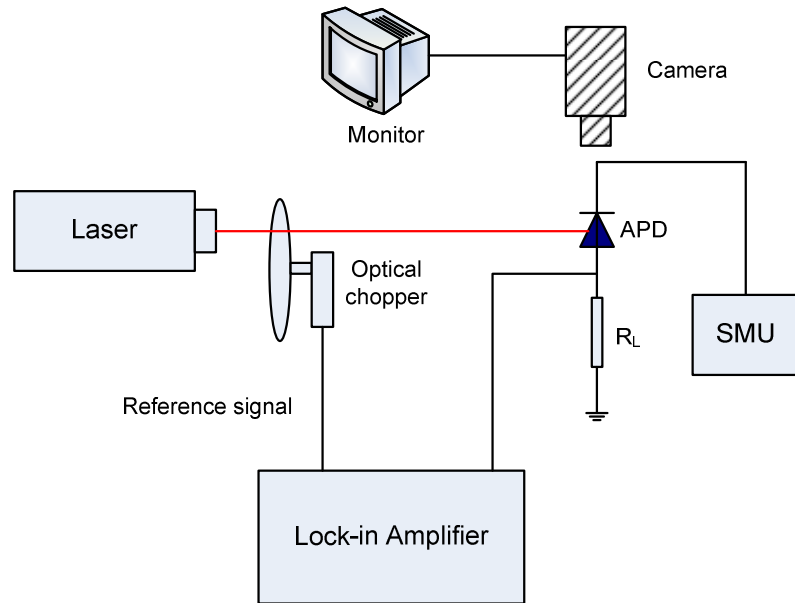
Figure 3.2 Schematic of an AC photomultiplication measurement setup.

For cases where the dark current was significantly lower (2-3 orders) than the primary photocurrent, DC measurements were performed to determine the multiplication factor. A SMU was used to measure the dark current and the total current under illumination of the laser. The dark current was then subtracted from the total current to obtain the multiplied photocurrent. For devices where the dark currents were higher, phase sensitive (AC) measurements were used. This technique allows for measurement of photocurrent levels of a few orders of magnitude lower than the dark currents.

Figure 3.2 shows the schematic diagram of the setup used for phase sensitive measurements. Light from the laser was modulated at 180 Hz using a mechanical chopper. The photocurrent was sensed by measuring the voltage drop across the series resistor, R_L, using a Stanford Research 830 Lock-in Amplifier (LIA). The chopping reference frequency was also supplied to the LIA. I_{ph} is hence simply given as V_{ph}/R_L. The value of R_L was also chosen such that a sufficiently large voltage drop appears across the resistor ($\sim\mu V$) while also ensuring that most of the applied voltage was dropped across the device.

3.4 Simple X-ray spectrometer

X-ray characterisation involves the determination of the pulse height spectra of the APD irradiated with characteristic X-ray photons. The spectral resolution of the detected energy peaks, low energy threshold and signal to noise ratio are determined from these measurements.

A simple X-ray spectrometer is shown in figure 3.3. The system comprises of the detector placed 0.5 cm away from an X-ray source along with its bias voltage supply, a charge sensitive preamplifier, a shaping amplifier and the multichannel analyser (MCA) interfaced via USB to a computer running the software required to build the pulse height spectra. The pulse generator along with the test capacitor are used only for testing purposes and also used to characterise the electronic noise generated by the detector-preamplifier system. The spectrometer used in this work is explained in this section along with the necessary calibration checks.
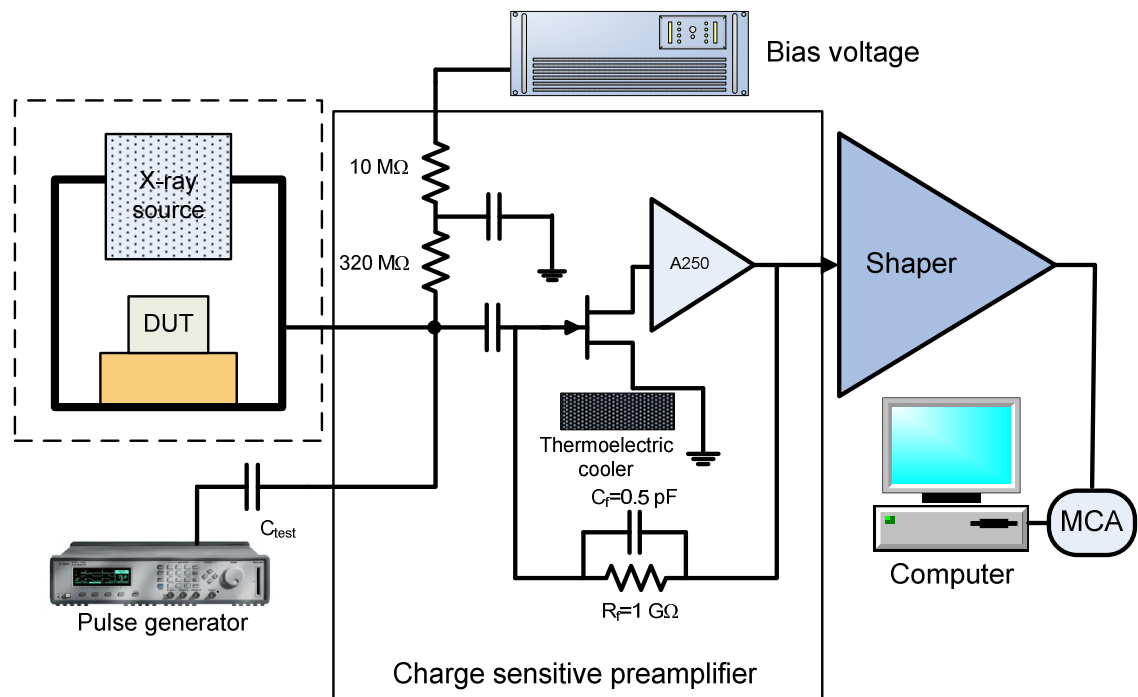
Figure 3.3 Schematic of a simple X-ray spectrometer.

3.4.1 Radioactive sources

The APDs investigated in the thesis are primarily for soft X-ray detection. A [55]Fe radioactive X-ray source from HTSL is used for most of the measurements [3]. The [55]Fe is encapsulated in a welded Monel capsule with a beryllium window. The source was covered in an additional cylindrical Perspex sleeve for handling purposes. The [55]Fe radioisotope has a half life of 2.73 years. The energy of photons and their probability of emission are shown in Table 3.1.

Additionally a [241]Am gamma-ray source has been used for higher energy detection. The [241]Am source is preferred for energy efficiency calibration for low energy detectors. [241]Am is a point source with an activity of 406 kBq. It is in a small plastic tile 10mm wide, 23mm long and 2mm thick with source (1mm diameter) located centrally. The decay process of [241]Am is rather complex, it alpha decays to [237]Np with majority of the decay populating the 59.5 keV gamma ray level. The gamma decays are also accompanied by Neptunium L-X-rays of high intensity in the 11 -23 keV range. The source has a half life of 432 years. Principal emissions of the source are also listed in Table 3.1.

Radiation source		Emission probability	Energy (keV)
[55]Fe	Mn - K_α	0.245	5.9
	Mn - K_β	0.0338	6.49
[241]Am	$XL_{\alpha 1}$	0.13	13.95
	$XL_{\beta 1}$	0.185	17.75
	$XL_{\gamma 1}$	0.029	20.78
	γ_1	0.0231	26.3
	γ_2	0.3592	59.5

Table 3.1: Emission data for [55]Fe [4] and [241]Am (for X-ray [5] and gamma-ray [6]) radiation sources.

3.4.2 Preamplifier

The signal from the detector is fed to a charge sensitive amplifier with a JFET at the input, where the input charge Q collected by the detector is deposited on the feedback capacitor, C_f, of the amplifier which produces a voltage step of magnitude Q/C_f. Hence the voltage step at the output is proportional to the charge deposited at the input.

The preamplifier used here is an Amptek A250 CoolFET charge sensitive preamplifier shown in figure 3.4 [7], where the input JFET is cooled to -50°C using a two stage Peltier cooler. Cooling the JFET reduces the shot noise generated by the JFET gate leakage current and also increases its transconductance which helps reduce the electronic noise in the preamplifier.
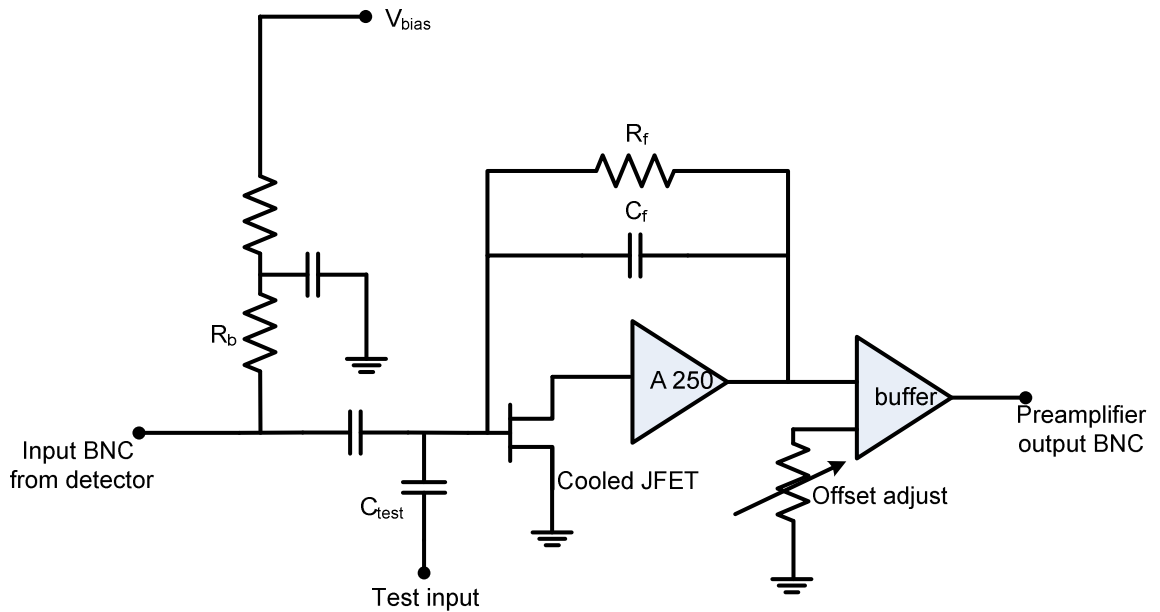
Figure 3.4 Block diagram of an Amptek A250 CF charge sensitive preamplifier.

In order to limit the series white noise of the preamplifier, the input capacitance should be comparable to the JFET input capacitance. Two choices of capacitances are available (using JFET 1 and 2 with C_{GS} = 8pF and JFET3 has C = 30pF) for high and low capacitance detectors. The JFET with C = 8pF is chosen for these measurements as most of the APDs used in the work

have capacitances below 25 pF. The preamplifier input is AC coupled. The detector is biased through a biasing resistor $R_b = 330$ MΩ and a high voltage low pass filter in preamplifier using a Keithley 2400 SMU.

The amplifier decay time of 500 μs is limited by the value of resistor $R_f = 1$ GΩ. The resistor is used to discharge the feedback capacitor and also establish a DC operating point to the amplifier. The feedback resistor will add to the thermal noise of the detector and its choice depends upon the shot noise from the leakage current of the detector and the input JFET. For low levels of leakage current a large resistor is necessary.

For calibration and noise measurements the detector output signal was simulated by a rectangular pulse generator coupled to a small 0.5 pF test capacitor. An Agilent 81101-a precision pulse generator was used to generate a square pulse with a rise time of 10 ns and a period of 100 μs. Charge is only transferred during the transition time of the pulse and is simply given as $Q = C_{test}V$, where Q is the charge transferred and V is the amplitude of the test pulse. The noise measurement is performed with the post amplifier and detector connected accounting for the total system noise.

3.4.3 Post amplifier

The preamplifier output is shaped using a pulse shaper. As described in chapter 2, pulse shaping techniques help improve the resolution of the spectrometer by improving the signal to noise ratio. The width of the output pulse from the preamplifier is reduced which makes it suitable for higher count rate applications without pile-up. An Ortec 570 shaping amplifier is used for the purpose [8]. The output of the shaping amplifier is a unipolar semi Gaussian pulse. The semi Gaussian shape is achieved by using a differentiator in cascade with an active integrator circuit, as shown in figure 3.5. The shaping time constant can be varied to obtain the best resolution from the detector. The choice of shaping time depends on the parallel and series white noise

contribution from the detection system. The shaped signal is also suitable for pulse height analysis using an MCA.
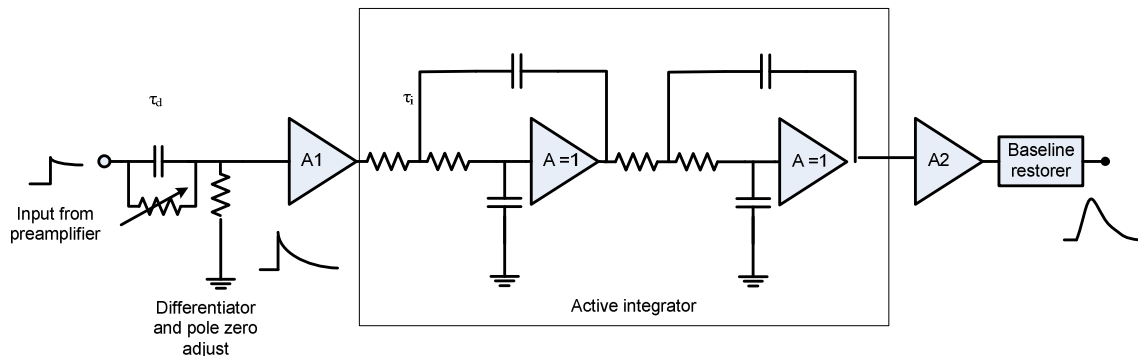

Figure 3.5 Schematic of the pulse shaping amplifier with a single stage differentiator followed by an active integrator in cascade, to produce a quasi Gaussian pulse shape.

The amplifier consists of an active filter shaping network that optimises the signal to noise ratio and reduces the pulse width. The differentiator in the shaping network produces an undershoot due to the exponential tail in the preamplifier output step signal. Pole-Zero (P-Z) cancellation technique is used whereby the pole created by amplifier pulse decay is cancelled by the zero of the shaping network. This is particularly important for higher count rate spectroscopy applications.

The test input can be used to configure the shaper output. The different gain and shaping time constant are adjusted from the front panel dials placed on the amplifier. Each time either the gain or the shaping time is adjusted the pole-zero correction of the amplifier needs to be checked and adjusted. This step is particularly crucial for fast count rate applications.
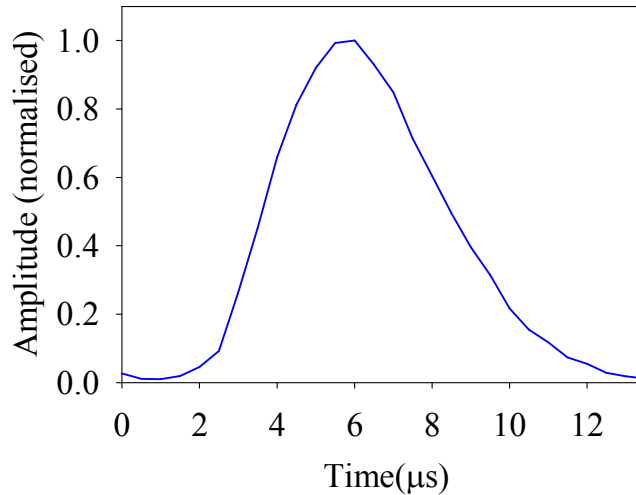
Figure 3.6 Semi Gaussian output from shaper with shaping time of 2μs using a test pulse.

Figure 3.6 shows the output for a shaping time constant of 2 μs normalised to its peak amplitude. The FWHM is 4.7×10^{-6}s, which is approximately equal to 2.36 times the shaping time of the amplifier.

The signal generated by the preamplifier using a pulse generator to simulate the detector can be used for P-Z adjustment. When connected to the shaper this produces unipolar semi Gaussian pulses of both positive and negative pulse captured using a Lecroy Waverunner oscilloscope shown in figure 3.7. The shaping amplifier can be adjusted for P-Z by using a screw potentiometer provided on the front panel until no undershoot is obtained. The figure shows the unipolar Gaussian pulse (with 2μs shaping time) for each transition of the square wave signal with P-Z adjusted.

For high count rate applications where pulses created by absorption of radiation are in quick succession, the P-Z cancellation becomes crucial. If a pulse arrives at the post amplifier when the previous pulse has an undercompensated P-Z adjustment, the negative undershoot can reduce the actual pulse height measured by the MCA, causing deterioration in the measured energy resolution of the radiation peak. Similarly overcompensation

can also limit the energy resolution. The P-Z cancellation effects are much less significant at lower count rates.
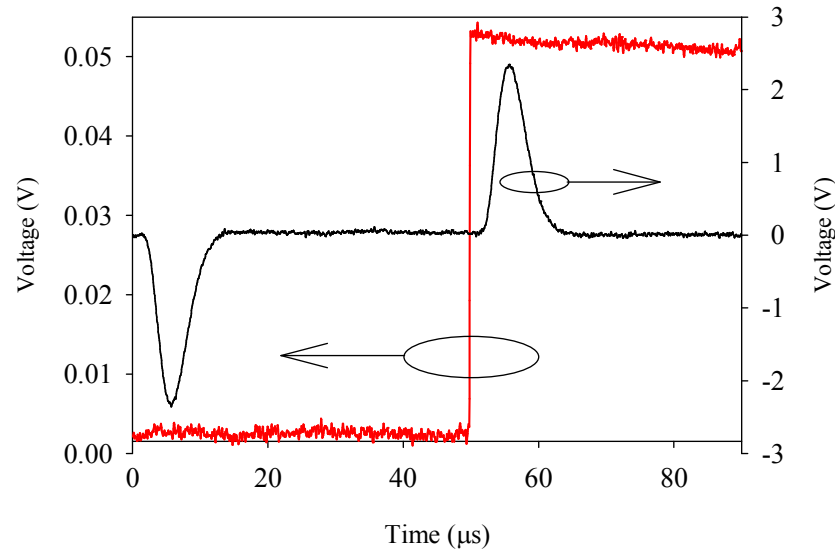
Figure 3.7 Output of preamplifier (red) and shaping amplifier (black) with a square wave input test signal.

3.4.4 Multichannel analyser

The shaped signal can now be used for pulse height analysis; the shaper output is connected to an Ortec easy MCA that is interfaced to a PC which is operated with Ortec's proprietary MAESTRO software package [9]. The semi Gaussian pulse height is sampled and converted to a digital value with an inbuilt ADC (Analog to Digital Converter) and binned into channels to build a histogram of the pulse height. The Ortec Easy MCA has a maximum of 8192 channels. The numbers of channels are selected depending on the required resolution of the spectrum being collected. A simple expression that gives the channel requirements for a detector is shown below

$$R = \frac{FWHM}{H} \quad ,$$
(3.6)

where R is the required resolution of the detector, FWHM is the full width at half maximum of the peak and H is the mean peak pulse height. In general the FWHM is required to be represented by at least 5 channels [10].
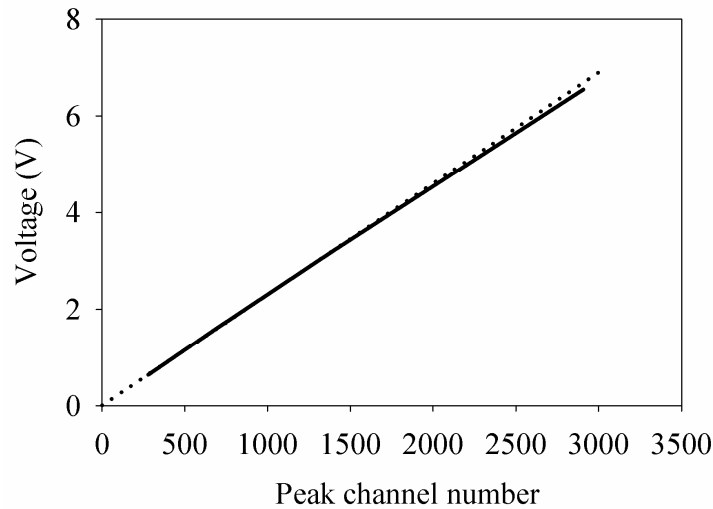

Figure 3.8 MCA linearity obtained using an electronic test pulse.

The BUSY signal from the shaper was used for dead time correction by connecting it to the BUSY input of the MCA. The pulser signal that was previously used as an input to the preamplifier produces a single peak in the collected spectra. The peak shifts to higher level in the MCA channel when its amplitude is increased. The FWHM at that peak can be directly obtained from the spectrum. An MCA calibrated with known energy sources will also give the FWHM in keV.

Ideally, a MCA should have linear conversion of pulse height to channel number. The linearity of the MCA is tested by recording the channel numbers with pulses of different known heights. The peak channel number is then plotted against the pulse height as shown in figure 3.8. The linearity is then given as the maximum deviation of the measured curve from a best straight line fit for the data. This data includes the uncertainties from the pulse generator and the preamplifier and hence represents the total system linearity. In order to test the pulse height to energy relation, a calibrated energy source is needed. The relation will also include the non linearity introduced by the detector used.
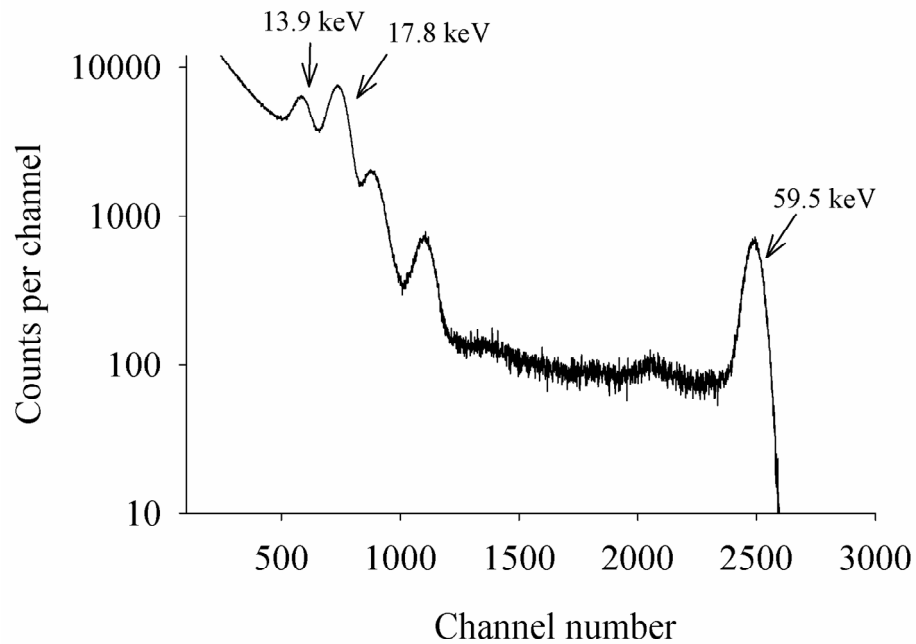
Figure 3.9 ^{241}Am spectra collected from a BPX65 diode.

The system was used to measure spectra from ^{241}Am gamma-ray source. A commercially available Centronic BPX65 Silicon photodiode was used as the detector. The device has low dark current in the pA range. The source was placed directly above the detector with its active area facing the top surface of the diode. The collected pulse height spectrum is shown in figure 3.9. The MCA can be calibrated by the two adjacent known energy doublet peaks of 13.9 and 17.8 keV respectively. In order to determine the energy resolution, the peak which corresponds to the energy at which maximum numbers of photons are emitted by the source (59.5 keV) was considered. Approximately 35% of the photons emitted by the source are of this energy. A FWHM of 1.89 keV was obtained at a reverse bias of 15 V corresponding to an energy resolution of $E_R =$ 3.1%.

3.5 References

[1]   S. M. Sze, *Physics of semiconductor devices*, 2nd Ed., ed.: John Wiley and Sons, Inc., 1981.

[2]   M. H. Woods, W. C. Johnson, and M. A. Lampert, "Use of a Schottky barrier to measure impact ionisation coefficients in semiconductors," *Solid-State Electronics,* vol. 16, pp. 381-394, 1973.

[3]   U. K. HTSL, "http://www.hightechsource.co.uk/Resources/Iron-55.pdf."

[4]   U. Schötzig, "Half-life and X-ray emission probabilities of 55Fe," *Applied Radiation and Isotopes,* vol. 53, pp. 469-472, 2000.

[5]   M. C. Lépy, J. Plagnard, and L. Ferreux, "Measurement of 241Am L X-ray emission probabilities," *Applied Radiation and Isotopes,* vol. 66, pp. 715-721, 2008.

[6]   V. P. Chechev and N. K. Kuzmenko, "Decay data evaluation project (DDEP): Updated evaluations of the 233Th and 241Am decay characteristics," *Applied Radiation and Isotopes,* vol. 68, pp. 1578-1582.

[7]   *AMPTEK Inc.*: 6 DeAngelo Drive, Bedford, MA 01730, USA.

[8]   *EG&G Ortec, Model 570 Spectroscopy Amplifier* Oak Ridge, Tennessee, USA.

[9]   *Ortec Easy-MCA-8k Digital Gamma-Ray Spectrometer* Oak Ridge, TN.

[10]   G. F. Knoll, *Radiation detection and measurement,* 3rd ed.: John Wiley & Sons, Inc.

Chapter 4 Avalanche gain and energy resolution of APDs

4.1 Introduction

Using compound semiconductors for X-ray detection offers more flexibility in detector design than using elementary Si and Ge. A wide band gap material offers better room and high temperature operations in hostile conditions with good spectral response while small band gap materials can offer higher spectral resolution provided the noise in the system is kept to a minimum. Compound (III-V) semiconductors have been used for detection of soft X-rays, while APDs have the added benefit of enhancing the signal to noise ratio of a detection system through avalanche gain. However, since avalanche multiplication is a stochastic process it can degrade the energy resolution of X-ray detectors. This depends on a number of factors such as the APD structure and constituent material parameters along with the incident photon energy. Despite the potentials in compound semiconductor APD detectors, there has been limited work on gain optimisation strategies in these detectors.

Conventionally the experimental energy resolution of semiconductor X-ray APDs has been interpreted using a semi empirical expression as follows [1, 2],

$$(FWHM_{total})^2 = (2.36\varepsilon)^2(f + F - 1)E/\varepsilon + (FWHM_{EN})^2 \quad , (4.1)$$

where $FWHM_{EN}$ accounts for the electronic noise arising from the amplifier and noise from the APD dark current and capacitance.

The first term on the right hand side of equation 4.1 includes the statistical errors from two fundamental sources. The first is the fano factor, f, which relates N, the number of primary EHPs, to the variance of primary EHPs,

$$\sigma_{ehp}{}^2 = Nf. \tag{4.2}$$

The second mechanism captures the effect of gain distribution of APD if the absorbed photons obey Poissonian statistics (this is generally acceptable for visible photon absorption but less obvious for X-ray photon absorption that leads to a large N). In conventional APDs where the avalanche process is seeded by a single EHP, the variance is

$$\sigma_{APD}{}^2 = <g^2> - M^2 = (F\text{-}1) \; M^2, \tag{4.3}$$

where F is the excess noise factor that characterises the gain fluctuation and g is the gain associated with each individual absorbed photon, Since an injected EHP does not always produce the same gain under a given set of conditions and can be approximated using [3]. Note that equation 4.3 is true for pure electron (or pure hole) injection case which can be easily achieved in conventional APD but much less likely in X-ray APD due to the significantly larger mean free path length of incident photons (this will be revisited in section 4.3.2). However to obtain an approximate analytical expression the following assumptions are made in equation 4.1 (i) equation 4.3 is assumed to be applicable and (ii) the carrier injection into the avalanche region is pure such that a single value of F is applicable. Since the two mechanisms are independent of each other, using the error propagation formula the final variance scaled by M^2, is given by

$$\sigma^2 = \frac{1}{M^2}\left(M^2\sigma^2{}_{ehp} + N\sigma^2{}_{APD}\right). \tag{4.4}$$

Using (4.2) and (4.3), and $N = E/\varepsilon$ we have

$$\sigma^2 = \frac{E}{\varepsilon}(f + F - 1). \tag{4.5}$$

Assuming a Gaussian distribution for the output signal, its FWHM is given by $2\sqrt{(2\ln2)}\sigma \sim 2.36\sigma$. Using (4.5), the FWHM expressed in energy is

$$FWHM = 2.36\varepsilon\sqrt{\frac{E}{\varepsilon}(f + F - 1)}\,.$$ (4.6)

Although 4.1 can be used for quantitative analysis of the APDs energy resolution, it has not been shown whether F can explain the avalanche gain distribution accurately for X-ray APDs. Recently Barnett *et al.* [4] analysed the energy resolution data of an AlGaAs soft X-ray APD from [5] by including avalanche multiplication from the p^+ and i-layers in the APDs. This model predicts the bimodal distribution in the energy spectra but was unable to include accurate distribution of the avalanche gain.

In this chapter a detailed analyses of the avalanche gain distribution of semiconductor X-ray APDs is presented. The effect of the incident photon energy, material EHP creation energy, ionisation coefficient ratio and the mean gain among others were studied using simulations. Analytical equations have been previously derived by McIntyre to access the relationship of avalanche gain and the number of injected EHPs [6]. These equations do not include the non local effects that can affect avalanche gain statistics. The model presented in this work includes the carrier dead space. Since X-ray absorbed across the device leads to a mixed injection of carriers across the avalanche region the dependence on the EHP creation position is also accounted for. The model can be used to predict the realistic gain distribution profile of the APD, This allows for the accurate prediction of the energy resolution broadening caused by the randomness of the avalanche process.

4.2 Model

A brief summary of previous work in determining the avalanche gain distribution of APDs is presented. The probability density functions of the gain in an avalanche region with uniform electric field have been previously presented by McIntyre [6]. Following [6] we have for a depletion region of width, w and pure electrons injected at position $x = 0$ into the avalanche region, the

probability $P_{n,n+r}$ that r ionisation events taken place in the avalanche region at position $x_1, x_2, \ldots x_r$ generating $n + r$ electrons at the output is given as

$$P_{n,n+r} = \int_0^w dx_1 \int_{x_1}^w dx_2 \ldots \int_{x_{r-1}}^w dx_r \, p_{n,n+r}(x_1, x_2, \ldots x_r) \quad , (4.7)$$

where $p_{n,n+r}$ is given by the product of the probability density that ionisations occur at $x_1, x_2, \ldots x_r$, $p_1(n,r)$ and the probability that no ionisations occur elsewhere, $P_2(n,r)$. The model is difficult to solve analytically hence an assumption of $k = \beta/a$ is made such that k is independent of the electric field The approximation of the probability distribution function is given as [6]

$$P_{n,n+r} = \frac{n}{\sqrt{(2\pi(n+r)(n+kr)r)}} \left(1 - \frac{nX}{r}\right)^r \left(1 + \frac{n(1-k)X}{n+kr}\right)^{(n+kr)/(1-k)}$$

$$, (4.8)$$

where $X = (n+r-nM)/nM = a - 1$, where $a = n+r/nM$ is the ratio of the actual gain to the mean gain, M. The equation above has been used to model the experimentally obtained values for a Si reach through APD [7]. An effective value of $k = 0.028$ was shown to provide a good fit with the experimental data for a range of multiplication values, with k being the only adjustable parameter.

Other models has been developed to provide an alternative to McIntyre's models [8-11] which were primarily developed to study the bit error rate performance of APDs used in optical telecommunications systems. Moment generating functions of the avalanche gain were obtained for the case of equal ionisation coefficients and the case of single carrier ionisation [10]. A generalised moment generating function of the gain as a function of k and M has also been derived [11]. Since no analytical solution was available the functions had to be solved numerically. This approach was shown to corroborate with the study by McIntyre.

All the above models assume a constant ionisation probability along the avalanche region such that the ionisation probability is independent of the carrier history. From a realistic standpoint, every single carrier generated needs to travel a certain distance before it can gain sufficient energy to initiate an ionisation event. This is defined by the carrier 'dead-space' and is dependent on the strength of the electric field and the threshold energy for impact ionisation. Significant dead-space is shown to reduce the avalanche multiplication and excess noise factors in a range of semiconductor materials [12-15]. The good agreement with McIntyre's model [6] with experimental results by Conradi [7] is obtained due to the thick avalanche region Si APD used in the measurements negating effects of dead space. Current APDs have depletion regions that are significantly smaller which make the dead space an important factor.

Another limiting factor of the model in [6] is that it does not take into account the carrier velocity. This is plausible if the bandwidth of the APD is significantly larger than the rate of the incoming signal. X-ray detectors with good timing resolution are necessary for high count rate applications, where the speed of the APD can be a limiting factor. Additionally, the probability distribution functions have been accurately predicted using the above expressions for pure injection of carriers into the avalanche region. X-rays are of considerably higher energy and hence are absorbed throughout the active region of the diode resulting in mixed injection carriers into the avalanche region. Hence in practical X-ray APDs a more complete model that takes into account the mixed injection of carriers is needed.

Hayat *et al.* have incorporated dead space effects and finite carrier velocity to access the bit error rate performance of the APD using recursive equations [16]. In these analyses, the probability density function (PDF) of the injected charge was assumed to be Gaussian. Another sampling technique to approximate the PDF of the charge is shown [17]. For energy resolving X-rays a model that takes into account the ionisation dead-space and distributed generation of charge all across the avalanche region is needed to generate realistic gain distribution of X-ray APDs. Monte Carlo models from full band

[18] to simple [19, 20] have been used to study the avalanche properties of semiconductors. A Random Path Length (RPL) model that has been developed to accurately model M and F in a wide range of semiconductor materials is chosen for this purpose [21-24].The RPL model was chosen as it can incorporate dead space and carrier velocity effects without the analytical difficulties associated with the integral technique [17], Initial results that exclude dead space are compared with those obtained from equation 4.8 to determine its validity.

In the RPL model, the random ionisation path length of an electron, x_e, is described by the ionisation path length probability density function, $h_e(x_e)$. In the simulations, x_e is determined by substituting uniformly distributed random number R between 0 and 1 into the survival probability, $S_e(x_e)$, which is given by

$$R = S_e(x_e) = 1 - \int_{0}^{x_e} h_e(x_e)dx .$$

(4.9)

In conventional APD simulations to obtain M and F, an EHP is injected at a position, ζ within an avalanche region width of w. The avalanche process is initiated by choosing a random path length x_e (for $w \geq \zeta + x_e$) and under the assumption that the electron travel from left to right of the avalanche region. An electron hole pair is created at position ($\zeta + x_e$), along with the initial primary electron. The process is repeated for all primary and secondary electrons until they exit the avalanche region. By replacing x_e and $S_e(x_e)$ by x_h and, $S_h(x_h)$, a similar approach is applied for all the holes (travelling from right to left) until their exit at $\zeta = 0$.

In each simulation trial, an X-ray photon interaction with the detector will generate a large number of EHPs depending on the photon energy and ε of the absorber material. Assuming that all the EHPs are created within a small distance of the position of interaction, appropriate numbers of EHPs are injected at the photon absorption position. The model tracks each carrier's journey through the avalanche region until its exit. The avalanche gain of each

trial, g, is then given by the ratio of the total number of final EHPs to the number of injected EHPs. At least 10000 trials were simulated for a given set of conditions to give gain distribution functions, $P(g)$, which are statistically accurate. Full width at half maximum of the gain distribution function, $FWHM_g$, can be obtained from $P(g)$ that indicates the detector energy resolution. Mean gain, M, is also obtained from $P(g)$.

4.3 Results

The following sections present an intensive analysis of the dependence of the gain distribution on the incident energy its path length through the absorbing material and the ionising properties of the constituent material.

4.3.1 Dependence on material parameters and incident photon energy

To analyse the dependence of the gain distribution on the material electron hole pair creation energy and the interacting photon energy, probability distribution functions of the gain, $P(g)$, for a mean gain, $M = 10$, simulated by injecting different number of EHPs at $\zeta = 0$ and assuming $k = 1$, are compared in Figure. 4.1. $P(g)$ changes from a quasi-exponential distribution for injection with a single carrier to a Gaussian like distribution for injections with large numbers of EHPs (> 1000). For a single injected carrier a large spread in the gain is obtained. Since a large number of these electrons injected fail to impact ionise while a certain number of electrons ionise readily to produce multiplication values well above a factor of 10.

While the equation given in (2.23) successfully models the excess noise for the single carrier injection it is insufficient for carriers generated by X-ray absorption since the absorption of X-ray creates a large number of EHPs that lead to different distribution of $P(g)$. $P(g)$ is also strongly dependent on the position of interaction of individual X-ray photons which requires the

consideration of the carrier generation profile across the active region of the detector to be considered to determine the real distribution.
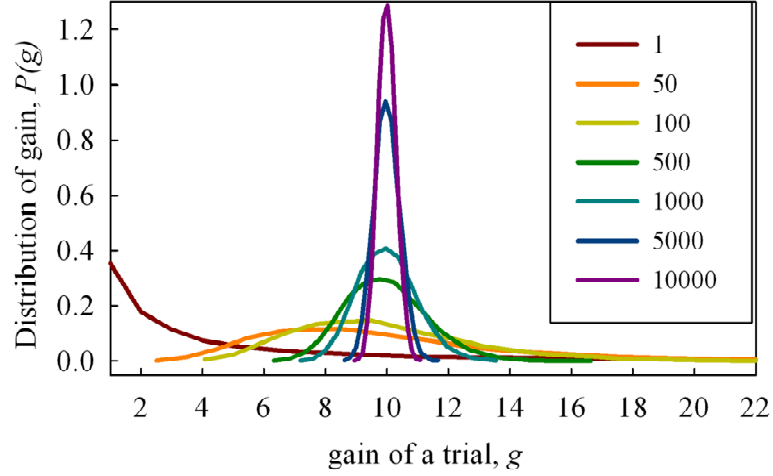

Figure 4.1 Simulated gain distributions for different numbers of EHPs (1 to 10000) injected at position $\zeta = 0$ assuming $k = 1$. Each simulation yields a mean gain of 10. The pseudo exponential distribution for a single carrier rapidly converges to a Gaussian as higher numbers of EHPs are injected.

The results for pure injection of carriers are verified using McIntyre's model as shown in figure 4.2. $P(g)$ is simulated for different k values. The solid curves are directly obtained from equation 4.8. Good agreement between the two is seen for the computed values.

The excess noise factor F, conventionally given by $<g^2>/<g>^2$ is concurrently computed for increasing EHPs and is seen to rapidly approach unity as shown in Figure 4.3(a). Similarly, with the increasing number of EHPs injected the FWHM of $P(g)$, FWHM_g, reduces as shown in Figure 4.3(b). Since a large number of primary carriers are injected the non- ionising carriers are easily compensated by carrier that ionise repeatedly to create large multiplication chains, leading to a much more deterministic ionisation process and a smaller FWHM_g. $P(g)$ is hence expected to converge to a delta-like function for very large number of EHPs. Hence using conventionally obtained excess noise factors to determine the spread in the energy resolution due to

avalanche noise is incorrect and can lead to overestimation of the degradation of the energy resolution due to avalanche statistics.
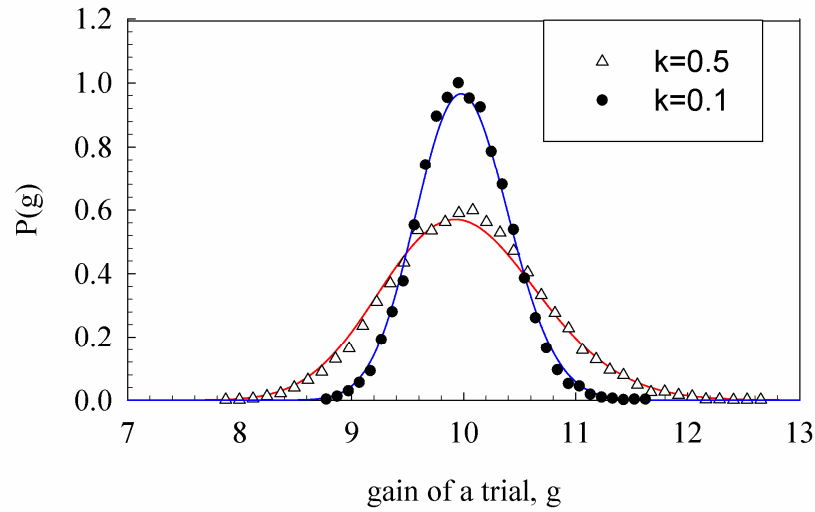

Figure 4.2 Comparison of $P(g)$ obtained from McIntyre's equation 4.8 (solid) with those generated from the RPL model (symbols) for $n=1000$, $M=10$.
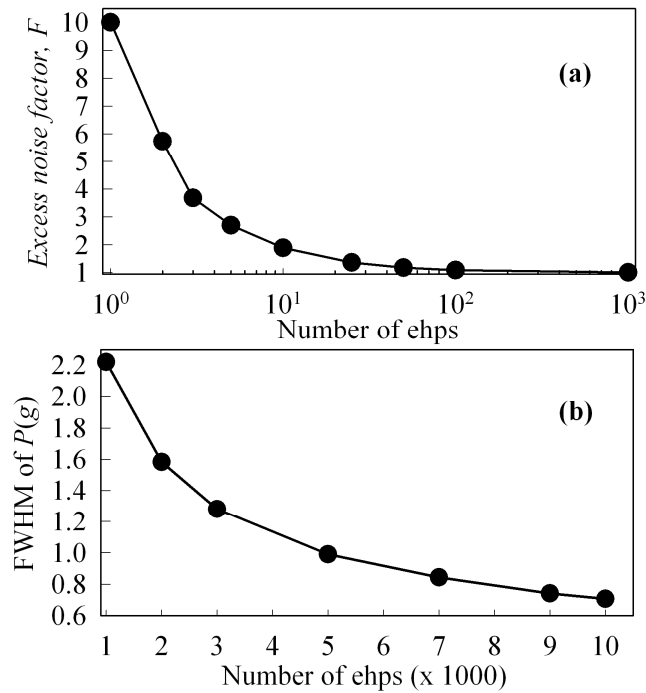

Figure 4.3 Variability of the (a)the excess noise factor and (b) FWHM$_g$ of $P(g)$ with the number of EHPs injected at position $\zeta = 0$. The value $k = 1$ and $M = 10$ are used in the simulations.

For interactions with high energy X-ray photons the number of EHPs produced is large, suggesting that the avalanche gain can improve the energy resolution and overall signal to noise ratio of the X-ray APDs. For low energy X-rays, chosen with a small ε will give large number of EHPs which is desirable to achieve a narrow $P(g)$.
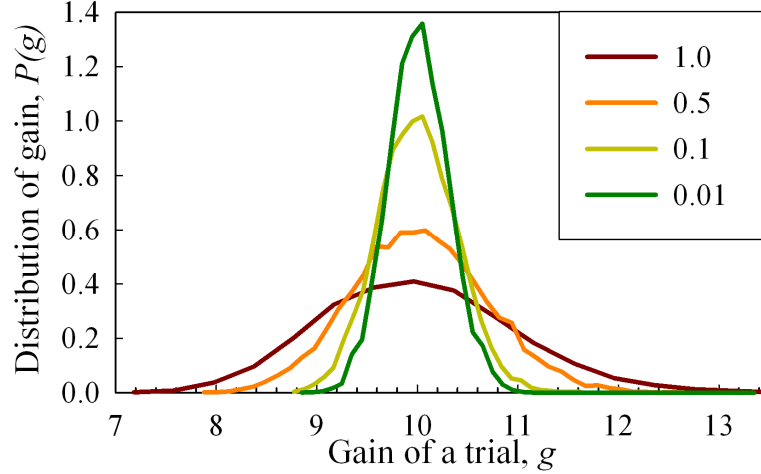

Figure 4.4 Simulated $P(g)$ for $M = 10$ with 1000 injected EHPs and different values of $k = 0.01$, 0.1, 0.5 and 1.0.

A further analysis was undertaken to assess the influence of ratio of ionisation coefficients. The dependence of $P(g)$ on k, using simulations with 1000 EHPs injected at $\zeta = 0$ and $M = 10$ was assessed. The results are compared in Figure. 4.4. Identical ionisation coefficients for electrons and holes, i.e. $k = 1$, produces the broadest $P(g)$. As electron and hole ionisation coefficients, become increasingly dissimilar i.e. k approaching 0, $P(g)$ narrows rapidly. More interestingly an analysis of the number of EHPs required to achieve a given $FWHM_g$, ~0.7 used in this case, shows that the minimum number of injected EHPs required increases with M and k. Simulations were carried out for different values of M (5 to 20) and k (0.01, 0.1, 0.5, and 1.0) and are shown in Figure 4.5. Hence to achieve a given $FWHM_g$ at low photon energies (small number of EHPs), in addition to the requirement for a material with a small ε, a material with a low k is preferred. Similarly for higher values of M, there are more statistical fluctuations in the ionisation of the injected EHPs, requiring more injected EHPs to reach $FWHM_g \sim 0.7$.
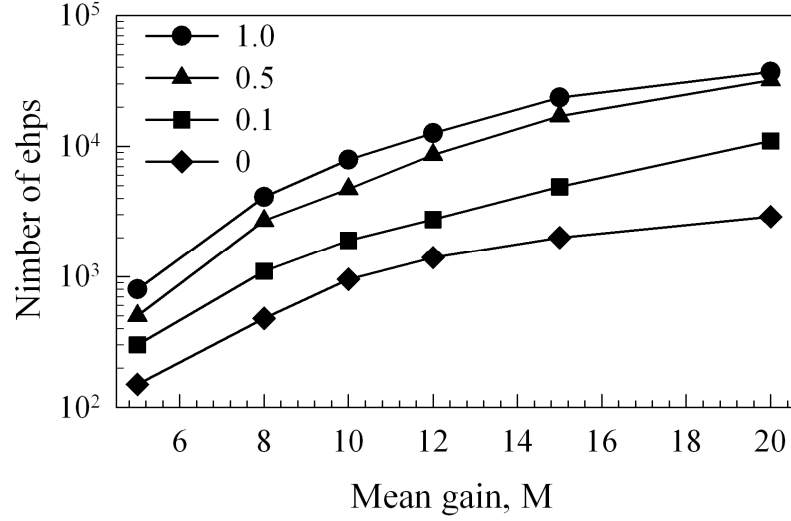
Figure 4.5 Minimum number of EHPs required to achieve a distribution of $P(g)$ with linewidth (FWHM~0.7), as a function of k, for M in the range from 5 to *20.*

Although avalanche gain will always add to the spread in energy resolution, it can also help to significantly improve the signal to noise ratio of the detection system. The model can be used to determine the maximum value of M for an X-ray APD at a given $FWHM_g$ to ensure the highest signal amplification without degrading the energy resolution, through the number of EHPs generated by the X-ray photon. The choice of operating gain will ultimately depend on the electronic noise from the leakage current of the APD and read out electronics. In the example presented in Figure 4.5 where the X-ray photon generated 1000 EHPs per interaction before the avalanche region such that carriers are injected at $\zeta = 0$ in materials with $k = 0$, 0.1, 0.5 and 1, the maximum value of M to achieve $FWHM_g \sim 0.7$ would be 9.97, 7.66, 6.15 and 5.36, respectively. For a detection system where the series white noise is larger than the noise contribution from the leakage current flowing through the detector, a material with a small k value can be operated at higher M without degrading the energy resolution. Although materials with comparable electron and hole ionisation coefficients tend to show the highest deterioration in the energy resolution, they would still be acceptable for detection of higher energy X-ray photons due to

the larger number of primary EHPs available for impact ionisation. If the avalanche noise becomes comparable or larger than the noise originating from the electronics no improvement in the overall signal to noise ratio will be seen.

4.3.2 Dependence on carrier injection position

Since X-rays are of considerably higher energy their mean free path length through a semiconductor APD can be a significant portion of the active region thickness. Thus even in the soft X-ray range absorption can take place all along the avalanche region of the detector. The absorption profile has to be considered in order to assess the actual deterioration due to avalanche gain in practical applications. Simulations at different injection positions for $k = 1.0$ and $M = 10$ were carried out. The results of $P(g)$ with injection positions, $0 \leq \zeta \leq w$, are compared in Figure 4.6(a). In conventional APDs the mean gain is independent of injection position, a similar trend is seen in the simulated $P(g)$ which is invariable to the charge injection position. Hence for materials with $k = 1$, the statistical broadening of $P(g)$ only depends on the mean gain M and the number of EHPs injected, This allows for absorption of photons within the depletion region of the APD without a compromise on both the energy resolution and quantum efficiency. A simple p^+in^+ diode with a constant electric field profile in the i-region would thus be adequate for higher energy X-ray APDs.

To analyse the dependence on injection position for disparate ionisation coefficients, the simulations were repeated for $k = 0.5$. Figure 4.6(b) shows that the gain distribution is strongly dependent on the injection position. For such cases where the X-ray photons are strongly absorbed throughout the avalanche region, $P(g)$ with consequentially be a discrete sum of the individual $P(g)$ due to carriers generated at each photon interaction position ζ *where* $0 \leq \zeta \leq w$, resulting in a broad distribution of $P(g)$. Absorption of photons in the avalanche region is hence detrimental when $k \neq 1$ and needs to be minimised by design.
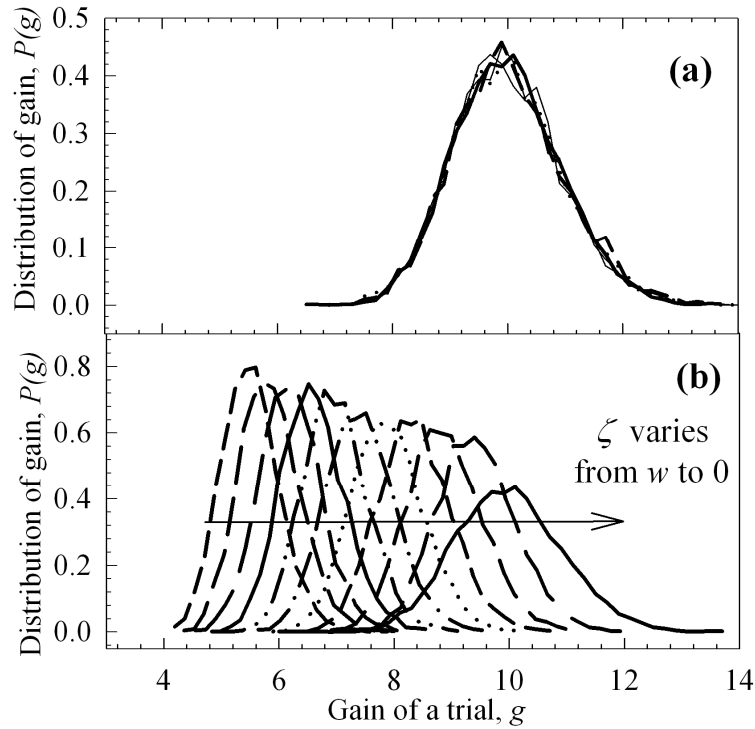
Figure 4.6 Simulated $P(g)$ for (a) $k = 1.0$ and (b) $k = 0.5$, when the injection position varies from $\zeta = w$ to 0, in steps of $0.1w$. $P(g)$ is invariable to injection position when $\alpha = \beta$.
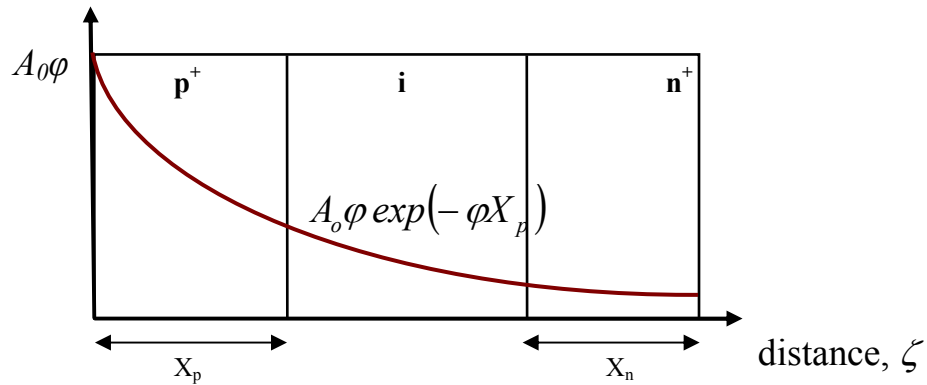
Figure 4.7 Schematic of a p^+in^+ diode illustrating its distributed carrier generation profile.

The position dependent distribution of $P(g)$ can be modelled and is illustrated for a simple p^+in^+ diode shown in Figure 4.7. Consider X-ray photons at a rate A_o photons per second and per unit area from the top p^+ surface of a p^+in^+ diode with p^+, i, n^+ region of widths X_p, w, and X_n, If φ is the absorption

coefficient of the diode then the rate at which EHPs are generated in the p$^+$ and n$^+$ region denoted as A_p and A_n respectively are given as

$$A_p = A_o\left(1 - exp\left(-\varphi X_p\right)\right)$$

(4.10)

$$A_n = A_o exp\left(-\varphi(X_p + w)\right)\left(1 - exp\left(-\varphi X_n\right)\right)$$

(4.11)

Accounting for the position dependent gain distribution, $P(g, \zeta)$, where ζ is calculated from the p$^+$/i region interface of the diode, the cumulative gain distribution of the diode is given by,

$$P(g) = A_p P(g, 0) + \int_0^w P(g,\zeta) A_o \varphi exp(-\varphi X_p) exp(-\varphi\zeta) d\zeta + A_n P(g, w)$$

, (4.12)

The above equation can be now used to determine the gain distribution of diode with different attenuation coefficients and active layer thickness (with $0 > \zeta < w$). To exemplify the dependence on these factors and ultimately the photon interaction position, $P(g)$ is simulated for different values of $\varphi X_p = 0.1$, 0.5 and 1.0, assuming that $w = 2X_p = X_n$ and $k = 0.5$. The results that have been simulated to achieve a pure electron injection mean gain of 10 are compared in Figure 4.8.

When φX_p is large, most of the photons are absorbed in the p$^+$ region resulting in the pure injection of electrons into the avalanche region. The cumulative gain distribution is thus largely dependent on the first term, $A_p P(g)$ in equation 4.12, resulting in a peak gain of 10. Photons absorbed in the n$^+$ and i region of the diode will also broaden the cumulative distribution. The peak at a gain of 5.5 in figure 4.8 is largely due to the ionisation events initiated by holes generated in the n$^+$ region of the diodes. When all the photon are absorbed in the p$^+$ region of the diode, no secondary peaks occur and $P(g)$ of the profile shown in figure 4.8 (solid curve) is obtained.
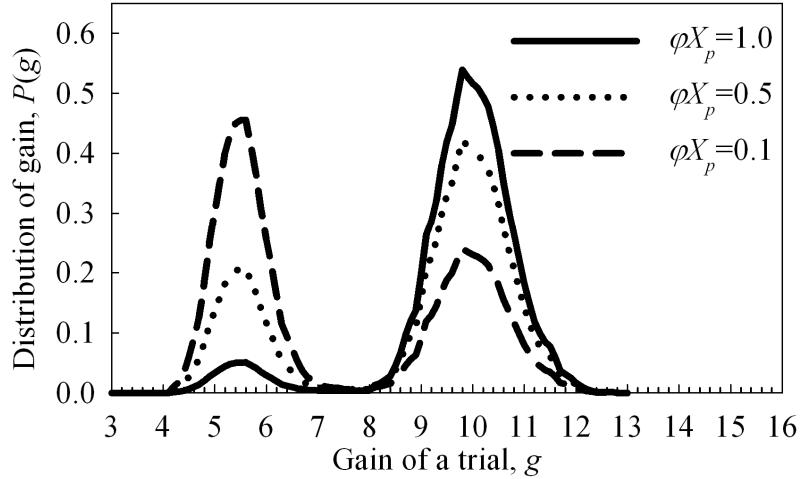
Figure 4.8 $P(g)$ due to distributed photon absorption in a p^+in^+ diode calculated using (equation 4.12), the ratios of photon absorption coefficient and epilayer thickness are shown in the legend.

Conversely when φX_p is small, photons are weakly absorbed throughout the p^+, i and n^+ regions, resulting in a broad distribution (computed in figure 4.8 (dashed curve) for $\varphi X_p = 0.1$). The larger peak at 5.5 and a second smaller peak at 10 obtained are consistent with the experimental results presented in [5] where an APD with a similar absorption profile was used to detect 5.9 keV X-rays. The model is compared with experimental data obtained from a GaAs/Al$_{0.8}$Ga$_{0.2}$As APD in chapter 6. The peaks at $g = 10$ and $g = 5.5$ are determined by $A_pP(g,0)$ and $A_nP(g,w)$ respectively. The intermediate gains between the two peaks and the overall distribution are determined by the integral of the middle term in equation 4.12.

When φX_p is small the dependence of the distribution on the middle term increases with the avalanche region width for materials with disparate ionisation coefficients. The reliance on the intrinsic region width is mitigated when φX_p increases. This effect is illustrated in figure 4.9 for the same case of $k = 0.5$ and a mean gain 10, for $\varphi Xp = 0.1$ and 0.5 each with $w = X_n$ and $4X_n$. The simulated curves in figure 4.9(b) show that increased absorption in the avalanche region can severely impede the peak resolving capability of the APD.
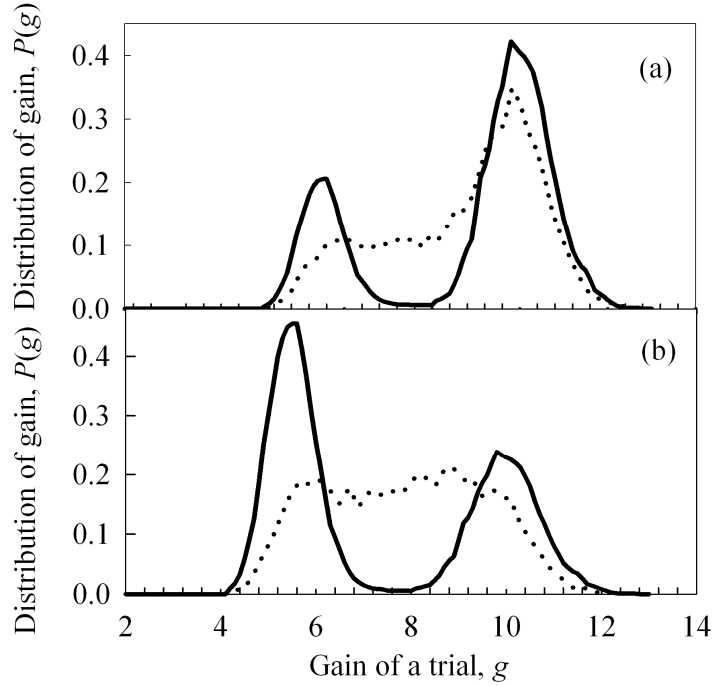
Figure 4.9 $P(g)$ due to distributed photon absorption in a p^+in^+ diode (a) φX_p = 0.5 (b) φX_p = 0.1 each with $w = X_n$ (solid) and $4X_n$.(dotted).

For $k \neq 1$, when most of the X-ray photons are absorbed before the avalanche region, the results strongly suggest that a minimum spread in the gain distribution occurs. This can be practically achieved by either having the photons absorbed in the p^+ region of the device (limited to by the minority electron diffusion length of the material) or within an absorption region with sufficiently low electric field to ensure unity gain, such as in a separate absorption and multiplication region APD, to achieve the best possible energy resolution.

4.3.3 Effects of 'dead space' on the avalanche gain distribution

The local model predicts an ionisation path length PDF of a carrier that exponentially decays from its point of creation. Although as discussed before each carrier has to traverse a dead space before it can gain sufficient energy to impact ionise. Significant dead space effects are known to reduce both the multiplication and excess noise factors in APDs with submicron (typically < 0.5 μm) avalanche regions [23, 24]. The local model is hence only valid when the

dead space is insignificant compared to the avalanche region width, w and the distance between consecutive ionisation events. Hence the gain distribution, $P(g)$, is also a function of the carrier ionisation dead space. Self contained models like the Monte Carlo techniques have been previously used to compute accurately the multiplication and excess noise in a range of APDs [18-20]. Recessive techniques and RPL model which are less cumbersome than the Monte Carlo models have also been successfully used to model the reduced multiplication and excess noise in APDs [16, 17]]. The RPL model described earlier in the chapter is used with a hard threshold for the dead space. The assumption of the hard threshold is reasonably plausible but care has to be taken when used this approach for avalanche region width < 0.1 μm, where the dead space can be a very large fraction of w. This section presents a study of potentially important effects of carrier's 'dead space' in impact ionisation on the energy resolution of X-ray APDs. The effects of dead space on mixed carrier injection and its subsequent effect on the gain distribution is also studied.

For an avalanche region with a uniform electric field profile, the hard threshold limited ionisation path length PDFs can be given as,

$$h_e(x_e) = \begin{cases} 0 & , x_e \leq d_e \\ \alpha * exp[- \alpha * (x_e - d_e)] & , x_e > d_e \end{cases} \tag{4.13}$$

and

$$h_h(x_h) = \begin{cases} 0 & , x_h \leq d_h \\ \beta * exp[- \beta * (x_h - d_h)] & , x_h > d_h \end{cases}, \tag{4.14}$$

where $\alpha*$ and $\beta*$ are the non-local ionisation coefficients for electrons and holes respectively. The hard threshold dead space d_e (d_h) for the electron (hole) can be calculated ballistically as

$$d_e = \frac{E_{the}}{\xi} \quad \text{and} \quad d_h = \frac{E_{thh}}{\xi} , \tag{4.15}$$

where E_{the} (E_{thh}) is the electron (hole) ionisation threshold energy. The local ionisation coefficient α and β for electron and hole respectively are related to non-local coefficients by the following relation,

$$\alpha = \frac{1}{d_e + \frac{1}{\alpha^*}} \quad \text{and} \quad \beta = \frac{1}{d_h + \frac{1}{\beta^*}} . \tag{4.16}$$

Random electron and hole ionisation path lengths are then computed and the multiplication and subsequently the PDFs are generated using the method described in section 4.2.

To study the effects of dead space on $P(g)$, simulations were carried out for $k \equiv \beta/\alpha = 0.1$ and 0.5 with 1000 EHPs injected per trial at $\zeta = 0$, covering mean gains of $M = 5$ to 20. Identical electron and hole dead spaces, d, were assumed for simplicity. Significance of dead space in the simulations was varied by using the ratio $d/w = 0$ and 0.3. The ionisation coefficients were appropriately adjusted to maintain the same M for cases with different d/w values. Figure 4.10 compares the FWHM_g given as a percentage of the mean gain for $k = 0.1$ and 0.5. The FWHM is computed as a percentage of the mean gain to ensure a fair comparison of the change in distribution at different mean gain values. For a given k value, FWHM_g reduces when dead space is increased. This is because significant dead space results in a more deterministic ionisation process which narrows $P(g)$. Conventional APDs used for light detection are known to exhibit lower than expected excess noise factors when dead space becomes more significant in these avalanche regions. For $d/w = 0.3$, $P(g)$ becomes narrower as k approaches zero (α and β become disparate), as shown by the smaller FWHM_g in figure 4.10. This trend with decreasing k is consistent with the observation made previously where no dead space was accounted for.
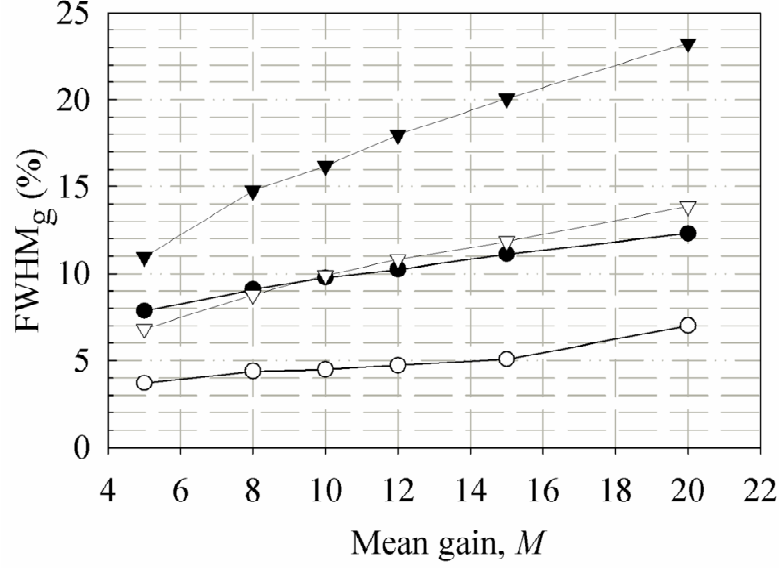
Figure 4.10 FWHM$_g$ as a percentage of mean gain for $k = 0.5(\triangledown)$ and $k = 0.1(\bigcirc)$, each with $d/w =0$ (closed symbols) and 0.3 (open symbols).

The decreasing FWHM$_g$ with increasing d/w ratio can be explained as follows. The randomness in the multiplication value obtained is largely determined by the variance of the ionisation path length of the electron. For the simulated range of d/w ratio from 0.1 to 0.3 the probability of the electron ionising has the highest value just after it has traversed its dead space and hence an electron hole pair is created (in addition to the original electron) thereafter. The secondary carriers also have a probability of ionising before their exit from the avalanche region. The impact ionisation process is strongly dependent on $h_e(x_e)$ of the primary electron. With increasing dead space the variance of ionisation path length PDF becomes smaller leading to a narrower PDF. Hence there is a significant reduction in the uncertainty of the ionisation of primary electrons. Due to the large number of primary electrons injected from an X-ray photon absorption event, the multiplication process is highly deterministic. This reduction in the fluctuation in the multiplication process leads to $P(g)$ with decreasing FWHM$_g$ at larger d/w values.
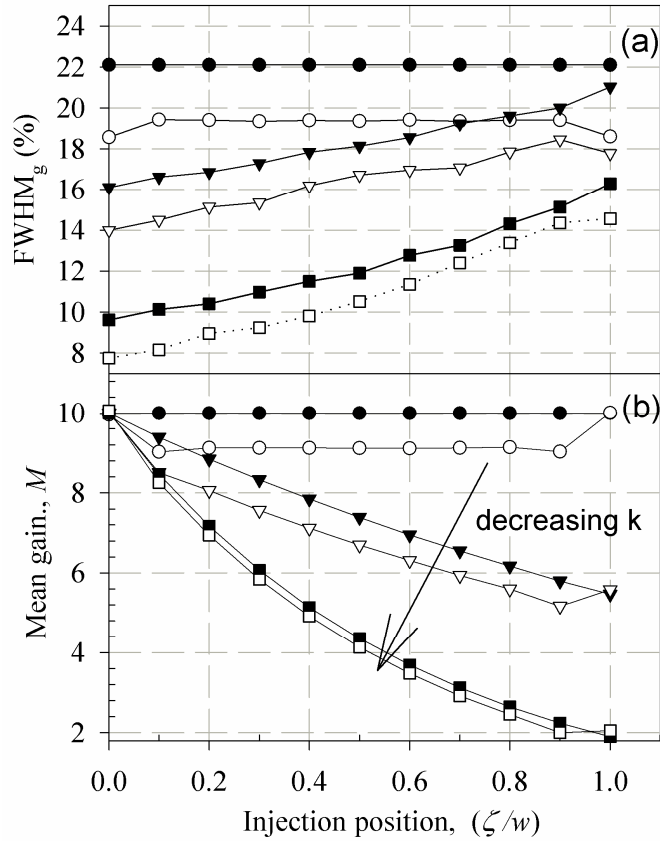
Figure 4.11 (a) FWHM$_g$ as a percentage of the mean gain across the avalanche region for $k = 1$ ($\bigcirc$), $k = 0.5$ ($\bigtriangledown$) and $k = 0.1$($\square$), each for $d/w = 0$ (closed symbols) and 0.1 (open symbols). (b) Simulated corresponding mean gain across the avalanche region.

So far we have considered the case where EHPs are injected at $\zeta = 0$, resulting in pure electron initiated impact ionisation. When $k \neq 1$, $P(g)$ varies with the charge injection position within the avalanche region. Since the effect of dead space is not known for the mixed injection condition, the gain distribution is simulated for 1000 EHPs, varying the injection position from $\zeta = 0$ to $\zeta = w$. The ionisation coefficients are appropriately adjusted such that all simulations conditions yield a multiplication factor, $M = 10$ at $\zeta = 0$. Figure 4.11(a) compares the simulated FWHM$_g$, expressed as a percentage of M versus injection position, for $k = 1$, 0.5 and 0.1 (with and without dead space effect). Equal electron and hole dead spaces given by the ratio $d/w = 0.1$ have been

assumed in these simulations. The corresponding mean gains are shown in figure 4.11(b).

From figure 4.11(a), it is clear that for a given set of k (for $k \neq 1$) and d/w, injection position of $\zeta = 0$ yields the smallest FWHM_g and largest M, as the simulations assumed that the electrons impact ionise more readily than holes i.e. $\alpha > \beta$. A similar approach can also be applied to the case where holes have a higher ionisation probability. As ζ varies from 0 to w, FWHM_g increases and M decreases. Although $k = 1$ gives constant gain independent of the injection position, which is desirable in minimising distribution in gain across the avalanche region, it gives the largest FWHM_g, in comparison to $k = 0.5$ and 0.1. When dead spaces in the avalanche regions are considered, FWHM_g improves for all k values, with $k = 1$ showing the largest reduction. Thus for $k = 1$, in avalanche regions with significant dead space, an improvement in FWHM can be achieved when pure electrons (or holes) are injected without a reduction in M. The effect of dead space on the reduction in M, for $k < 1$ is observed to be less significant as k approaches 0.

To analyse, the dependence of $M(\zeta)$ and $P(g, \zeta)$ with varying injection position , ζ, across the avalanche region we consider the simple case of $k = 1$. Figure 4.12 shows the FWHM_g of $P(g, \zeta)$ and $M(\zeta)$ with 1000 EHPs injected across the avalanche region with $d/w = 0.2$. For $k = 1$, the FWHM_g and $M(\zeta)$ characteristics are symmetric about the centre of the avalanche region. As EHPs are injected from the edge of the avalanche region towards w, the value of $M(\zeta)$ drops to a minimum at $\zeta = 0.2w$. For all the EHPs injected before $\zeta = 0.2w$ only the primary electron can ionise and its ionising probability keeps decreasing as the injection position approaches $\zeta = 0.2w$. For $\zeta > 0.2w$, both the primary electron and hole have a finite probability of ionising and hence the multiplication value increases from the minima. It retains almost a fixed value before falling to a minimum at $\zeta = 0.8w$, as the electron and hole have equal ionising probability it rises back to its maximum at $\zeta = w$. Consequently the injection position also has effects on the distribution of gain, $P(g)$ leading to a

change in the FWHM$_g$. For $k = 1$ considered here the avalanche multiplication process depends heavily on the ionising probability of the secondary EHPs created. The primary electron ionisation probability reduces as the injection position approaches $\zeta = 0.2w$, it causes a large fluctuation in the multiplication obtained for each photon absorption event causing an increase in the FWHM$_g$ of *P(g)*. The value of FWHM$_g$ peaks at $\zeta = 0.2w$ after which it stays at a constant value until $\zeta = 0.8w$. Although for $\zeta > 0.2w$ the ionisation probability of the hole increases there is no reduction in FWHM$_g$ or increase in $M(\zeta)$. The uncertainties of ionisation in the large number of primary electrons injected per absorbed photon (1000 in this case) are seen to mitigate the increasing ionisation probability of the injected hole. The FWHM$_g$ drops after $\zeta > 0.8w$ and reaches a minimum again at $\zeta = w$.
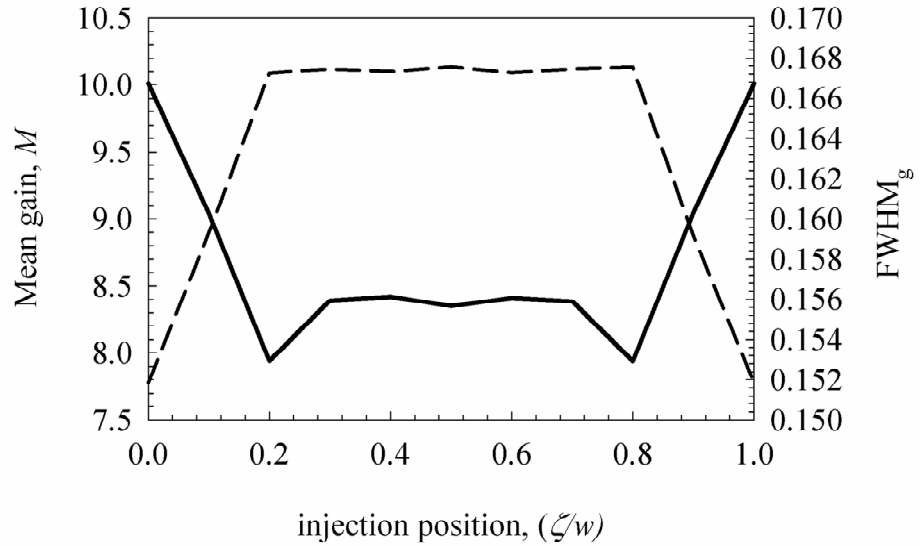
Figure 4.12 FWHM$_g$ (dashed) as a percentage of the mean gain (solid), M along the avalanche region for the case $k = 1$.

As dead spaces become significant only in thin avalanche regions, the improved FWHM$_g$ shown in figure 4.11 {a) will only be achieved using these avalanche region designs. The X-ray photon absorption in these thin structures will be substantially smaller when compared with thick avalanche regions. Since the gain distribution is also dependent on the X-ray photon interaction position,

thin avalanche region are also essential in minimising the distribution in gain and undesirable artifacts in the pulse height spectra due to avalanche statistics.

4.4 Summary

The avalanche gain distribution narrows as the number of carriers generated by X-ray photon absorption (dependent on the incident photon energy and the absorbing material) increase. The excess noise factors used in light detection APDs are thus not appropriate for X-ray APDs.

For a given mean gain, less fluctuation in gain, and hence a narrower $P(g)$ is obtained as the ionisation coefficients become disparate (i.e. k approaches zero). For low energy detection a material with a small k is essential. For higher energy detection materials with large k values would be still acceptable at reduced operational gain.

Dead space effects are shown to decrease the spread in avalanche multiplication distribution and hence improve the energy resolution in X-ray APDs. Mixed injection of carriers across the avalanche region exacerbates the spread in the gain distribution, except when $k = 1$. To minimise the spread in the gain distribution, photons should be absorbed predominantly in a non-avalanching region in the APD.

4.5 References

[1]   G. F. Knoll, *Radiation detection and measurement*: John Wiley & Sons, Inc, 2002.

[2]   L. M. P. Fernandes, F. D. Amaro, A. Antognini, J. M. R. Cardoso, C. A. N. Conde, O. Huot, P. E. Knowles, F. Kottmann, J. A. M. Lopes, L. Ludhova, C. M. B. Monteiro, F. Mulhauser, R. Pohl, J. M. F. d. Santos, L. A. Schaller, D. Taqqu, and J. F. C. A. Veloso, "Characterisation of large area avalanche photodiodes in X-ray and VUV-light detection," *Journal of Instrumentation,* vol. 2, p. P08005, 2007.

[3]   R. J. McIntyre, "Multiplication noise in uniform avalanche diodes," *Electron Devices, IEEE Transactions on,* vol. 13, pp. 164-168, 1966.

[4]   A. M. Barnett, J. E. Lees, D. J. Bassford, J. S. Ng, C. H. Tan, and R. B. Gomez, "Modelling results of avalanche multiplication in AlGaAs soft X-ray APDs," *Nuclear Instruments and Methods in Physics Research Section A: Accelerators, Spectrometers, Detectors and Associated Equipment,* vol. 626-627, pp. 25-30.

[5]   J. E. Lees, D. J. Bassford, J. S. Ng, C. H. Tan, and J. P. R. David, "AlGaAs diodes for X-ray spectroscopy," *Nuclear Instruments and Methods in Physics Research Section A: Accelerators, Spectrometers, Detectors and Associated Equipment,* vol. 594, pp. 202-205, 2008.

[6]   R. J. McIntyre, "The distribution of gains in uniformly multiplying avalanche photodiodes: Theory," *Electron Devices, IEEE Transactions on,* vol. 19, pp. 703-713, 1972.

[7]   J. Conradi, "The distribution of gains in uniformly multiplying avalanche photodiodes: Experimental," *Electron Devices, IEEE Transactions on,* vol. 19, pp. 713-718, 1972.

[8]   C. W. Helstrom, "Computing the performance of optical receivers with avalanche diode detectors," *Communications, IEEE Transactions on,* vol. 36, pp. 61-66, 1988.

[9]   M. Mansuripur, J. Goodman, E. Rawson, and R. Norton, "Fiber Optics Receiver Error Rate Prediction Using the Gram-Charlier Series," *Communications, IEEE Transactions on,* vol. 28, pp. 402-407, 1980.

[10]   S. D. Personick, "New results on avalanche multiplication statistics with applications to optical detection," *Bell Syst. Tech.,* vol. 50, 1971.

[11]   S. D. Personick, "Statistics of a general class of avalanche detectors, with applications to optical communication (1971)." *Bell Syst. Tech.,* vol. 50, 1971.

[12]   B. K. Ng, F. Yan, J. P. R. David, R. C. Tozer, G. J. Rees, C. Qin, and J. H. Zhao, "Multiplication and excess noise characteristics of thin 4H-SiC UV avalanche photodiodes," *Photonics Technology Letters, IEEE,* vol. 14, pp. 1342-1344, 2002.

[13]   Y. L. Goh, D. J. Massey, A. R. J. Marshall, J. S. Ng, C. H. Tan, W. K. Ng, G. J. Rees, M. Hopkinson, J. P. R. David, and S. K. Jones, "Avalanche Multiplication in InAlAs," *Electron Devices, IEEE Transactions on,* vol. 54, pp. 11-16, 2007.

[14]   L. J. J. Tan, J. S. Ng, C. H. Tan, M. Hopkinson, and J. P. R. David, "Effect of Dead Space on Low-Field Avalanche Multiplication in InP," *Electron Devices, IEEE Transactions on,* vol. 54, pp. 2051-2054, 2007.

[15]   S. A. Plimmer, J. P. R. David, G. J. Rees, and P. N. Robson, "Ionisation coefficients in $Al_xGa_{1-x}As$ (x = 0 - 0.60)," *Semiconductor Science and Technology,* vol. 15, p. 692, 2000.

[16]   M. M. Hayat, B. E. A. Saleh, and J. A. Gubner, "Bit-error rates for optical receivers using avalanche photodiodes with dead space," *Communications, IEEE Transactions on,* vol. 43, pp. 99-106, 1995.

[17]   M. M. Hayat, B. E. A. Saleh, and M. C. Teich, "Effect of dead space on gain and noise of double-carrier-multiplication avalanche photodiodes," *Electron Devices, IEEE Transactions on,* vol. 39, pp. 546-552, 1992.

[18]   D. S. Ong, K. F. Li, S. A. Plimmer, G. J. Rees, J. P. R. David, and P. N. Robson, "Full band Monte Carlo modeling of impact ionisation,

avalanche multiplication, and noise in submicron GaAs p^+-i-n^+ diodes," *Journal of Applied Physics,* vol. 87, pp. 7885-7891, 2000.

[19] S. A. Plimmer, J. P. R. David, B. Jacob, and G. J. Rees, "Impact ionisation probabilities as functions of two-dimensional space and time," *Journal of Applied Physics,* vol. 89, pp. 2742-2751, 2001.

[20] S. C. L. T. Mun, C. H. Tan, Y. L. Goh, A. R. J. Marshall, and J. P. R. David, "Modeling of avalanche multiplication and excess noise factor in $In_{0.52}Al_{0.48}As$ avalanche photodiodes using a simple Monte Carlo model," *Journal of Applied Physics,* vol. 104, pp. 013114-6, 2008.

[21] D. S. Ong, K. F. Li, G. J. Rees, J. P. R. David, and P. N. Robson, "A simple model to determine multiplication and noise in avalanche photodiodes," *Journal of Applied Physics,* vol. 83, pp. 3426-3428, 1998.

[22] C. Groves, J. P. R. David, G. J. Rees, and D. S. Ong, "Modeling of avalanche multiplication and noise in heterojunction avalanche photodiodes," *Journal of Applied Physics,* vol. 95, pp. 6245-6251, 2004.

[23] C. H. Tan, R. Ghin, J. P. R. David, G. J. Rees, and M. Hopkinson, "The effect of dead space on gain and excess noise in $In_{0.48}Ga_{0.52}P$ p^+-i-n^+ diodes," *Semiconductor Science and Technology,* vol. 18, p. 803, 2003.

[24] B. K. Ng, J. P. R. David, R. C. Tozer, G. J. Rees, Y. Feng, J. H. Zhao, and M. Weiner, "Nonlocal effects in thin 4H-SiC UV avalanche photodiodes," *Electron Devices, IEEE Transactions on,* vol. 50, pp. 1724-1732, 2003.

Chapter 5 InAs avalanche photodiodes for X-ray detection

5.1 Introduction

X-ray detectors with low thresholds and energy resolution in the sub 100 eV range are required in astrophysics and other industrial applications. Superconductor radiation detectors that have the potential for achieving this low resolution have been investigated [1, 2]. A superconducting tunnel junction detector has also been shown to achieve statistical limited resolution performance in the 0.2 to 1 keV energy range when cooled to 0.1 K [3]. A similar high resolution performance has been obtained at higher energies using 5.9 keV X-rays [4].

	Semiconductors			
	InSb	InAs	Ge	Si
Atomic numbers	49,51	49,33	32	14
Band gap (eV)	0.165	0.36	0.67	1.11
Density (gm/cm^3)	5.78	5.68	5.32	2.33
Electron mobility (cm^{2}V^{-1}s^{-1})	77000	40000	3900	1400
Hole mobility (cm^{2}V^{-1}s^{-1})	850	500	1900	450
Operating temperature	<77 K	77 K	77 K	Room temperature
Fano limit @5.9 keV	68	85	99	115

Table 5.1 Comparison of semiconductor properties for radiation detection.

Despite the high resolution performance of superconductors these devices suffer from high capacitance per unit area. They also have absorber thickness

within the sub micrometer range making them inefficient for detection in the tens of keV range. The operation of superconductors is also restricted to the very low temperatures below 1 K, for semiconductor detectors such high resolution cannot be achieved with elemental Si and Ge due to the statistical limit and thus requires the exploration of other potential semiconductor materials. Table 5.1 shows the comparison of two narrow band gap III-V compound semiconductors (InSb and InAs) with Si and Ge. These compound semiconductors possess high atomic numbers and crystal densities making them ideal for enhanced detection efficiency at higher energies. The narrow band gap leads to low electron hole pair creation energy. Since fano-limited energy resolution is proportional to the square root of the pair-creation energy, these materials have the potential to provide better energy resolution than Si and Ge. To calculate the statistical limit best available values of fano factors have been used for the calculations for the fano limited energy resolution for Si and Ge [5]. Since no measured fano factors for InAs and InSb are available, a conservative value of 0.14 is assumed [6].

McHarris first highlighted the advantages of using InSb for X-ray detection along with its pitfalls [7]. Despite their potential, X-ray detectors based on InSb have only been investigated by a group at Kyoto University [8, 9]. Their most recent work has shown the detection of gamma rays [10] and alpha particles [11]. These diodes were cooled to very low cryogenic temperature (4.2 - 5.4 K) to avoid high leakage currents contributing to noise in the detection system. Using InSb wafer grown by liquid phase epitaxy, an E_R = 2.4 % was achieved for 5.5 MeV alpha particles when the diode was cooled to 5.4 K [12]. With a wider band gap and similar atomic numbers compared to InSb, InAs is expected to exhibit leakage currents much lower than those of InSb, whilst largely retaining high X-ray detection efficiency. InAs is therefore an attractive choice for better energy resolution detectors operating at higher temperatures than InSb. A pixel matrix detector fabricated by Zn diffusion has been the only reported work on InAs radiation detectors [13]. The detector placed in liquid nitrogen was shown to detect alpha particles but showed very poor resolution which was attributed to the high leakage current of the detector. This severely

limited the detector's ability to resolve X-ray and gamma ray peaks. High leakage current further inhibited the diodes to be biased to a higher voltage and prohibited a meaningful determination of the FWHM of the detected peaks.

Well designed APDs can help improve the signal to the noise ratio of the detector and the FWHM of the detected photo peak. This is a significant advantage in applications that require low energy thresholds like X-ray fluorescence studies and detection of elements with small atomic numbers. Recently high quality epitaxially grown InAs photodiodes have been reported [14, 15]. Surface leakage currents were suppressed in these diodes over a wide range of temperature such that the leakage current was dominated by bulk mechanism. Additionally, within the electric field range studied, these diodes exhibit the ideal avalanche characteristics, i.e. only electron initiated impact ionisation process [14]. This yields avalanche gain M, with very low excess noise factors, consistent with McIntyre's excess noise theory [16]. The highly desirable single carrier ionisation characteristic can be exploited to produce high gain in X-ray APDs without significant degradation of the energy resolution. This can lead to X-ray APDs with high resolution and greatly improves signal to noise performance.

This chapter reports InAs X-ray APDs for detection of soft X-ray photons below 10 keV and exhibits the improving FWHM with avalanche gain. The effects of the avalanche gain on the signal to noise ratio are studied and discussed. The avalanche gain statistics model presented in chapter 4 is used to quantify the avalanche contribution of the APD. This is the first investigation into the detection of soft X-rays using InAs and the demonstration of an InAs X-ray APD.

5.2 APD structure

The InAs APD used was grown and fabricated at the National Centre for III-V Technologies at the University Of Sheffield. It has an n^+ip^+ configuration,

grown on a p-type InAs substrate using metal organic vapour phase epitaxy (MOVPE) at a growth temperature of 600 °C. The p-type cladding was 2 μm thick and doped with Zn to a concentration of $\sim 1 \times 10^{18}$ cm^{-3}. The 2 μm thick n-type region was doped with Si to a concentration of $\sim 2 \times 10^{17}$ cm^{-3}. The 6 μm wide intrinsic region was undoped but the depletion achieved was limited by its unintentional n-type background doping concentration of $\sim 2 \times 10^{15}$ cm^{-3}.
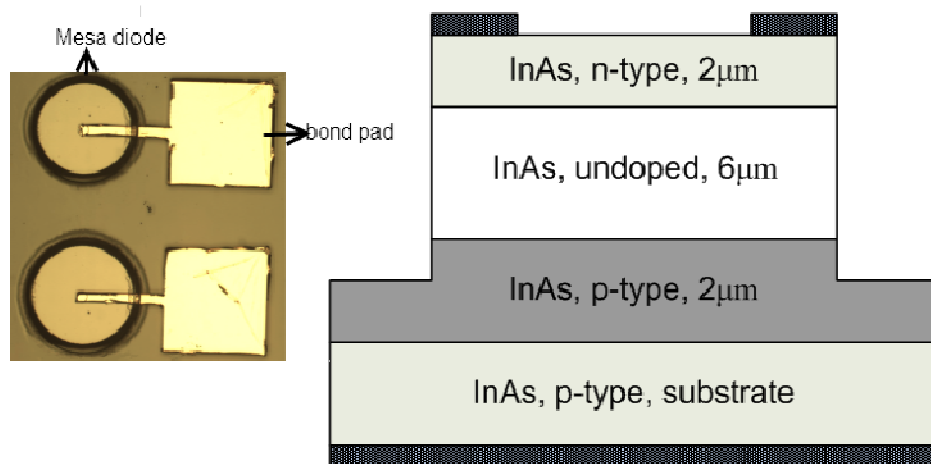

Figure 5.1 Schematic cross section of an InAs n$^+$ip$^+$ APD, also shown is the top view of mesa etched InAs APDs with remote bond pads.

Circular mesa diodes were fabricated by using wet chemical etching and photolithographic techniques described in detail in [17]. The wet etching was carried out using a 1:1:1 mixture of phosphoric acid, hydrogen peroxide, and de-ionised water followed by another etch using a 1:8:80 mixture of sulphuric acid, hydrogen peroxide, and de-ionised water. The cross section of the diode along with the top view of fabricated mesa diodes is shown in figure 5.1. Ti/Au was deposited by metal evaporation to form both the p- and n-type contacts. Annular (or dot) contacts were deposited on the top of the device while a large contact was deposited at the back of the substrate by thermal evaporation. The etched mesa walls were passivated by depositing SU-8 to preserve the diode leakage current characteristics. Diodes with 100 μm diameter were bonded using gold wires to a TO-5 package for X-ray measurements. Due to its narrow band gap the bulk dark current is prohibitively high for room temperature

measurements. Fortunately the bulk leakage current decreases rapidly with temperature, exhibiting ~150 nAcm^{-2} leakage currents at low reverse bias when the device is cooled to 77 K. The typical characteristics and a rigorous analysis of the temperature dependence of leakage current in InAs APDs have been performed by Ker *et al.* [15].

X-ray measurements were performed using the characterisation system described in chapter 3. The T0-5 package was placed in a vacuum Dewar filled with liquid nitrogen to achieve a temperature of 77 K. The sample was irradiated with a ^{55}Fe radioactive X-ray source (with Mn K$_\alpha$ and K$_\beta$ peaks at 5.9 keV and 6.49 keV) placed 0.5 cm away from the diode. Pulse height spectra were then obtained from the diodes by varying the reverse bias voltage.

5.3 APD response

5.3.1 X-ray spectra

Pulse height spectra of two InAs APDs, D1 and D2, are shown in figure 5.2. The 5.9 keV X-ray peak shifts away from the electronic noise floor with increasing reverse bias. A unity gain peak was observed at channel 41 (figure 5.2(b)) of the MCA at a reverse bias of 1 V. The maximum reverse bias applied to D1 and D2 were limited to 10.8 and 9.5 V since at higher bias the potential drop across the biasing resistor of the preamplifier became unacceptably high. Since the MCA was calibrated for zero offset using a precision pulse generator (such that channel 0 represents the actual 0 value of the spectrometer), M for a given diode was deduced from the ratio of peak channel numbers to the unity gain channel number (41). Maximum effective avalanche gain of 5.3 for D1 and 4.1 for D2 were obtained. Since the X-ray absorption takes place in all the epilayers of the diode the multiplication characteristics result from mixed carrier injection that affect the pulse height spectra.

The unity gain voltage was set at 1 V, corresponding to a peak at channel number 41. The peak at channel number 41 is seen to show no shift when the reverse bias is increased from 0 to 1 V, the region which corresponds to the steep increase in the depletion region of the APD. The capacitance of the APD measured at 77 K is shown in Figure 5.3. A depletion region of ~3.2 μm is achieved at the highest measured reverse bias voltage of 10.8 V. The increase in depletion region width is seen to have negligible effects on the charge collection efficiency particularly attributed to the long minority carrier lifetimes in InAs [18]. For InAs grown by vapour phase epitaxy the carrier lifetime was shown to lie between 10^{-6} to 10^{-7} s for temperatures ranging from 77 to 300 K. The unity gain peak voltage has also been verified by light measurements discussed in the following section.
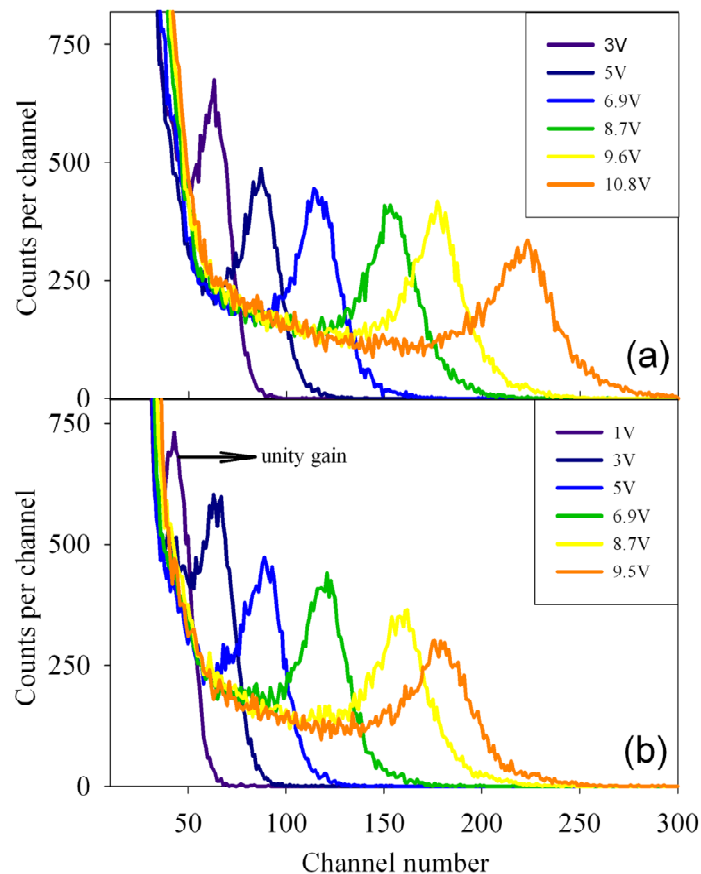

Figure 5.2 Pulse height spectra obtained from (a) D1 and (b) D2 irradiated by a ^{55}Fe X-ray source with increasing reverse bias.
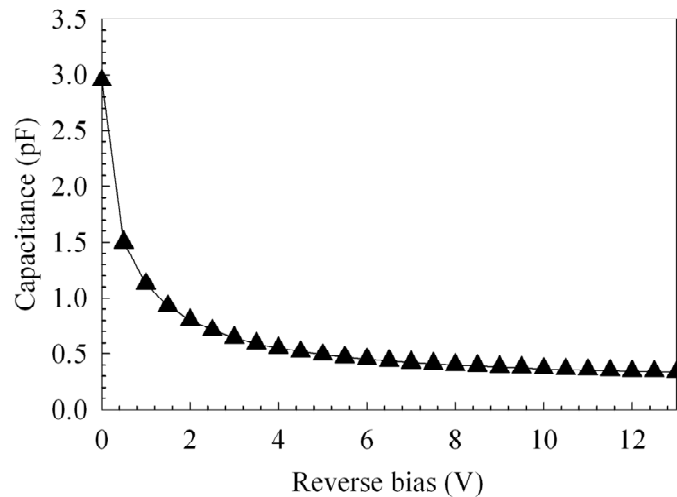
Figure 5.3 C-V characteristics of an InAs APD with 100μm diameter measured at 77 K.

5.3.2 Visible light measurements

Due to the onset of impact ionisation in InAs APDs at fields as low as ~3 kVcm^{-1}, avalanche gain was observed at very low bias. On the contrary typical Si X-ray APDs exhibit useful gain at much higher electric fields > 90 kVcm^{-1} [19]. The values for M deduced from the X-ray spectra are compared with those from visible laser measurements, shown in figure 5.4. A 633 nm wavelength laser was used to generate the primary photocurrent for these measurements.

To achieve a mixed carrier injection profile the laser was focused on the edge of the mesa structure such that electron-hole pairs were generated in all the epilayers. The variability in the positioning of the laser spot on the edge of the device will produce varying degrees of mixed injection leading to a spread in the measured gain. Measurements on a number of devices are shown in figure 5.4. The avalanche gains derived from the laser measurements are in good agreement with that obtained from X-ray measurements, as shown in figure 5.4. The higher gain measured on one of the devices was due to the larger proportion of electron injection generated by the 633 nm laser.
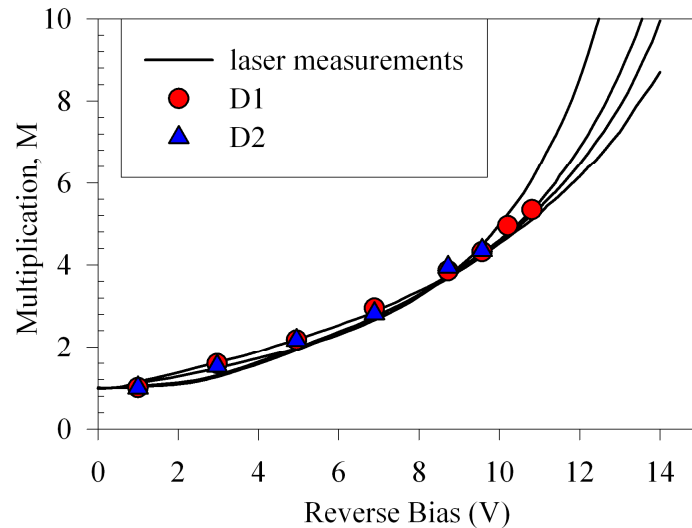
Figure 5.4 Comparison of avalanche multiplication factors obtained from a 633 nm laser and X-rays performed at 77 K.
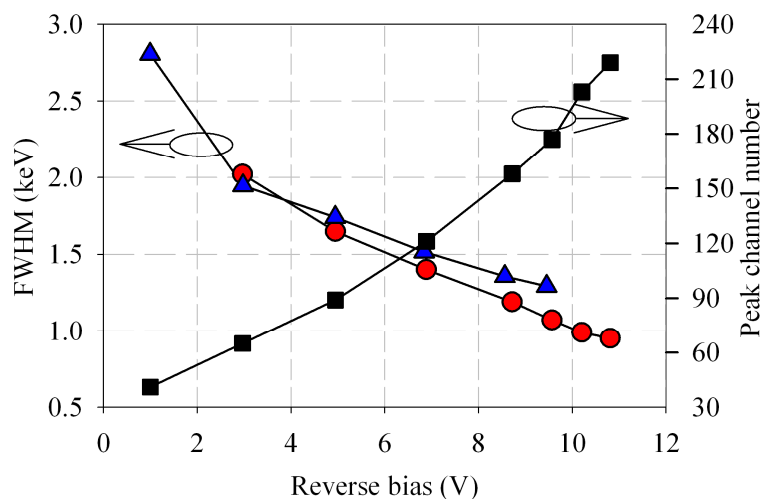
Figure 5.5 FWHM (left axis) of the 5.9 keV peak from D1 (circles) and D2 (triangles) versus reverse bias, along with the peak channel numbers (closed squares, right axis) (the lines are included for visualisation purposes).

5.4 Energy resolution

The calibration of the spectra for photon energy in terms of keV was obtained using the electronic noise peak and the detected X-ray peak corresponding to 5.9 keV photons. Gaussian curves were then fitted to the

experimental spectra to obtain the energy resolution given by the FWHM of the detected 5.9 keV X-ray peak. Figure 5.5 shows the FWHM as a function of reverse bias. As the reverse bias increases the FWHM drops substantially. A FWHM of 2.02 keV at $M = 1.58$ reducing to 0.95 keV at $M = 5.3$ for the 5.9 keV X-ray photons was obtained for D1. D2 showed a FWHM of 2.8 keV at $M = 1$ reducing to 1.3 keV at $M = 4.3$. Also shown in figure 5.5 is the corresponding increment in the peak channel number with bias for D1.
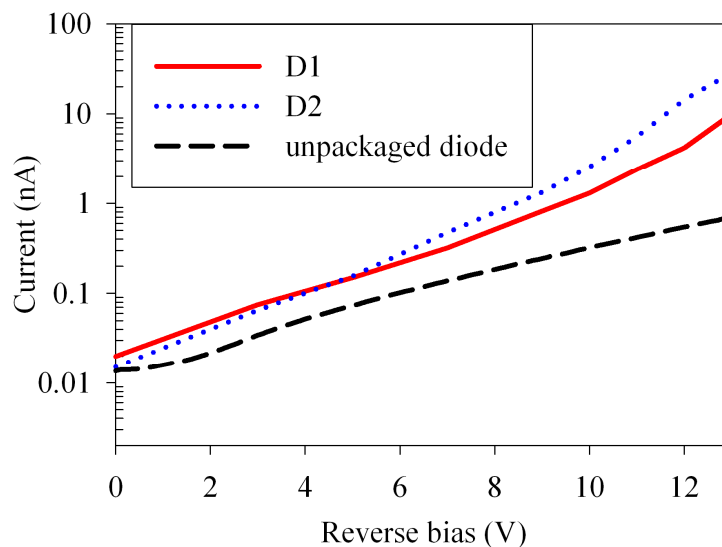
Figure 5.6 Comparison of the reverse bias dark currents from diodes D1, D2 and unpackaged InAs APDs measured at 77 K.

The discrepancy in the measured FWHM at higher bias can be attributed to the higher leakage currents of D2 compared to D1, shown in figure 5.6. The X-ray detection measurements were limited to a maximum gain of 5.3 by the increase in dark current of the detector limiting the useful gain of the detector. Tunnelling current kicks in at around 11 V in the measured devices. The leakage current in the packaged devices was considerably higher than unpackaged devices, possibly due to increased surface leakage current caused by non-optimised packaging procedures. The shot noise from the diode leakage current increases the parallel white noise contribution. InAs APDs with thicker avalanche regions would achieve higher gain for a given bias, increasing the maximum useful gain. A wider depletion region would also reduce the electric

field delaying the onset of tunnelling. A thicker structure would also increase detection efficiency at higher energies.

5.5 Model

The fano-limited energy resolution for InAs for the 5.9 keV X-ray photon can be obtained as follows. With a pair creation energy, $\varepsilon = 1.56$ eV (from Klein's empirical equation [20]) and a fano factor, f of 0.14 [6] a fano-limited energy resolution given by,

$$E_F = 2.36\sqrt{fE\varepsilon} = 84.6eV \ \text{(eV)} \ ,\tag{5.1}$$

where $E = 5.9$ keV, the incident photon energy. The experimental FWHM is significantly larger than this theoretical limit. To study this, the gain distribution of the InAs APD was simulated using the RPL model discussed in chapter 4.

5.5.1 Avalanche gain statistics

The spread in avalanche gain from the model can be combined with the electronic noise contributions from the leakage current and read out electronic circuit as well as the intrinsic fano spread to model the experimental spectrum. The RPL model used parameterised equation for the electron ionisation coefficient α at 77 K from ref [21]. The parameterised equations are obtained assuming that the diode has an ideal n^+ip^+ structure and the hole ionisation coefficient, $\beta = 0$. Hence for the electric field range in this study we have

$$\alpha(\xi) = 3.91 \times 10^4 exp\left[-\left(\frac{2.62 \times 10^5}{|\xi|}\right)^{0.342}\right] \text{cm}^{-1}.\tag{5.2}$$

Excess noise factors measured in InAs are seen to be well lower than the lowest limit predicted by McIntyre's local model. This discrepancy has been attributed to the dead space, d, which has been included in the model. As

shown in chapter 4 significant dead space can improve the gain-limited energy resolution. A value of $\alpha d = 0.08$, derived from modelling of the experimentally obtained excess noise factors was assumed. The position of interaction ζ, for each photon was calculated using absorption coefficients from ref [22]. Using the equation $\zeta = -(1/\varphi)\ ln(R)$ (where R is random number uniformly distributed between 0 and 1). The electric field profile in the APD was assumed to be constant across the avalanche region. An emission probability ratio of $P_{K\beta}\ /\ P_{K\alpha}$ = 0.138 for the ^{55}Fe source was used [23]. A charge collection of 100 % within the p region has been assumed due to the long minority electron diffusion length in the p$^+$ region of InAs [18].

The simulated spectrum for D1 at M = 5.3 (bias = 10.8 V) is shown in figure 5.7. The counts in the peak of the simulated spectra were normalised to the experimental data as the total number of photons radiated on the device was unknown. The simulated avalanche gain-limited spectrum has two peaks corresponding to 5.9 keV (larger) and 6.49 keV (smaller). Additionally an unmultiplied X-ray peak is seen at channel 41. An avalanche gain limited energy resolution, E_G = 172 eV was predicted for the main peak at 5.9 keV. This is seen to be sufficiently small to resolve the 6.49 keV X-ray peak. The simulated spectrum reveals considerable absorption in the top n-cladding layer and the avalanche region of the APD, resulting in a range of intermediate gain values. These correspond to counts between channels 41-200, degrading the peak-to-background ratio in the spectrum. Since the hole does not impact ionise the pure electron injection peak shifts away from the unity gain peak. This results in negligible interference between the two peaks at high gains. Due to the considerably thick avalanche region width the peak to background ratio is much higher than expected. Characteristic X-rays with energies lower than the incident X-ray can be emitted by the constituent atoms. These low energy X-rays are usually reabsorbed, if they escape the detector it can result in X-ray escape peaks in the lower end of the energy spectra. The probability of emission of characteristic X-rays is dependent on the energy of the incident X-ray i.e. if the incident energy is higher than the absorption edge of the constituent atoms and its fluorescence yield. Since the number of X-rays that escape the detector

can be relatively low, a good peak to background ratio is necessary to recover these peaks in addition to the requirement of a low energy threshold.
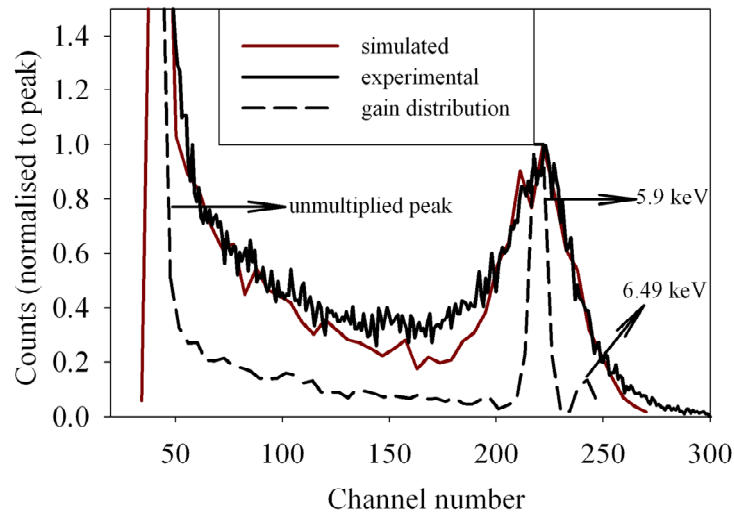
Figure 5.7 Comparison of simulated and experimental spectra for D1 at reverse bias 10.8 V ($M = 5.3$), along with the gain distribution of the diode.

Figure 5.8 shows the unity gain spectra at a reverse bias of 1V in comparison with the spectra at a gain of 6.1. The lower electronic noise floor enables the observation of the unity gain peak at higher bias. The large separation between the peaks helps in observing photo peaks (if present) at intermediate energies.
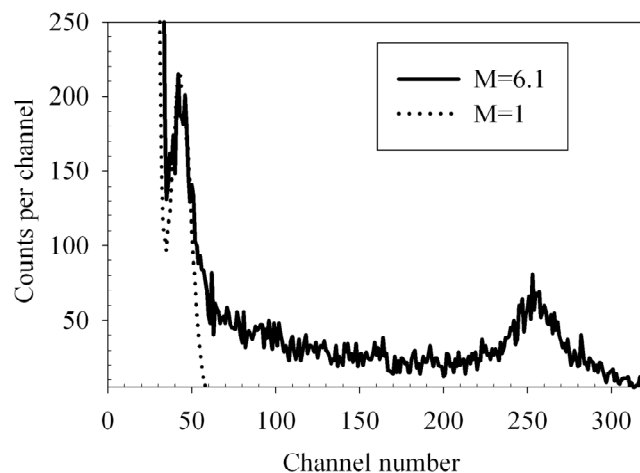
Figure 5.8 Comparison of pulse height spectra obtained from an InAs APD at unity gain and a gain of 6.1.

5.5.2 Noise
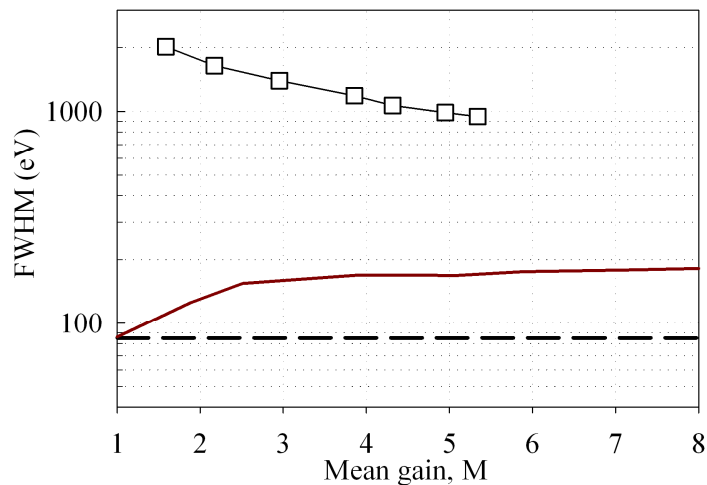
Figure 5.9 Calculated FWHM due to avalanche gain, E_G (solid line) and fano limit, E_F (dashed line) compared to the experimental FWHM of D1 (squares).

Figure 5.9 compares the experimental FWHM with the gain and fano-limited FWHM values in terms of energy. At all avalanche gains, the experimental FWHM is much higher than the fano limited resolution, E_F, and avalanche statistics limited resolution, E_G, indicating that these noise sources intrinsic to the APD are insignificant compared to the electronic noise (including leakage current and diode and other stray capacitance). For $M \geq 3$, E_G remains constant at ~172 eV, independent of the gain. The measured excess noise factors in InAs are shown to be extremely low and independent of avalanche gain for a primary photocurrent generated by electrons [21]. The dead space reduces E_G from 213 to 172 eV confirming that carefully designed APDs could exploit the dead space effects to improve the energy resolution. To experimentally verify this effect the electronic noise contribution has to be comparable to the intrinsic noise of the APD.

It is clear that the measured spectrum has a much wider distribution than the simulated avalanche gain limited spectrum (dashed line figure 5.7). This is attributed to the noise contributions from the preamplifier-APD system which

can be mainly divided into a parallel and series white noise components (section 2.9) [24, 25]. The diode leakage current is the major contributor to the parallel white noise in the current system while the bias resistor and the preamplifier feedback resistor will also contribute towards the parallel noise. Since the parallel noise is directly proportional to the shaping time of the amplifier a small shaping time was used in these measurements to minimise parallel noise. The second noise component is the series white noise in the system, which originates from the input JFET of the preamplifier. The series white noise is proportional to the sum of the capacitances from the detector, input JFET, stray (diode packaging and cabling) and feedback capacitor. It is however inversely proportional to the shaping time used. Since a small shaping time (0.5 µs) was used for these measurements the series white noise was an important factor at all measured gain values.

The system electronic noise, E_N, was subtracted in quadrature from the expression for the total measured energy resolution, E, such that $E^2 = E_G^2 + E_N^2 + E_F^2$. E_N is then used as a fitting parameter and a good fit is obtained as seen in Figure 5.7.
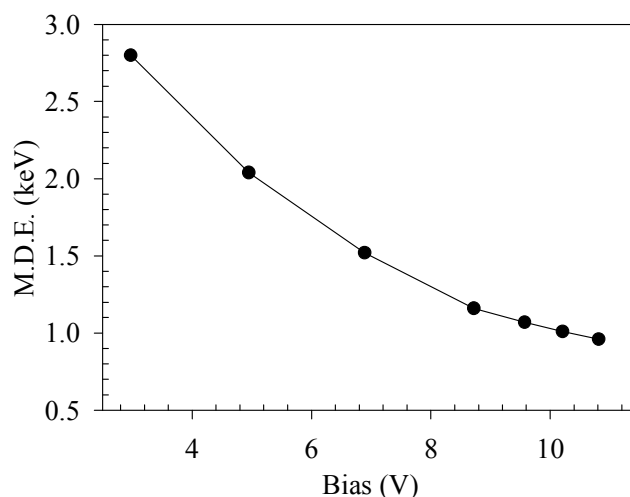

Figure 5.10 MDE with increasing reverse bias (Lines are for visualisation purposes).

Although the avalanche gain will always add to the total spread in energy resolution the gain helps improve the FWHM in systems dominated by the series white noise. The improved signal to noise ratio also helps in the reduction of the low energy threshold of the system. Since detection of light elements requires the threshold to be as low as possible, APDs could be important in such applications. A rudimentary extraction of the minimum detectable energy (MDE) from the measured spectra has been performed. MDE is usually defined as the minimum energy at which X-ray events are measured from a detector above the electronic noise tail. The MDE here is determined by the intercept of a Gaussian curve to the abscissa which is fitted to the measured electronic noise peak of the spectra. A rapid improvement in the MDE is seen at higher reverse bias as shown in Figure 5.10. The MDE reduces from 2.8 keV at $M = 1.58$ to ~1 keV at $M = 5.3$. Although the leakage current increases at higher bias it is not seen to affect the MDE within the range of measured data. For low energy X-rays the avalanche gain helps improve the signal strength above the noise floor thus improving the MDE. Since InAs APDs exhibit very low excess noise that is independent of avalanche gain, the effect of gain fluctuation on MDE is not important. Hence the electronic noise is the most important parameter to achieve the lowest possible MDE as well as maintain good spectral resolution. For each APD a compromise between dark current and avalanche gain has to be independently chosen to determine the best operating voltage.

5.6 Response to ^{241}Am

The InAs n$^+$ip$^+$ was also used to study its response to higher energy X-rays. A ^{241}Am X-ray source with principal emissions as listed in table 3.1 was used. The I-V characteristic of the diode packaged on a TO-5 header used to carry out the measurement is shown in figure 5.11, measured at room temperature and at 77 K. The measurements are performed at 0 V where the dark current was measured to be 50 pA (77 K). The depletion region is estimated to be 1.13 μm at 0 V, inferred from C-V measurements. The long minority carrier lifetimes

in InAs enable the measurements to be performed without any external reverse bias.
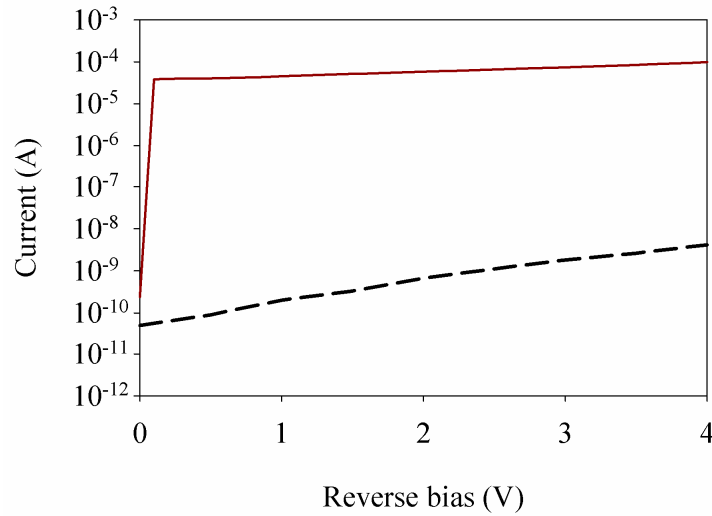
Figure 5.11 I-V characteristics of an InAs n^+ip^+ diode at room temperature (solid line) and 77 K (dashed line).

The spectrum collected over duration of 12 hours with an amplifier shaping time of 2 μs, as shown in figure 5.12. The 13.9 and 17.8 keV doublets have been clearly resolved. The insert in figure 5.12 shows the spectrum obtained form a [55]Fe source, the 5.9 keV energy peak is clearly resolved above the noise floor with a peak to background ratio of 10:1.

The large time required for sufficient collection of counts to build the pulse height spectra is due to the low quantum efficiency of the detector at higher energies (largely limited by its active layer thickness) and also restricted by the low activity of the [241]Am source (406 kBq). Figure 5.13 shows the calculated quantum efficiency of the InAs diode, a diode active region thickness of 10 μm was used. This assumption is made while considering the large carrier diffusion lengths in InAs. The quantum efficiency is calculated to be 0.89 and 0,02 at 5.9 and 59.5 keV respectively, which is much higher than 0.28 and 2.98×10^{-4} respectively for Si with comparable thickness. This is mainly attributed to the larger atomic numbers and crystal density of InAs. Diodes with increased active region thickness are required for improved efficiency at higher energies.
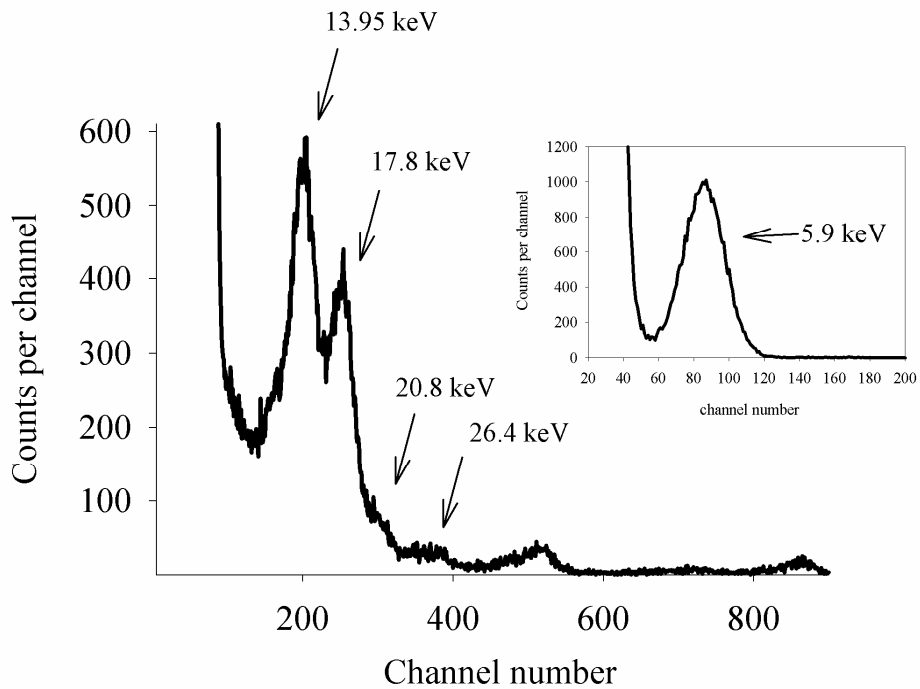
Figure 5.12 Spectrum collected from a ^{241}Am gamma ray source, with the device biased at 0 V at an amplifier shaping time of 2 μs. The insert also shows spectrum collected from a ^{55}Fe X-ray source at the same conditions (the ^{55}Fe source has an activity of 185 MBq, the collection time was 48 seconds).

The pulse height spectrum is re-plotted in figure 5.14 in a log scale to observe the gamma ray response of the diode. The higher energy gamma ray γ_2 at 59.5 keV has the highest emission probability of 0.35. It can be seen that γ_2 has been resolved by the detector. The spectrum also shows additional features related to the escape of indium or arsenic photons. The energy of γ_2 is much higher than the K shell binding energy of both As and In and hence escape peaks can be seen in the spectrum in addition to those arising from the capture of photons emitted by the source. Table 5.2 and 5.3 show the K shell florescence line energies along with their fractional radiative rates for In and As respectively [26, 27].
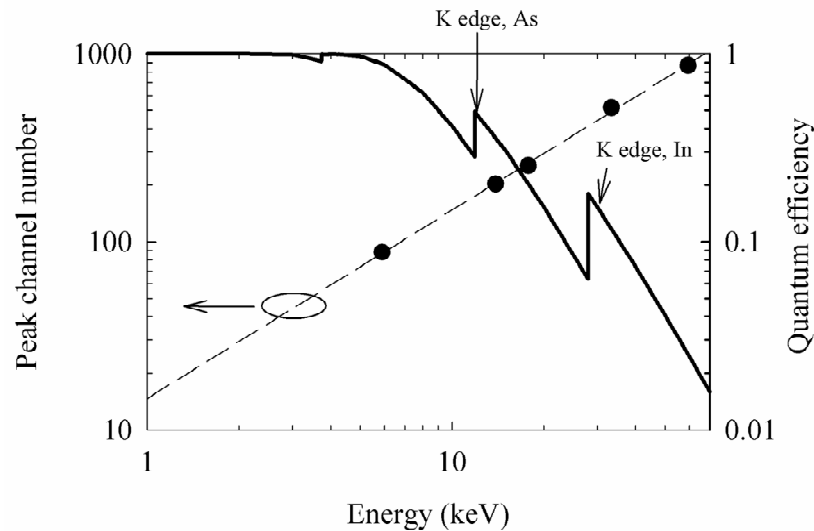
Figure 5.13 The calculated quantum efficiency (right vertical axis) of InAs diodes with 10 μm thickness. The discontinuities in the curve correspond to the absorption edge of the constituent atoms (K-edge In = 27.94 keV, K edge As =11.86 keV and also seen is the L edge discontinuity for In = 3.93 keV). The figure also shows the plot of the linearity of the detector up to 60 keV (closed circles).
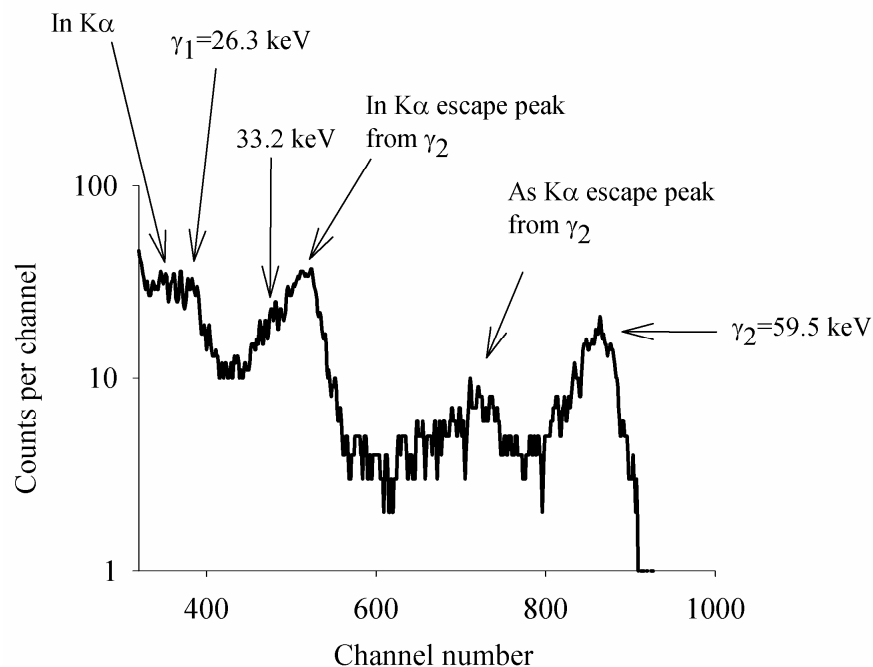
Figure 5.14 Log plot showing the pulse height spectrum of the gamma rays detected from the [241]Am source. The escape and fluorescence peaks from the constituent atoms are also identified

	Kα$_1$	Kα$_2$	Kβ$_1$	Kβ$_3$
Line energy (keV)	24.210	24.002	27.276	27.237
Radiative rate	0.535	0.285	0.099	0.051

Table 5.2 In florescence line energies along with their respective fractional radiative rates [26, 27].

	Kα$_1$	Kα$_2$	Kβ$_1$	Kβ$_3$
Line energy(keV)	10.543	10.507	11.726	11.720
Radiative rate	0.571	0.294	0.086	0.044

Table 5.3 As florescence line energies along with their respective fractional radiative rates [26, 27].

The Kα$_1$and Kα$_2$ escape peak for In from γ_2 are too similar in energy to be resolved and seen as a single peak at 35.3 keV in the measured spectrum. Similarly the Kα$_1$and Kα$_2$ escape peak for As from γ_2 have been partially resolved in the spectrum as shown in figure 5.14. The low energy shoulder near the Kα escape peak for In from γ_2 is postulated to be the 33.2 keV gamma ray emitted by the source. The As escape peaks from 13.95, 17.8 and 20.8 keV X-ray have not been resolved. The Kα fluorescence peak from In at 24.2 keV is in close proximity to the γ_1 peak at 26.3 keV (from the [241]Am source with emission probability of 0.023) and have been partially resolved in the pulse height spectrum. A FWHM of 2.58 keV is obtained for the peak at 13.95 keV corresponding to $E_R = 18.5$ %, a modest resolution for the detector biased at 0 V. Fitting a Gaussian to the 59.5 keV peak gives an $E_R = 4.5$ %.

5.7 Summary

InAs APDs have been show to detect soft X-rays. The energy resolution of the detected photo peak was shown to improve significantly with avalanche gain. The avalanche gain also helped improve the overall signal to noise ratio of the detection system thus increasing its low energy threshold. A gamma ray source has also been used to detect higher energy X-rays without any external bias with reasonable resolution.

The energy resolution is still significantly poorer than the fano limited value. A reduction in the series electronic noise along with the diode leakage current is necessary to achieve better spectral performance. Operating the APD at higher gain would reduce the series white noise such that the performance is limited by the shot noise from the leakage current of the detector. Modelling results have shown that the avalanche gain limited energy resolution can be independent of gain, due to the desirable single carrier ionisation characteristics in InAs.

5.8 References

[1]   M. C. Gaidis, S. Friedrich, K. Segall, D. E. Prober, A. E. Szymkowiak, and S. H. Moseley, "A superconducting X-ray spectrometer with a tantalum absorber and lateral trapping," *Applied Superconductivity, IEEE Transactions on,* vol. 6, pp. 1-4, 1996.

[2]   S. Friedrich, J. B. Le Grand, L. J. Hiller, J. Kipp, M. Frank, S. E. Labov, S. P. Cramer, and A. T. Barfknecht, "High resolution tunnel junction extreme ultraviolet detectors limited by quasiparticle counting statistics," *Applied Superconductivity, IEEE Transactions on,* vol. 9, pp. 3330-3333, 1999.

[3]   J. B. le Grand, C. A. Mears, L. J. Hiller, M. Frank, S. E. Labov, H. Netel, D. Chow, S. Friedrich, M. A. Lindeman, and A. T. Barfknecht, "A superconducting tunnel junction x-ray detector with performance limited by statistical effects," *Applied Physics Letters,* vol. 73, pp. 1295-1297, 1998.

[4]   L. Li, L. Frunzio, C. Wilson, D. E. Prober, A. E. Szymkowiak, and S. H. Moseley, "Improved energy resolution of x-ray single photon imaging spectrometers using superconducting tunnel junctions," *Journal of Applied Physics,* vol. 90, pp. 3645-3647, 2001.

[5]   B. G. Lowe, "Measurements of Fano factors in silicon and germanium in the low-energy X-ray region," *Nuclear Instruments and Methods in Physics Research Section A: Accelerators, Spectrometers, Detectors and Associated Equipment,* vol. 399, pp. 354-364, 1997.

[6]   A. Owens and A. Peacock, "Compound semiconductor radiation detectors," *Nuclear Instruments and Methods in Physics Research Section A: Accelerators, Spectrometers, Detectors and Associated Equipment,* vol. 531, pp. 18-37, 2004.

[7]   W. C. McHarris, "InSb as a γ-ray detector," *Nuclear Instruments and Methods in Physics Research Section A: Accelerators, Spectrometers, Detectors and Associated Equipment,* vol. 242, pp. 373-375, 1986.

[8]   I. Kanno, F. Yoshihara, R. Nouchi, O. Sugiura, T. Nakamura, and M. Katagiri, "Cryogenic InSb detector for radiation measurements," *Review of Scientific Instruments,* vol. 73, pp. 2533-2536, 2002.

[9]   Y. Sato, Y. Morita, T. Harai, and I. Kanno, "Photopeak detection by an InSb radiation detector made of liquid phase epitaxially grown crystals," *Nuclear Instruments and Methods in Physics Research Section A: Accelerators, Spectrometers, Detectors and Associated Equipment,* vol. 621, pp. 383-386.

[10]   S. Hishiki, Y. Kogetsu, I. Kanno, T. Nakamura, and M. Katagiri, "First detection of gamma-ray peaks by an undoped InSb Schottky detector," *Nuclear Instruments and Methods in Physics Research Section A: Accelerators, Spectrometers, Detectors and Associated Equipment,* vol. 559, pp. 558-560, 2006.

[11]   Y. Sato, Y. Morita, T. Harai, and I. Kanno, "Alpha-particle response of an InSb radiation detector made of liquid-phase epitaxially-grown crystal," *Radiation Measurements,* vol. 46, pp. 1654-1657.

[12]   I. Kanno, S. Hishiki, O. Sugiura, R. Xiang, T. Nakamura, and M. Katagiri, "InSb cryogenic radiation detectors," *Nuclear Instruments and Methods in Physics Research Section A: Accelerators, Spectrometers, Detectors and Associated Equipment,* vol. 568, pp. 416-420, 2006.

[13]   A. Saynatjoki, P. Kostamo, J. Sormunen, J. Riikonen, A. Lankinen, H. Lipsanen, H. Andersson, K. Banzuzi, S. Nenonen, H. SipilÃ, S. VaijÃrvi, and D. Lumb, "InAs pixel matrix detectors fabricated by diffusion of Zn in a metal-organic vapour-phase epitaxy reactor," *Nuclear Instruments and Methods in Physics Research Section A: Accelerators, Spectrometers, Detectors and Associated Equipment,* vol. 563, pp. 24-26, 2006.

[14]   A. R. J. Marshall, T. Chee Hing, M. J. Steer, and J. P. R. David, "Extremely Low Excess Noise in InAs Electron Avalanche Photodiodes," *Photonics Technology Letters, IEEE,* vol. 21, pp. 866-868, 2009.

[15]   K. Pin Jern, A. R. J. Marshall, A. B. Krysa, J. P. R. David, and T. Chee Hing, "Temperature Dependence of Leakage Current in InAs Avalanche Photodiodes," *Quantum Electronics, IEEE Journal of,* vol. 47, pp. 1123-1128.

[16]   R. J. McIntyre, "Multiplication noise in uniform avalanche diodes," *Electron Devices, IEEE Transactions on,* vol. 13, pp. 164-168, 1966.

[17]   A. R. J. Marshall, C. H. Tan, J. P. R. David, J. S. Ng, and M. Hopkinson, "Fabrication of InAs photodiodes with reduced surface leakage current," in

Optical Materials in Defence Systems Technology IV, Florence, Italy, 2007, pp. 67400H-9.

[18]   V. L. Dalal, J. W. A. Hicinbothem, and H. Kressel, "Carrier lifetimes in epitaxial InAs," *Applied Physics Letters,* vol. 24, pp. 184-185, 1974.

[19]   W. Maes, K. De Meyer, and R. Van Overstraeten, "Impact ionisation in silicon: A review and update," *Solid-State Electronics,* vol. 33, pp. 705-718, 1990.

[20]   C. A. Klein, "Bandgap Dependence and Related Features of Radiation Ionisation Energies in Semiconductors," *Journal of Applied Physics,* vol. 39, pp. 2029-2038, 1968.

[21]   A. R. J. Marshall, P. Vines, P. J. Ker, J. P. R. David, and T. Chee Hing, "Avalanche Multiplication and Excess Noise in InAs Electron Avalanche Photodiodes at 77 K," *Quantum Electronics, IEEE Journal of,* vol. 47, pp. 858-864.

[22]   J. H. Hubbell and S. M. Seltzer, "Tables of x-ray mass attenuation coefficients and mass energy-absorption coefficients 1 keV to 20 MeV for elements Z = 1 to 92 and 48 additional substances of dosimetric interest." vol. http://www.nist.gov/pml/data/xraycoef/index.cfm, 1995.

[23]   S. T. Ulrich, "Half-life and X-ray emission probabilities of ^{55}Fe," *Applied Radiation and Isotopes,* vol. 53, pp. 469-472, 2000.

[24]   G. Bertuccio and A. Pullia, "A method for the determination of the noise parameters in preamplifying systems for semiconductor radiation detectors," *Review of Scientific Instruments,* vol. 64, pp. 3294-3298, 1993.

[25]   G. Bertuccio, A. Pullia, and G. De Geronimo, "Criteria of choice of the front-end transistor for low-noise preamplification of detector signals at sub-microsecond shaping times for X- and γ-ray spectroscopy," *Nuclear Instruments and Methods in Physics Research Section A: Accelerators, Spectrometers, Detectors and Associated Equipment,* vol. 380, pp. 301-307, 1996.

[26]   A. Brunetti, M. Sanchez del Rio, B. Golosio, A. Simionovici, and A. Somogyi, "A library for X-ray matter interaction cross sections for X-ray fluorescence applications," *Spectrochimica Acta Part B: Atomic Spectroscopy,* vol. 59, pp. 1725-1731, 2004.

[27]   M. O. Krause and J. H. Oliver, "Natural widths of atomic K and L levels, K alpha X-ray lines and several KLL Auger lines," *Journal of Physical and Chemical Reference Data,* vol. 8, pp. 329-338, 1979.

Chapter 6 GaAs / Al$_{0.8}$Ga$_{0.2}$As Separate absorption and multiplication (SAM) APD for soft X-ray detection

6.1 Introduction

X-ray detectors for operations in harsh thermal environments, require detectors that operate without cryogenic cooling for higher stability and lower operational cost. Many wide band gap compound semiconductors have been investigated for room (and higher) temperature operation. McGregor and Hermon have summarised the materials investigated for room temperature operation [1]. A more recent review of compound semiconductors for room temperature radiation detection has been presented by Sellin [2]. Some of the best results have been achieved with GaAs and SiC coupled with ultra low noise electronics. Bertuccio *et al.* have shown SiC X-ray detectors operating in a wide temperature range [3]. The pixel detector showed sub keV resolution with equivalent noise energy of 797 eV even at temperature as high as 100 °C, when irradiated by a ^{241}Am gamma ray source. This was largely attributed to the extremely low leakage currents and low noise electronics. Most of the reported III-V X-ray detectors are based on GaAs. One of the earlier reports using an n type GaAs grown by liquid phase epitaxy showed good response to both gamma rays and alpha particles. A FWHM of 694 eV was obtained for 59.5 keV photons with the detector cooled to 130 K which increased to 2.5 keV at room temperature [4]. This allowed for a good estimate of the fano factor and ε value for GaAs, which were reported to be 0.18 and 4.27 eV (at room temperature) respectively. More recently with the development in the growth and fabrication techniques coupled by low noise electronics a more accurate estimate of the fano factor and ε has been obtained. A GaAs pixel detector with an active thickness

of 5 µm has been shown to detect X-rays from a ^{55}Fe source with a good resolution of 407 eV when cooled to -30 °C [5]. Bertuccio *et al.* in another piece of work have reported an improved fano factor of 0.124 [6] and a slightly lower ε = 4.21 eV [7]. Owens *et al.* developed GaAs pixel arrays with a pixel size of 200 μm^2 with a FWHM of 266 eV for 5.9 keV X-rays at room temperature [8]. GaAs schottky diodes with a time resolution of 600 ps at 14.4 keV have been developed for high count rate applications. These diodes also showed a modest energy resolution of 1.6 keV for 6 keV X-rays [9].

Other semiconductors investigated include, $Al_{0.8}Ga_{0.2}As$ [10, 11] and diamond [12, 13]. Recently, $Al_{0.8}Ga_{0.2}As$ photodiodes have been tested for soft X-rays performance at higher temperatures [14]. The detectors were shown to have a spectroscopic performance from 0.9 – 2.5 keV for temperatures ranging from −30 to +90 °C.

The results in chapter 4 strongly indicate that X-ray APDs with improvement in signal to noise ratio, without significant degradation in spectral resolution due to the avalanche multiplication process can be designed. In summary, the avalanche gain distribution narrows as the number of carriers generated by X-ray photon absorption (dependent on the incident photon energy and the absorbing material) increase. The results are shown to be in good agreement with the analytical studies by McIntyre [15]. Materials with dissimilar ionisation coefficients also produce a better energy resolution. Minimum spread in the energy spectra was achieved when the avalanche process is dominated by pure injection of the carrier with higher ionisation probability, such as in a SAM APD. Yet there has only been a single report of a GaAs/AlGaAs SAM APD [16] demonstrating its X-ray spectroscopic capability. The APD comprised of an undepleted GaAs absorption region and an AlGaAs multiplication layer. Spectra were obtained from a ^{241}Am source irradiated on the device. An energy resolution of 1.95 keV and an improvement to 0.9 keV were achieved at unity gain and a gain of 4.1 respectively, for 13.9 keV X-rays.

In this chapter, results from the characterisation of a GaAs/$Al_{0.8}Ga_{0.2}As$ SAM APD for soft X-ray detection at room temperature are presented. The effects of avalanche gain on the energy resolution of the detected X-ray peak and the minimum detectable energy were experimentally obtained. The spread in avalanche gain was computed using the model presented in chapter 4. An assessment of the electronic noise from the APD and the accompanying preamplifier system was carried out. The avalanche gain model was tested by comparing the simulated and experimentally obtained energy spectra.

6.2 Layer details and C-V characteristics

Layer	Thickness (nm)	Material	Type	Doping (cm^{-3})
Cladding	50	GaAs	p^+	1×10^{19}
	200	GaAs	p^+	2×10^{18}
Absorber	400	GaAs	i	-
Charge sheet	50	GaAs	p^-	2.6×10^{17}
	80	$Al_{0.8}Ga_{0.2}As$	p^-	2.6×10^{17}
Avalanche	100	$Al_{0.8}Ga_{0.2}As$	i	-
Cladding	100	$Al_{0.8}Ga_{0.2}As$	n^+	2×10^{18}
Buffer	200	GaAs	n^+	2×10^{18}
Substrate		GaAs	n^+	

Table 6.1 Details of the GaAs/$Al_{0.8}Ga_{0.2}As$ SAM APD structure

The GaAs/$Al_{0.8}Ga_{0.2}As$ SAM APD structure grown on an n^+ GaAs substrate by Molecular Beam Epitaxy (MBE) is shown in Table 6.1. It consists of a 0.4 µm GaAs absorption region and 0.1 µm $Al_{0.8}Ga_{0.2}As$ multiplication region. The GaAs/$Al_{0.8}Ga_{0.2}As$ system was chosen to obtain good avalanche characteristics as well as high absorption efficiency. GaAs has a higher absorption coefficient compared to $Al_{0.8}Ga_{0.2}As$, leading to better detection efficiency for the same absorber thickness. The lower ε of GaAs leads to a better spectral resolution due a smaller fano spread as compared to $Al_{0.8}Ga_{0.2}As$. Figure 6.1 shows a comparison of the attenuation length of GaAs with Si and $Al_{0.8}Ga_{0.2}As$. The thin

Al$_{0.8}$Ga$_{0.2}$As multiplication region was chosen because of its lower avalanche statistics noise due to increased dead space effects [17]. The two regions are separated by a p-doped GaAs region to reduce the strength of the electric field in the absorption region, which allows for the drifting of the carriers generated into the multiplication region, while restricting avalanche multiplication. The p$^+$ and n$^+$ cladding regions of the diode were doped with Be and Si respectively to a concentration of 2×10^{18} cm^{-3}.
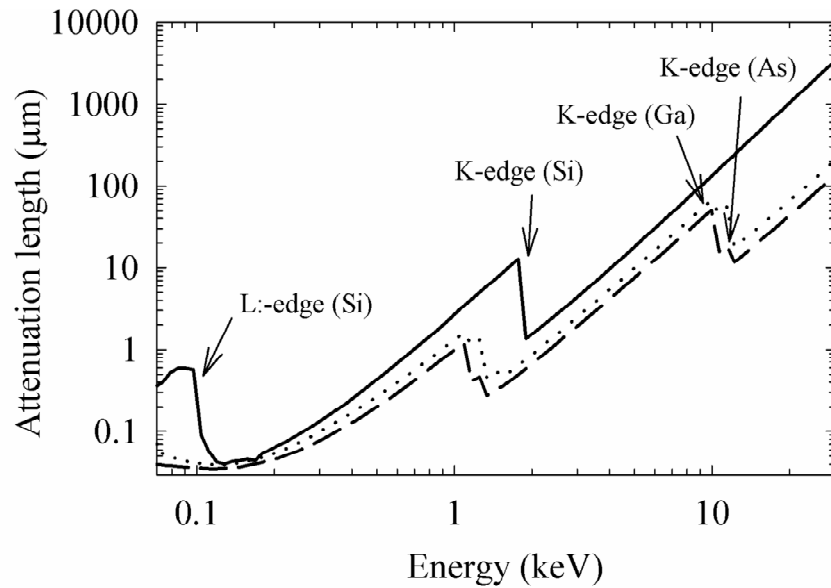
Figure 6.1 Comparison of attenuation lengths of GaAs (dashed), Al$_{0.8}$Ga$_{0.2}$As (dotted) and Si (solid) for X-rays up to 30 keV. The discontinuities in the graph are due to the absorption edges of the constituent atoms. There is a significant improvement in the detection efficiency immediately after the absorption edge.

Circular mesa diodes of diameters ranging from 50-400 μm were processed by using photolithographic techniques (fabricated by Yu Ling Goh at the National III-V centre, Sheffield). Au/Zn/Au annular contacts were deposited on the top p$^+$ layer of the diode. The n$^+$ contacts were formed by using In/Ge/Au. The mesa diodes were isolated by wet chemical etching using a 1:1:1 mixture of hydrogen bromide, acetic acid and potassium dichromate. Diodes with 200 μm diameter were bonded using gold wires to a TO-5 package for X-ray measurements.
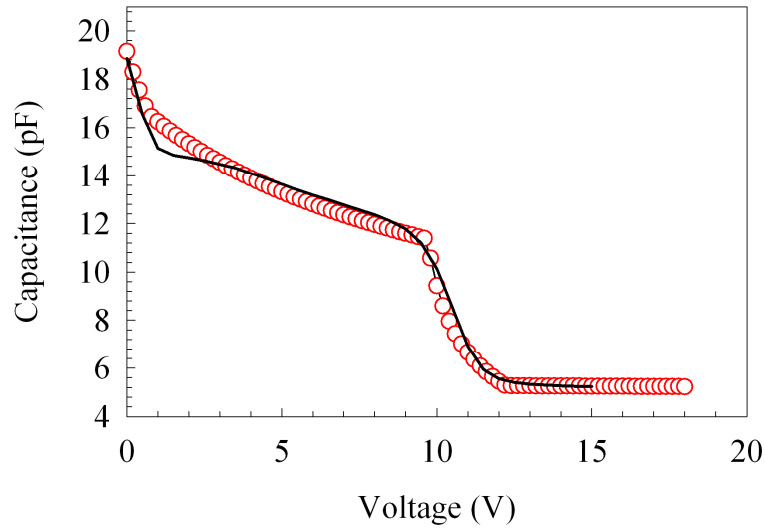
Figure 6.2 Measured (line) and fitted (symbols) results of a 200 μm diameter device.

C-V measurements were carried out on devices of different diameters. The capacitance scaled with area for the devices measured. The i-region thickness, w, and its background doping were estimated by modelling of the C-V characteristics using the electrostatic model described in section 3.2.2. The C-V characteristic of a 200 μm diameter along with the fitted curve is shown in figure 6.2. The intrinsic doping concentration of the absorption and the charge multiplication region are obtained from the C-V fitting. The thickness of absorption region and the multiplication region are estimated to be 0.43 and 0.22 μm respectively. These values are used as input parameters when modelling the X-ray response of the SAM APD.

6.3 X-ray Response

6.3.1 Pulse height spectra

The TO-5 package was placed in a metal Dewar. A 185 MBq ^{55}Fe radioisotope source emitting characteristic Mn K$_\alpha$ and K$_\beta$ peaks at 5.9 and 6.49 keV respectively was irradiated on the APD placed 0.5 cm away. The APD was reverse biased using a Keithley 2400 SMU through a charge sensitive

preamplifier (Amptek A250CF). X-ray spectra were then obtained using the process described in chapter 3. The signal from the preamplifier was shaped using a semi-Gaussian shaping amplifier (Ortec 570), with a shaping time of 2 μs. The amplified pulse was then digitised and pulse height distribution was obtained by connecting the amplifier output to a multichannel analyser (MCA) interfaced to a computer. The spectra were collected for a range of bias voltages at room temperature.
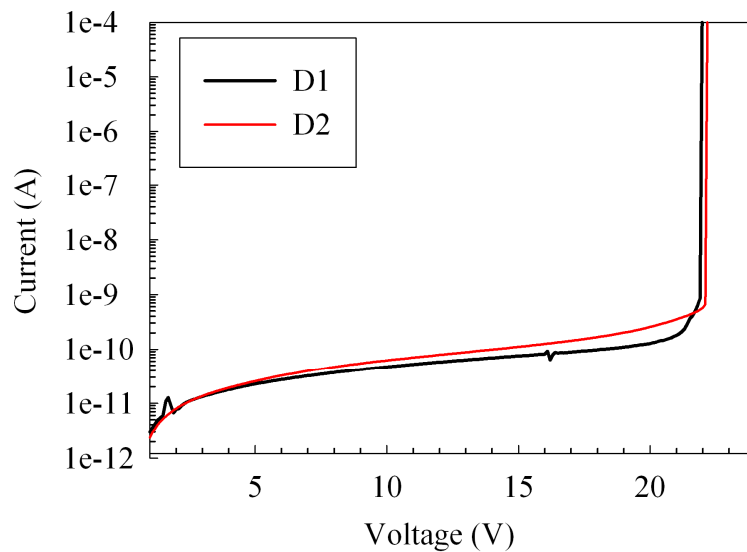
Figure 6.3 Reverse I-V characteristics of 200 μm diameter diodes.

The dark reverse I-V characteristics of two diodes D1 and D2 used in the measurements are shows in figure 6.3. The dark current increases rapidly above 21 V due to avalanche multiplication of current, resulting in a sharp breakdown.

Pulse height spectra obtained from the ^{55}Fe isotope irradiated on D2 with increasing reverse bias is shown in figure 6.4. The 5.9 keV X-ray peak shifts away from the electronic noise floor as the gain increases, thus improving the signal to noise ratio of the detection system. The maximum useful gain before breakdown is dependent on the increasing noise due to the device leakage current. The bias resistor value used is large (330 MΩ), in order to reduce the noise in the system. At higher bias, the dark current increases, resulting in an appreciable drop across the bias resistor, hence the applied voltage values were

appropriately corrected to include this. Since most of the photons absorbed are in the low field absorption region of the APD, pure injection of electrons predominantly accounted for the main detected peak. As the reverse bias increases, a distinct secondary peak at the lower channel numbers of the MCA is seen. This has been analysed later on in the chapter using the RPL model.
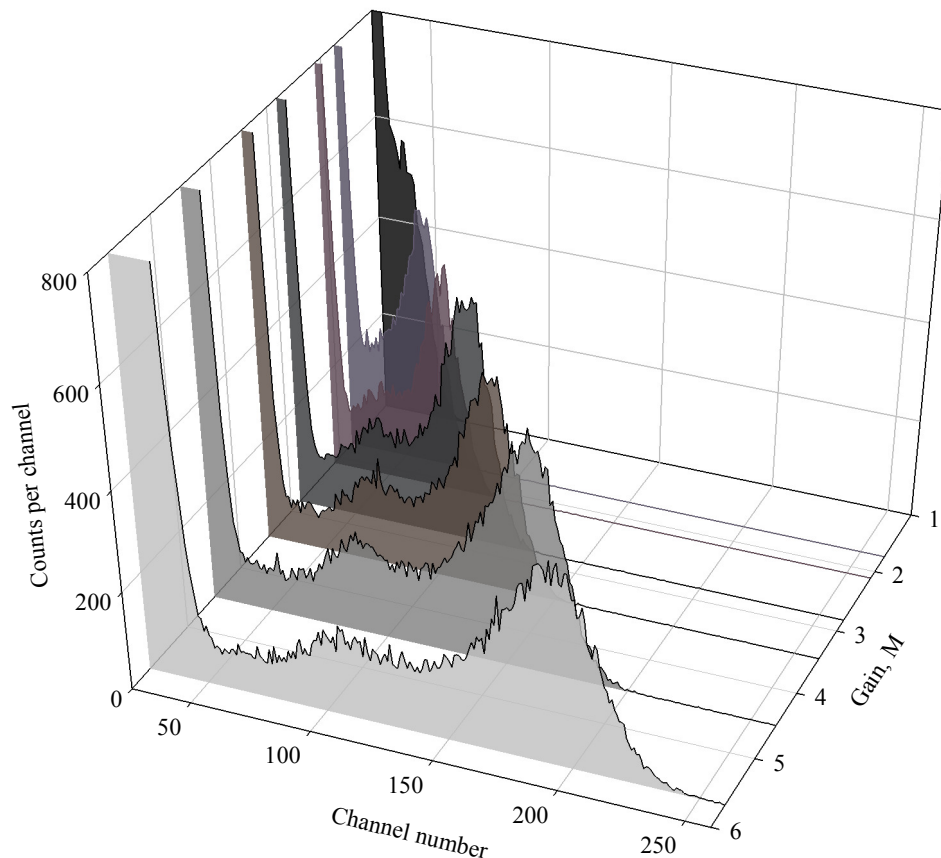
Figure 6.4 ^{55}Fe pulse height spectra obtained from D1 as function of avalanche gain, M.

Effective avalanche multiplication factors were obtained by normalising the peak channel number for each bias to its unity gain peak channel number. The unity gain peak was set at 9 V as there was no appreciable change in its channel number after the punch through voltage (~10 V). The long minority carrier diffusion length in GaAs [18] ensures that the carriers generated in the undepleted absorber before punch through, reach the high field region. The MCA was also calibrated with zero-offset such that channel number zero

represents the actual zero of the detection system. Figure 6.5 shows the mean gain values obtained for D1 and D2.
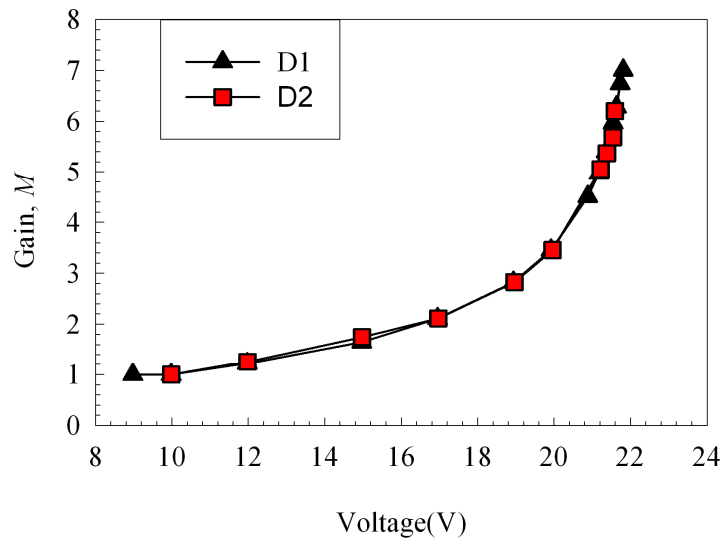
Figure 6.5 Effective avalanche multiplication factors deduced from X-ray measurements (lines are for visualisation purposes).

6.3.2 Energy resolution

The energy resolution of the APD at different gain values was compared by determining the FWHM of the detected X-ray peak. Accurate Gaussian curves were fitted to the experimentally obtained 5.9 keV energy peak. The calibration in terms of energy was obtained by considering the electronic noise peak and the detected X-ray peak as reference. Figure 6.6 shows the FWHM as function of increasing bias. The FWHM obtained from a pulser fed simultaneously through the input of the preamplifier is also shown. The pulser is used for noise evaluation and calibration purposes. Hence the electronic noise measured includes the contribution from the APD leakage current, the preamplifier and the post amplifier and also includes stray capacitances between the diode and preamplifier input.
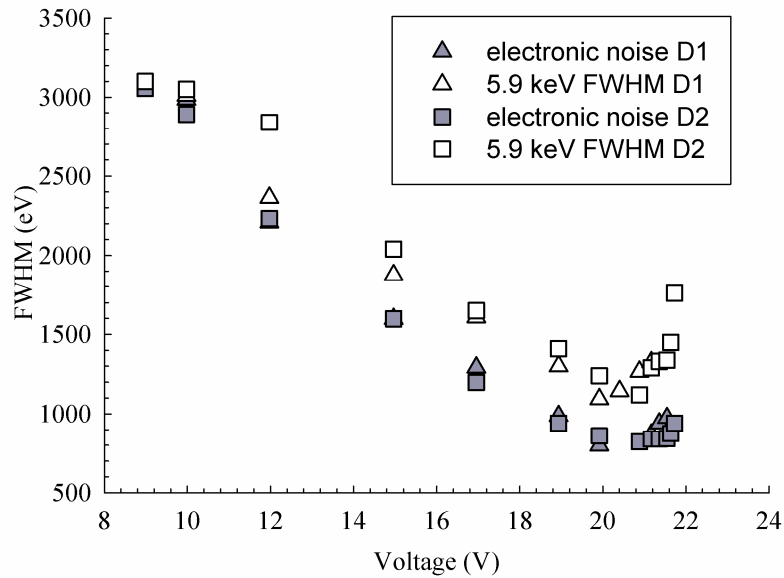
Figure 6.6 Noise measured from a pulser compared with experimental FWHM obtained from ^{55}Fe isotope from D1 and D2.
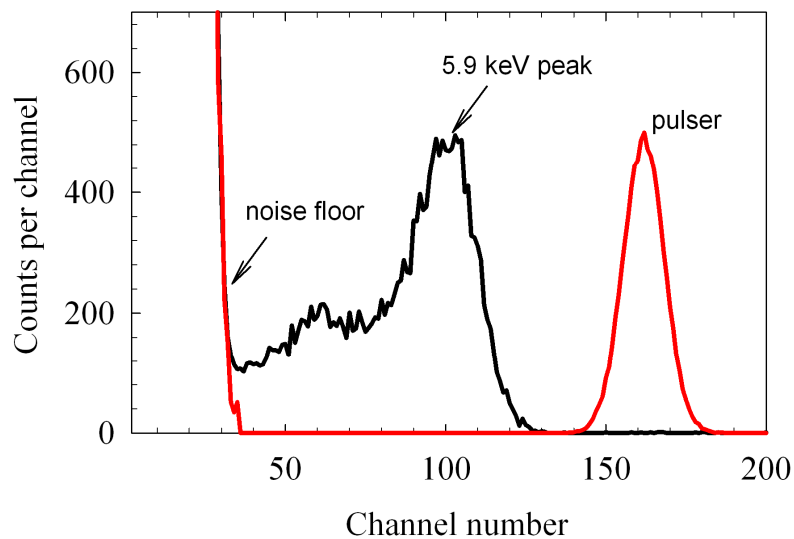
Figure 6.7 Comparison of pulser and X-ray energy peaks at 19 V for D2.

An example of an X-ray spectrum with the test pulser obtained from D2 biased at 19 V is shown in figure 6.7. The FWHM of the 5.9 keV energy peak drops as the gain increases for both D1 and D2, largely due to a reduction in the series white noise of the system. At higher gains the FWHM increases due to increasing leakage current of the detectors, contributing to the increase in the

parallel white noise. The pulser peaks shows excessive tailing effect when the device was biased close to its breakdown voltage possibly indicating non systematic dark current noise from the APD. The results have been presented in figure 2.7. The disparity in the FWHM value between D1 and D2 is due to the difference in their dark current characteristics and breakdown voltage.

The optimum operating voltage for an X-ray APD can be obtained from the FWHM measurements. Best FWHM values of 1.08 keV at 20 V for D1 and 1.12 keV at 20.8 V for D2 have been obtained. The APD provides a significant improvement in the energy resolving capability of the system, in the soft X-ray energy range, for room temperature detection.
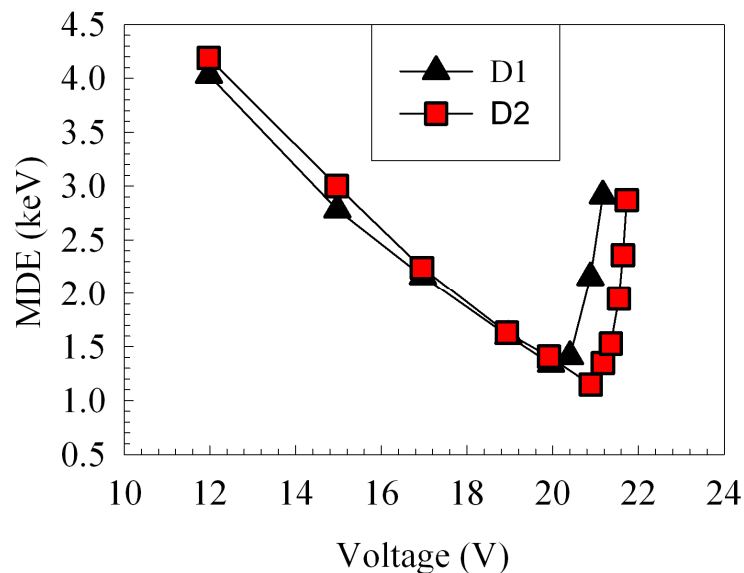
Figure 6.8 Variation of the low energy threshold with increasing reverse bias.

Another important parameter for detection in this range is the low energy threshold or the MDE of the APD. The MDE is defined as the lowest energy, which upon interaction, produces counts above the electronic noise floor of the system. The MDE for D1 and D2 was determined using the spectrum obtained from the pulser measurements at each bias voltage. The MDE characteristics as a function of increasing bias voltage are shown in figure 6.8. The MDE is largely determined by the noise contribution of the preamplifier system and the leakage current of the APD. At higher gain the MDE will also be dependent on the

avalanche statistics due to the stochastic nature of the multiplication process. As seen in figure 6.8, the MDE reduces rapidly from ~4 keV at 12 V to ~1.1 keV at 21 V. Above that voltage, as the diodes approach breakdown, the increasing dark current exacerbates the MDE due to increasing tailing effects in the electronic noise peak in the pulse height spectra.

The results presented in this section show that the avalanche gain significantly improves the energy resolution and the signal to noise ratio of the detection system. The increasing leakage current compromises any further improvement at higher bias. Optimised fabrication techniques can help reduce the dark current in the system. The reduction in the noise from the preamplifier and stray capacitances from the APD packaging and cabling is also needed to achieve further improvements in the spectral resolution.

6.4 Noise Analysis

The fano limited energy resolution for the energy peak is given by $2.36\sqrt{fE\varepsilon}$ [19], where f is measured to be $= 0.12$ for GaAs [6], E is the incident photon energy (5.9 keV) and the pair creation energy ε of 4.21eV is used for GaAs. An $E_F = 129$ eV due to the fano limit is obtained. This is significantly smaller than the FWHM obtained experimentally. The noise sources that lead to the spread in energy resolution are quantified in this section and subsequently used to reproduce the experimental spectrum.

6.4.1 Electronic noise

The electronic noise contribution is mainly divided into the parallel white noise (PWN) and series white noise (SWN) contribution [20]. The PWN includes the shot noise from the leakage current of detector and gate leakage current of input JFET. It also includes the thermal noise generated by the preamplifier feedback resistor. Since the PWN is proportional to the shaping time constant a small shaping time of 2 μs was used. The SWN includes the

preamplifier noise voltage. The SWN is also dependent on the capacitance of the detector, the input JFET and stray capacitance from cabling and device packaging. The SWN is inversely proportional to the shaping time and hence an important factor in these measured values.

The measured and the calculated FWHM of equivalent noise charge (ENC) (expressed in terms of energy (eV)) are calculated as shown in figure 6.9 for diode D1. The various noise sources contributing to the total noise in the system are also shown. The contribution from the PWN to the noise spectral density, S_p, is given by equation 2.31 as,

$$S_0 = 2q(I_{ds} + M^2FI_{db}) + \frac{4kT}{R_p} \quad , \tag{6.1}$$

Since the FET used in the A250CF is cooled to -50°C, the effect of the gate leakage current on the total noise is negligible and hence is neglected. The SWN stems from the thermal noise from the input FET of the preamplifier, e_n and the capacitance of the APD, C_D. This contribution is inversely proportional to shaping time. Neglecting the frequency dependent noise components (as it is usually much smaller than the noise sources considered here) the SWN noise spectral density can be given as

$$S_2 = e_n^2 C_T^2 + 4kTR_S C_D^2 , \quad , \tag{6.2}$$

where R_S is the series resistance of the diode (determined from the forward dark I-V characteristics of the diode). C_T is the total capacitance, which includes the detector, preamplifier feedback capacitor, C_f and stray capacitances. The total stray capacitance from the cabling, T0-5 package and electrical connections inside the metal Dewar to the preamplifier input was measured to be 39 pF. The parameters used in the above equations are summarised in Table 6.2. The total electronic noise expressed in terms of its ENC is obtained from equation 2.33 in chapter 2 for a single differentiating and integrating stage shaping

amplifier. The total ENC contribution to the energy peak is given in terms of the FWHM from equation 2.33.
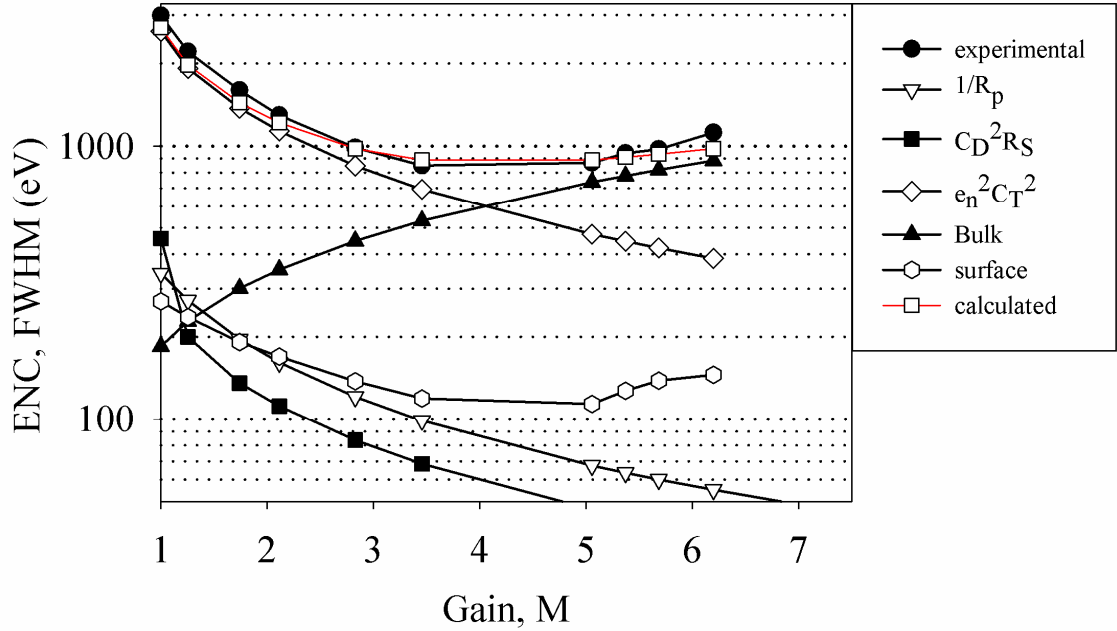
Figure 6.9 ENC (FWHM) as a function of avalanche gain M (lines are for visualisation purposes).

Parameter	Symbol	Value
Preamplifier noise voltage	e_n	1.08 nV/$\sqrt{Hz}$
Capacitance of FET	C_{GS}	8 pF
APD series resistance	R_S	70 Ω
APD capacitance	C_D	6 pF
Shaping time constant	τ	2 μs
Preamplifier feedback capacitance	C_f	0.5 pF
Total Capacitance	C_T	53 pF

Table 6.2 Parameters used to model the electronic noise.

For multiplication factors below 4, the electronic noise is primarily dominated by the SWN contribution. The SWN decreases as the gain increases. An increase in gain is also accompanied by increased diode leakage current. For low gain operation, a low noise preamplifier would significantly improve the performance of the system. The PWN contribution increases above a gain of 5. Operating the APD at high gain will reduce the SWN such that the energy resolution performance largely depends on the leakage current of the APD. The measured leakage current was assumed to be subjected to full shot noise; this produced a good fit to the total measured ENC at higher gain. The APD leakage current at higher gains can be possibly reduced by cooling the APD. This would not be a feasible option for operation in harsh environments.

6.4.2 Avalanche statistics

To calculate the total energy resolution, the noise due to avalanche statistics has to account for, in addition to the electronic noise and the noise from EHP creation statistics. The RPL model presented in chapter 4 is used to compute the spread in energy resolution due to avalanche statistics. The material parameters used for the carrier generation profile along the avalanche region are listed in Table 6.3. The linear absorption coefficients are obtained from their mass absorption coefficients after multiplying with their respective material densities [21]. The impact ionisation coefficients are computed from parameterised equations given in [22]. These coefficients have been independently measured using a series of Al$_{0.8}$Ga$_{0.2}$As p$^+$in$^+$ diodes covering a wide range of electric fields. The parameterised equations for α and β for the electric field, ξ, in the range from 328 to 1110 kVcm^{-1} are given by

$$\alpha(\xi) = 3.18 \times 10^5 \, exp\left[-\left(\frac{1.04 \times 10^6}{|\xi|}\right)^{1.67}\right] cm^{-1}, \qquad (6.3)$$

$$\beta(\xi) = 3.55 \times 10^5 \, exp\left[-\left(\frac{1.12 \times 10^6}{|\xi|}\right)^{1.85}\right] cm^{-1}, \qquad (6.4)$$

	ε	Absorption coefficient @ 5.9 keV (cm^{-1})	Absorption coefficient @ 6.49 keV (cm^{-1})
GaAs	4.21	833.7	640.5
Al$_{0.8}$Ga$_{0.2}$As	5.25	638.8	490.9

Table 6.3 Material parameters used for modelling of the SAMAPD

The position of interaction of each photon was calculated using the parameters in Table 6.3. The value of ε was used to obtain the number of EHPs created per photon interaction. The EHPs were assumed to be created at the point of interaction. These parameters were used as input to the RPL model to calculate the gain of each photon independently. An emission probability ratio of $P_{K\beta}$ / P_{Ka} = 0.138 for the ^{55}Fe source was used [23]. Avalanche gain distribution across the APD was then generated. The 'dead-space' effect has been shown to improve the energy resolution of X-ray APDs. Dead space is a significant factor in thin avalanche regions, as in the one used here, and hence has to be considered. Ionisation threshold energy equal to the average of the bandgap energy of 2.23 eV was assumed for electrons and holes [24]. This was used to successfully model the experimental multiplication and noise data for Al$_{0.8}$Ga$_{0.2}$As in [17].

For simplicity the simulations assumed complete charge collection for every X-ray photon absorbed within all epitaxially grown layers (i.e. layers including and above the n$^+$ Al$_{0.8}$Ga$_{0.2}$As layer), although experimental results indicate incomplete charge collection. The counts of the simulated spectrum were normalised to those of the experimental spectrum for easy comparison.
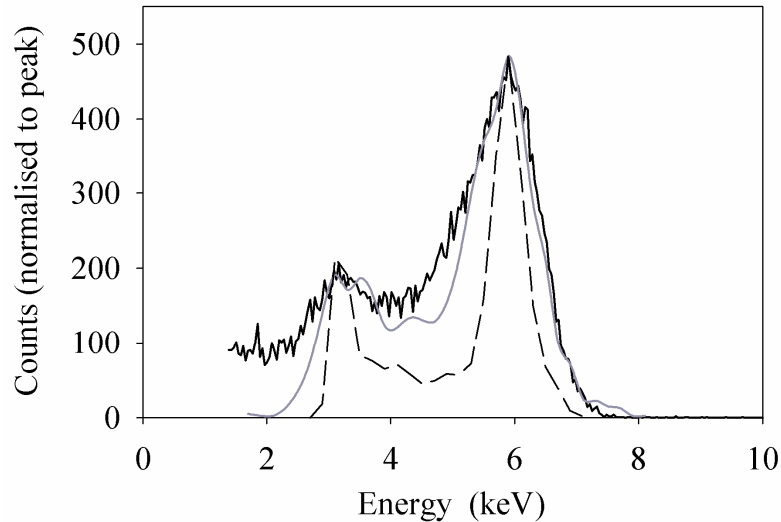
Figure 6.10 Comparison of simulated (grey line) and experimental (black line) spectra for D1 at $M = 4.5$. The avalanche gain limited spectra is also shown (dashed).

The simulated gain spectrum is shown in figure 6.10. The avalanche limited spectrum is narrower than the total measured spectrum. The total electronic noise from the diode preamplifier system and the fano limit were added in quadrature and used as a fitting parameter to simulate the total spread in energy resolution. The simulated spectrum is in agreement with experimental results. The poor fitting to the low energy tail indicates the presence of incomplete charge collection, which also contributes to the increasing FWHM. The additional (smaller) peak at ~3 keV in the experimental spectrum is also present in the simulated spectrum. This originated from avalanche multiplication initiated by holes generated by photon absorption in the n^+ $Al_{0.8}Ga_{0.2}As$ cladding layer, and was confirmed by simulations that excluded absorption in that layer. As the reverse bias increases, the separation between the two peaks is seen to increase (figure 6.4), because of the increasing difference between the pure electron and pure hole multiplication factors. Since the measured gain are limited to low values, these factors will eventually converge at higher electric fields leading to a single broad peak.

6.5 Summary

GaAs/$Al_{0.8}Ga_{0.2}As$ SAM APDs have been implemented for soft X-ray detection. Measurements carried out using a ^{55}Fe radioisotope source show that avalanche gain substantially improves the signal to noise ratio and spectral resolution of the detected 5.9 keV energy peak. Further improvements in energy resolution can be obtained by reducing the noise from accompanying electronics and stray capacitances. Additional improvement is also possible by reducing the leakage currents through optimised fabrication, perhaps with device surface passivation.

At room temperature the APD exhibited a capacitance of ~6 pF above 12 V, as shown in figure 6.2. This value is consistent with the relatively narrow depletion region in the design (~0.7 μm), although the capacitance is much larger than those typically found in X-ray APDs, where the depletion region width is at least tens of μm. A more appropriate APD design with a thicker absorption region is necessary to improve detection efficiency particularly at higher energies.

The energy spectrum has been successfully modelled while taking into account the noise due to avalanche statistics and the electronics. The model also predicts the occurrence of undesirable secondary peaks in the spectra that can be mitigated by optimizing the APD design.

6.6 References

[1]   D. S. McGregor and H. Hermon, "Room-temperature compound semiconductor radiation detectors," *Nuclear Instruments and Methods in Physics Research Section A: Accelerators, Spectrometers, Detectors and Associated Equipment,* vol. 395, pp. 101-124, 1997.

[2]   P. J. Sellin, "Recent advances in compound semiconductor radiation detectors," *Nuclear Instruments and Methods in Physics Research Section A: Accelerators, Spectrometers, Detectors and Associated Equipment,* vol. 513, pp. 332-339, 2003.

[3]   G. Bertuccio, R. Casiraghi, A. Cetronio, C. Lanzieri, and F. Nava, "Silicon carbide for high resolution X-ray detectors operating up to 100°C," *Nuclear Instruments and Methods in Physics Research Section A: Accelerators, Spectrometers, Detectors and Associated Equipment,* vol. 522, pp. 413-419, 2004.

[4]   J. E. Eberhardt, R. D. Ryan, and A. J. Tavendale, "Evaluation of epitaxial n-GaAs for nuclear radiation detection," *Nuclear Instruments and Methods,* vol. 94, pp. 463-476, 1971.

[5]   G. Bertuccio, A. Pullia, J. Lauter, A. Forster, and H. Luth, "Pixel X-ray detectors in epitaxial gallium arsenide with high-energy resolution capabilities (Fano factor experimental determination)," *Nuclear Science, IEEE Transactions on,* vol. 44, pp. 1-5, 1997.

[6]   G. Bertuccio, R. Casiraghi, D. Maiocchi, A. Owens, M. Bavdaz, A. Peacock, H. Andersson, and S. Nenonen, "Noise analysis of gallium arsenide pixel X-ray detectors coupled to ultra-low noise electronics," *Nuclear Science, IEEE Transactions on,* vol. 50, pp. 723-728, 2003.

[7]   G. Bertuccio and D. Maiocchi, "Electron-hole pair generation energy in gallium arsenide by x and gamma photons," *Journal of Applied Physics,* vol. 92, pp. 1248-1255, 2002.

[8]   A. Owens, M. Bavdaz, A. Peacock, A. Poelaert, H. Andersson, S. Nenonen, L. Troger, and G. Bertuccio, "Hard X-ray spectroscopy using small format GaAs arrays," *Nuclear Instruments and Methods in Physics Research Section A: Accelerators, Spectrometers, Detectors and Associated Equipment,* vol. 466, pp. 168-173, 2001.

[9]   C. Rente, J. Lauter, R. Engels, R. Reinartz, R. Apetz, and H. Luth, "Fast X-ray detection systems based on GaAs diodes grown by LPE," in *Nuclear Science Symposium, 1996. Conference Record., 1996 IEEE*, 1996, pp. 376-379 vol.1.

[10]   J. E. Lees, D. J. Bassford, J. S. Ng, C. H. Tan, and J. P. R. David, "AlGaAs diodes for X-ray spectroscopy," *Nuclear Instruments and Methods in Physics Research Section A: Accelerators, Spectrometers, Detectors and Associated Equipment,* vol. 594, pp. 202-205, 2008.

[11]   J. E. Lees, A. M. Barnett, D. J. Bassford, J. S. N. a. C. H. Tan, N. Babazadeh, R. B. Gomes, P. Vines, J. P. R. David, R. D. McKeag, and D. Boe, "Development of high temperature AlGaAs soft X-ray photon counting detectors," *Journal of Instrumentation,* vol. 6, p. C12007.

[12]   H, Kagan, "Diamond radiation detectors may be forever!," *Nuclear Instruments and Methods in Physics Research Section A: Accelerators, Spectrometers, Detectors and Associated Equipment,* vol. 546, pp. 222-227, 2005.

[13]   G. Conte, M. Girolami, S. Salvatori, and V. Ralchenko, "X-ray diamond detectors with energy resolution," *Applied Physics Letters,* vol. 91, pp. 183515-3, 2007.

[14]   A. M. Barnett, D. J. Bassford, J. E. Lees, J. S. Ng, C. H. Tan, and J. P. R. David, "Temperature dependence of AlGaAs soft X-ray detectors," *Nuclear Instruments and Methods in Physics Research Section A: Accelerators, Spectrometers, Detectors and Associated Equipment,* vol. 621, pp. 453-455.

[15]   R. J. McIntyre, "The distribution of gains in uniformly multiplying avalanche photodiodes: Theory," *Electron Devices, IEEE Transactions on,* vol. 19, pp. 703-713, 1972.

[16]   J. Lauter, D. Protic, A. Forster, and H. Luth, "AlGaAs/GaAs SAM-avalanche photodiode: An X-ray detector for low energy photons," *Nuclear Instruments and Methods in Physics Research Section A: Accelerators, Spectrometers, Detectors and Associated Equipment,* vol. 356, pp. 324-329, 1995.

[17]   B. K. Ng, J. P. R. David, S. A. Plimmer, G. J. Rees, R. C. Tozer, M. Hopkinson, and G. Hill, "Avalanche multiplication characteristics of $Al_{0.8}Ga_{0.2}As$ diodes," *Electron Devices, IEEE Transactions on,* vol. 48, pp. 2198-2204, 2001.

[18]   S. Adachi, "Handbook on Physical Properties of Semiconductors ". vol. 2: III-V Compound Semiconductors: Kluwer Academic, Boston, 2004, p. 359.

[19]   G. F. Knoll, *Radiation detection and measurement*: John Wiley & Sons, Inc, 2002.

[20]   G. Bertuccio, A. Pullia, and G. De Geronimo, "Criteria of choice of the front-end transistor for low-noise preamplification of detector signals at sub-microsecond shaping times for X- and γ-ray spectroscopy," *Nuclear Instruments and Methods in Physics Research Section A: Accelerators, Spectrometers, Detectors and Associated Equipment,* vol. 380, pp. 301-307, 1996.

[21]   J. H. Hubbell and S. M. Seltzer, "Tables of x-ray mass attenuation coefficients and mass energy-absorption coefficients 1 keV to 20 MeV for elements Z = 1 to 92 and 48 additional substances of dosimetric interest. ," vol. http://www.nist.gov/pml/data/xraycoef/index.cfm, 1995.

[22]   B. K. Ng, J. P. R. David, S. A. Plimmer, M. Hopkinson, R. C. Tozer, and G. J. Rees, "Impact ionisation coefficients of $Al_{0.8}Ga_{0.2}As$," *Applied Physics Letters,* vol. 77, pp. 4374-4376, 2000.

[23]   S. T. Ulrich, "Half-life and X-ray emission probabilities of ^{55}Fe," *Applied Radiation and Isotopes,* vol. 53, pp. 469-472, 2000.

[24]   J. Allam, "Universal Dependence of Avalanche Breakdown on Bandstructure: Choosing Materials for High-Power Devices," *Japanese Journal of Applied Physics,* vol. 36, 1997.

Chapter 7 Conclusions

7.1 Summary

A generalised model that quantifies the spread in the energy resolution of the detected energy peak by X-ray APDs has been presented. The model has shown that the avalanche gain distribution PDFs created by high energy photons are considerably different from that obtained from EHPs created by light absorption. The PDF changes from an exponential for a single EHP injection to a pseudo Gaussian as the number of EHPs injected increase. For EHPs greater than 1000, the distribution is seen to converge to a Gaussian in accordance with the central limit theorem. Hence for very large number of EHPs approaching infinity, the distribution is expected to converge to a delta like function. The incorporation of conventionally obtained excess noise factors from light measurements, to determine the avalanche gain limited energy resolution of the APD is thus inaccurate and can lead to an overestimation of the resolution spread.

The FWHM of the PDF is shown to narrow with increasing number of EHPs. The distribution also narrows with the increasing difference between the electron and hole ionisation coefficients, consistent with analytical studies by McIntyre [1, 2]. X-rays are of considerable high energy and hence can be strongly absorbed throughout the active region of the APD. The PDF of the gain distribution is shown to be heavily dependent on the position of interaction of the photon throughout the APD. The gain distribution is independent of path length of the photon through the absorber with equal ionisation coefficients. For disparate ionisation coefficients, the PDF changes with absorption position and hence can cause degradation in the total spectral resolution. APDs can thus be optimised for their best avalanche statistics performance using the model.

The well known dead space effect observed in wide range of semiconductor APDs reduces the avalanche excess noise. Dead space effects are incorporated in the model to study its effects on the PDF. Significant dead space, achieved using APDs with thin avalanche region width and high impact ionisation threshold energies, is shown to considerably reduce the FWHM of the PDF. The effect of dead space on the photon absorption position has also been investigated.

InAs APDs have been investigated for their soft X-ray spectroscopic ability. The APDs were shown to detect the 5.9 keV energy peak from a ^{55}Fe radioisotope source at zero bias with a FWHM of 2.8 keV at 77 K. The energy resolution spread is largely dominated by the voltage noise from the preamplifier. As the reverse bias is increased, the FWHM is seen to drop rapidly and a lowest value of 950 eV at a reverse bias of 10.8 V (corresponding to a gain of 5.3) is obtained. The 5.9 keV energy peak is also seen to shift away from the electronic noise floor, improving the low energy threshold of the spectrometer. Simulations were carried out to model the experimental spectra. The single carrier ionisation characteristic of InAs is shown to exhibit very low spread in energy resolution due to avalanche statistics. More importantly, the intrinsic resolution of the APD is shown to be independent of avalanche gain. This shows the capability of low noise APDs for X-ray detection. A further improvement in energy resolution can possibly be achieved by the reduction in leakage currents introduced during non optimised bonding techniques. Reducing the noise from readout electronics and the stray capacitances between the detector and the preamplifier will reduce the series white noise of the APD. Thicker structures are necessary to detect higher energy X-ray with good efficiency. Increasing the avalanche region also increases the gain obtained at a particular reverse bias and delays the on set of band to band tunnelling due to the reduced electric field across the junction. A ^{241}Am gamma ray source was also used to demonstrate the higher energy response of the detector. An $E_R =$ 18.5 %, was obtained for 13.95 keV photons. The 59.5 keV gamma ray peak was also resolved with an $E_R = 4.5$ % under no external bias.

Finally the spectroscopic performance of a $GaAs/Al_{0.8}Ga_{0.2}As$ SAM APD has been analysed at room temperature. An optimum FWHM of 1.08 keV has been achieved for 5.9 keV X-rays. Electronic noise contribution to the FWHM has been evaluated using a test pulser. The FWHM at gains below 3, is limited by the series white noise of the system. At higher gains the shot noise from the detector increasing leakage current is a major limiting factor. The avalanche gain helps improve the signal to noise performance and the MDE reduces rapidly from ~4 keV at 12 V to ~1.1 keV at 21 V. The pulse height spectra have been modelled using the method presented in chapter 4. A good agreement with experimental data is obtained when the electronic noise and statistics due to energy loss of the photon are accounted for. Spurious secondary peaks arsing due to avalanche gain statistics have also been accounted for by the model. Optimum design for a given energy range can be developed using the model that mitigate any stray peaks in the pulse height spectra.

7.2 Future work

In this section some further comments and suggestions are listed for future work in modelling and experimental characterisation of compound semiconductor APDs for X-ray spectroscopy.

7.2.1 APD modelling

The model presented in the thesis presents an accurate method to predict the avalanche statistics effects on the energy resolution of APDs for soft X-rays. A simple approach that includes the electronic noise and photon energy loss statistics is shown to reproduce the experimental data with sufficient accuracy. In order to have a more complete model of the detector response factors like incomplete charge collection needs to be taken into account.

- For X-rays absorbed in the field free region of the APD the carries generated rely on diffusion to be efficiently collected. This depends on

the diffusion length of the carriers which is a function of temperature and doping density. Since the carriers generated at the interaction point move in an isotropic manner, some of the carriers will recombine while others that reach the edge of the depletion region are collected after charge multiplication. This can lead to a degradation of the spectral resolution and low energy tails in the pulse height spectra.

- A further improvement that could lead to more realistic modelling is the inclusion of the carrier velocity distribution and space charge effects on the avalanche gain distribution PDF.

- In the current model the carriers are assumed to be created at the point of interaction. This is a reasonable assumption for soft X-rays, as the mean free path length of the ejected photoelectron by a photon absorption event is much smaller than the active region thickness. As the incident photon energy increases, the stopping power of the material is reduced and hence the position of the carrier creation can affect the PDF. Some of the energetic photoelectrons can also escape the detector without depositing all their energy. Monte Carlo models like CASINO [3] used in chapter 2 to simulate electron path lengths in semiconductors can be incorporated to include the energy loss statistics.

- The energy loss mechanism is assumed to be photoelectric (the dominant mechanism at low energy X-rays), for modelling of high energy X-rays the Compton Effect has to be taken into consideration.

- During the ejection of a photoelectron the atom is ionised and hence a rearrangement of the electrons takes place resulting in the emission of characteristic X-rays or the ejection of auger electron. Usually the characteristic X-rays are of low energy and reabsorbed close to the point of creation. Some of the characteristic X-rays can escape the

detector resulting in the peaks in the pulse height spectra referred to as X-ray 'escape peaks' which could also be included in the model.

7.2.2 X-ray APD characterisation

The APDs presented in chapters 5 and 6 show the advantages of the avalanche gain mechanism. Although the avalanche process will add to the statistical noise in fano limited systems, an APD can be a good alternative in systems operating above the fano limit to improve the signal to noise ratio without the use of ultra low noise read out electronics.

The first results using an InAs APD has shown sub keV energy resolution for soft X-rays. Further improvements are needed to achieve performance closer to the limit predicted by the fano and avalanche statistics.

- Since the diodes are limited to measurements at low gain values, the series white noise is still a significant contributor to the spread in energy resolution. Having diodes with thicker avalanche region width would allow for operation at much higher gains for a given reverse bias voltage. The modelling indicates that avalanche statistical broadening is almost independent of the avalanche gain due to the single characteristic ionisation behaviour in InAs. Hence operation at higher gain would solely be dependent on the short noise contribution from the leakage current of the detector.

- Since the n^+ region in the n^+ip^+ diodes measured is thin, a sizable number of incident photon are absorbed in the avalanche region worsening the peak to background ratio (also seen in the modelled spectra). This can be mitigated by increasing the thickness of the cladding layers or having a low field drift region before the avalanche region. Since impact ionisation in InAs occurs at low fields, it would be difficult to control the electric field in the drift region of the diode

and hence diffusion from the thick p$^+$ into the i region is a better option.

- The packaged diodes measured in this thesis show a significant increase in leakage current compared to the unpackaged samples. The exact cause of the increase in current has yet to be comprehensively investigated. The optimisation of the packaging process could further aid in improving the APD performance.

The SAM APD shows reasonable spectral performance at room temperature. The improvement in FWHM is limited by the leakage current at higher bias. Due to the small absorption region width the evaluation of these diodes has been limited to the soft X-ray range. Thicker diodes would improve the detection efficiency. Temperature dependent measurements can also be performed on the APDs to access their feasibility for operation in harsher conditions.

7.3 References

[1]   R. J. McIntyre, "Multiplication noise in uniform avalanche diodes," *Electron Devices, IEEE Transactions on*, vol. 13, pp. 164-168, 1966.

[2]   R. J. McIntyre, "The distribution of gains in uniformly multiplying avalanche photodiodes: Theory," *Electron Devices, IEEE Transactions on*, vol. 19, pp. 703-713, 1972.

[3]   P. Hovington, D. Drouin, and R. Gauvin, "CASINO: A new monte carlo code in C language for electron beam interaction —part I: Description of the program," *Scanning*, vol. 19, pp. 1-14, 1997.

Appendix A

The Poisson solver for the fitting in section 3.2.1 is described in this appendix. For a p^+in^+ diode as shown schematically in figure 3.1, N_1, N_2, $-N_3$ are the doping concentrations of the p^+, i and n^+ regions respectively (where the negative sign indicated n type doping).

From the Poissonian equation we get

$$\left(\frac{dE}{dx}\right)_1 = \frac{qN_1}{\varepsilon_s}, \left(\frac{dE}{dx}\right)_2 = \frac{qN_2}{\varepsilon_s} \text{ and } \left(\frac{dE}{dx}\right)_3 = \frac{qN_3}{\varepsilon_s} \tag{1}$$

The electric field at the junction is thus given by

$$E_1 = \frac{qN_1X_1}{\varepsilon_s}, \ E_2 = E_1 + \frac{qN_2X_2}{\varepsilon_s} \text{ and } E_3 = -\frac{qN_3X_3}{\varepsilon_s} \tag{2}$$

Solving for X_3 we get,

$$X_3 = -\frac{(N_1X_1 + N_2X_2)}{N_3} \tag{3}$$

The area under the curve in figure 3.1 gives the total voltage than can be given as

$$V_3 = \frac{1}{2}E_1X_1 + (E_1 + E_2)X_2 + E_2X_3 \tag{4}$$

Substituting the values from equation 2 and 3 into 4 and rearranging we get

$$N_1\left(1 - \frac{N_1}{N_3}\right)X_1^2 + 2N_1\left(X_2 - \frac{N_2X_2}{N_3}\right)X_1 - \frac{(N_2X_2)^2}{N_3} + N_2X_2^2 - \frac{2\varepsilon_s V}{q} = 0 \tag{6}$$

which is a quadratic equation whose roots are given by the formula

$$X_1 = \frac{-b \pm \sqrt{b^2 - 4ac}}{2a}$$

7

where the coefficients a, b and c are given as

$$a = N_1\left(1 - \frac{N_1}{N_3}\right), \quad b = 2N_1\left(X_2 - \frac{N_2 X_2}{N_3}\right) \quad \text{and}$$

$$c = -\frac{(N_2 X_2)^2}{N_3} + N_2 X_2{}^2 - \frac{2\varepsilon_s V}{q}$$

Similarly for a four region diode like a SAM APD we can write the coefficients for the quadratic equation as

$$a = N_1\left(1 - \frac{N_1}{N_4}\right), \quad b = 2N_1\left((X_2 + X_3) - \frac{(N_2 X_2 + N_3 X_3)}{N_4}\right) \quad \text{and}$$

$$c = -\frac{(N_2 X_2 + N_3 X_3)^2}{N_4} + N_2 X_2{}^2 + N_3 X_3{}^2 + 2N_2 X_3 X_2 - \frac{2\varepsilon_s V}{q}$$

A similar approach can be followed to derive the coefficients for the case of a SAM APD with a charge sheet between the absorption and multiplication region, by following a five region model.

Appendix B

The code used to generate random numbers that are normally distributed has been achieved using the Box-Muller approach in polar form. This has been used to generate the electronic noise with desired mean and standard deviation to simulate the pulse height spectrum. The code written in C is shown below.

The process is started off by generating two uniformly distributed random numbers between 0 and 1. The transformation is then used to generate random numbers with normal distribution with a mean of 0 and a standard deviation of 1.

```c
#include <limits.h>
#include <stdio.h>
#include <math.h>
#include <stdlib.h>
#include <time.h>

unsigned time_seed()
{
time_t now = time ( 0 );
unsigned char *p = (unsigned char *)&now;
unsigned seed = 0;
size_t s;
for ( s = 0; s < sizeof now; s++ )
seed = seed * ( UCHAR_MAX + 2U ) + p[s];
return seed;
}

int main(void)
{
    srand ( time_seed() );
```

```c
    float x1, x2, w, y1, y2;
    double r,r1;
    int i;
    FILE *f;
    f = fopen("histogram.txt","w");     // file to store the Gaussian random
numbers
 for (i=0;i<100000;i++)
 {
        do    {
                r=(double)  rand()  /  (RAND_MAX);  //  random  number
generator for x1
                x1 = 2.0 * r - 1.0;
                r1=(double)  rand()  /  (RAND_MAX);    //  random  number
generator for x2
                x2 = 2.0 * r1 - 1.0;
                w = x1 * x1 + x2 * x2;
                } while ( w >= 1.0 );

        w = sqrt( (-2.0 * log( w ) ) / w );
        y1 = x1 * w;
        y2 = x2 * w;
fprintf(f,"%f\n",y1);
}
fclose(f);
system("PAUSE");
return 0;
}
```

Appendix C

In this appendix the basic steps to carry out the pulse height measurements are outlined for future reference. For details on the various modules used in the setup refer to chapter 3.

- The device bonded to TO-5 headers is placed on the copper cold finger in the metal Dewar for low temperature measurements and sufficient shielding of the X-rays from the user. After securely placing the X-ray source above the detector the following steps need to be performed (for low temperature measurements only).

- A custom pump-out valve (VOM-1) operator made by Judson Technologies is used to pump the dewar following the steps below
  - ➢ Remove the phenolic valve cap from the dewar.
  - ➢ Install and tighten the operator on the gland seal nut.
  - ➢ Screw in the valve operator stem into the insert, then the vacuum line can be evacuated while simultaneously pulling the plug from the valve.
  - ➢ Pump down the system until full deflection of the Pirani gauge corresponding to a pressure of around 10^{-4} Torr is achieved.
  - ➢ Pour the liquid nitrogen into the jacket and allow the temperature to stabilise at 77 K for around 25 minutes before carrying out the measurements (the dewar is recommended to be continuously pumped down during measurements to maintain the low pressure).

- Connect the SMA connector from the dewar to the input BNC of the Amptek preamplifier using a SMA to BNC cable.

- Connect the bias supply to the SHV bias input of the preamplifier to bias the detector that is ac coupled to the input of the preamplifier as shown in figure 3.4.

- The energy output of the preamplifier is connected to the input of the shaping amplifier via a BNC cable. The unipolar output of the shaping amplifier is fed to the Ortec MCA that is interfaced to a PC via USB and controlled using the proprietary MAESTRO package. The busy output of the shaping amplifier is connected the BUSY of the MCA for dead time correction.

- The output from the preamplifier and shaping amplifier can be observed using an oscilloscope. By varying the shaping time and gain of the post amplifier the change in the waveforms can be observed.

- Bias the detector to the desired voltage and start the pulse height build-up by using the start acquisition button on the MAESTRO interface. Before the acquisition the properties of the MCA can be adjusted from the MCB properties dialog box as follows.

  ➢ The ADC tab in the properties can be used to adjust the conversion gain of the MCA. The conversion gain represents the maximum number of channels used for storing the pulse height. For instance a gain of 1024 means that the pulse height spectra will be represented by 0 to 1023 channels. The conversion gain should be chosen such that the detected peak in the region of interest (ROI) is represented by at least 5 channels.

  ➢ The lower and upper level discriminator can also be adjusted in terms of channels. The lower level limits the lowest pulse height spectra that can be binned into the MCA (used to reduce the counts in the noise peak). Similarly the higher level determines the highest amplitude pulse that will be stored.

  ➢ The MDA preset tab can also be adjusted to determine the time of collection of each spectrum. The ROI peak preset determine the number of counts required in the region of interest of the peak and the acquisition is stopped when the desired number is achieved. The real time represents the real clock time and can be set to stop the acquisition after a desired period of time. The live time represents the time elapsed since the start of acquisition minus the dead time of the detector.

- After the spectrum has been collected the next step is to calibrate the channels such that the pulse height in terms of energy is obtained. Calibration in MAESTRO can be achieved in terms of units of keV using the following steps.

  ➢ Place the marker on the peak centroid and press insert to insert an ROI on the peak.

  ➢ Select the Calculate/Calibrate option to calculate the centroid of the peak, enter the value of the peak energy on prompt in keV. If there is a warning at the bottom of the status bar, the energy value can be entered manually by placing the marker on the peak centroid.

  ➢ Place the marker on the second peak and repeat the above process, (for the ^{55}Fe source where only a single 5.9 keV peak is resolved by the detector the zero energy noise peak can be used for calibration). Entering 3 or more peak energy values will prompt the program to perform a quadratic fit for more accurate results.

  ➢ The calibrated spectrum can now be saved in ASCII format from the file menu. The calibration data is also saved in the file in the form of three (a, b and c) coefficients that can be recovered by using then in the quadratic equation $ax^2 + bx + c$, where x is the channel number, to obtain the energy value for each x in keV.

  ➢ The data from the ASCII file can now be used in Sigmaplot for Gaussian fitting to determine the peak resolution in terms of energy.

Isotope markers from the library can also be used in the energy calibrated spectrum to locate the position of other gamma rays from the same nuclide (useful for sources that emit photons with a wide energy range such as the ^{241}Am gamma source presented in the thesis).